AN ABSTRACT OF THE THESIS OF

Alberto M. Mestas-Nuñez for the degree of Doctor of Philosophy in Oceanography presented on March 20, 1996.

Title: The Large-Scale Wind-Forced Response of the Pacific.
Redacted for Privacy

Abstract approved:

Dudley B. Chelton James G. Richman

Changes in sea level in the South Pacific from July to September 1978 are estimated from Seasat scatterometer vector wind data based on Sverdrup dynamics assuming a flat-bottom barotropic ocean. These changes in Sverdrup sea level are compared with the changes in sea level observed by the Seasat altimeter for the same time period. The sea level changes observed by the altimeter are consistent with the changes predicted by the Sverdrup model.

A wind stress climatology derived from operational weather analyses by the European Centre for Medium-range Weather Forecasts (ECMWF) has been made available by Trenberth et al. (1990). Global wind stress fields constructed from winds measured by the Seasat-A Satellite Scatterometer (SASS) during 1978 are used here as an independent data set for evaluating the Trenberth et al. (1990) climatology. The ECMWF stresses are shown to be systematically stronger than SASS over extratropical latitudes by almost 50%. This difference can be accounted for by the lack of any scaling factor to convert the ECMWF 1000 mb to surface winds in the Trenberth et al. climatology.

After correcting the systematic error in the ECMWF stresses, the statistical relationship between the large-scale variability of sea level and wind forcing in the South Pacific is investigated from two years of Geosat sea level observations (December 1986 to October 1988). The sea level observations are compared with ECMWF wind stress curl, Sverdrup sea level, and sea level from the Navy layered and Semtner and Chervin z-level models. Although the observed large-scale sea level variability appears to be wind-forced, the dynamics remain unclear.

The flat-bottom, time-dependent Sverdrup theory is used to study the variability of the large-scale circulation in the western North Pacific during the period October 1992–June 1994. Despite the simplicity of the Sverdrup theory, it yields large-scale, seasonal transport variations very similar to the global ocean general circulation model by the Parallel Ocean Program of the Los Alamos National Laboratory. The results are validated using high-quality sea level observations from the TOPEX/POSEIDON altimeter.

The Large-Scale Wind-Forced Response of the Pacific

by

Alberto M. Mestas-Nuñez

A Thesis

submitted to

Oregon State University

in partial fulfillment of
the requirements for the
degree of

Doctor of Philosophy

Completed March 20, 1996
Commencement June 1996

Doctor of Philosophy thesis of Alberto M. Mestas-Nuñez presented on March 20, 1996

APPROVED:
Redacted for Privacy

Co-Major Professor, representing Oceanography
Redacted for Privacy

Co-Major Professor, representing Oceanography
Redacted for Privacy

Dean of College of Oceanic and Atmospheric Sciences
Redacted for Privacy

Dean of Graduate School

I understand that my thesis will become part of the permanent collection of Oregon State University libraries. My signature below authorizes release of my thesis to any reader upon request. Redacted for Privacy

Alberto M. Mestas-Nuñez, Author

ACKNOWLEDGMENTS

I would like to acknowledge the support and encouragement of many people. I am grateful to my thesis co-advisors, Dudley Chelton and Jim Richman, for their guidance, help and interest during the extended period of preparation of this thesis. Roland deSzoeke shared invaluable physical insight through lectures and conversations. Mike Freilich gave helpful suggestions and comments and meticulously proofread the entire manuscript. It has been a pleasure to attend my minor professor, Bob Higdon, lectures in mathematics. Jeff Barnes kindly gave of his time to serve as Graduate Council Representative to the committee.

I am also grateful to the students, faculty and staff of COAS for their help. In particular, Erika Francis gave me a start with the computer system. Ayal Anis helped me with the comprehensive exam. Hemantha Wijesekera, Vasilis Zervakis, and Jorge Mesias provided friendship, motivation, encouragement, laughs and good food. Donna Witter and Ricardo Matano kindly read and commented on early versions of several of the manuscripts. Eric Beals provided outstanding technical support and allowed me to beat him at ping pong many times during lunch time.

Chapter 4 was written while I was working at CAST/MSU in Stennis Space Center. I am thankful to my friends at CAST for their support and encouragement during that time, in particular to Jim Corbin, for giving me the opportunity to work there. Dave Dietrich and Hurley Hurlburt (from NRL) provided many helpful discussions and Don Goff valuable technical assistance.

I would have not been able to accomplish this without the encouragement of my family. Above all I am indebted to my wife, Patricia for her unconditional love and for making my goals hers and helping me to achieve them. To our children

Carolina, Cecilia and Lucas for appearing in scene just when my motivation was weakening and for putting things in perspective. They were the flame that boosted my last years through college, showing me that energy is not always a conservative quantity. I am also thankful to my parents, Andrea and Porfirio; brothers, Mariano, Favio and Saul; and sister, Eliana for their moral support through their visits, letters and telephone calls.

Patricia and I have a big, big thanks for Suresh Venkatswami for becoming our best friend from day one, sharing his Indian culture and putting up with our ironic Argentine sense of humor, and for making himself available to us and our family at all times. Patricia and I have seen many Argentines come and go and we are endebted to all of them for making our country seem closer. Among them Jesus and Estela, Cacho and Nora, Jose and Jillian, Hugo and Miriam, Claudio F., Claudio and Priscila, Ricardo and Paty, Enrique and Estela, and Julio and Laura. We are also thankful to our friends from Pearl River and Kings Circle Asamblies for their prayers.

Genesis 1:2

TABLE OF CONTENTS

TABLE OF CONTENTS (Continued)

TABLE OF CONTENTS (Continued)

LIST OF FIGURES

LIST OF FIGURES (Continued)

LIST OF FIGURES (Continued)

LIST OF FIGURES (Continued)

LIST OF TABLES

To my wife, Patricia

THE LARGE-SCALE WIND-FORCED RESPONSE OF THE PACIFIC

1. INTRODUCTION

Since the pioneering work of Sverdrup (1947) that established the basis for the theory of large-scale, wind-driven ocean circulation, the search for observational evidence to validate Sverdrup's ideas has produced inconclusive results. Early North Atlantic studies concentrated on testing whether the mean meridional transport of volume in the ocean interior derived from climatological winds could be balanced by an opposite transport in the western boundary current. Gill (1971) suggested that the observed transport of the Gulf Stream was up to 5 times larger than the theoretical value derived from the Sverdrup relation. Leetmaa et al. (1977) argued that such a discrepancy arises from neglecting the return flow in a wide western recirculation region. Their estimate of the southward flow across the interior ocean derived from the Sverdrup relation at about 30°N agrees with the southward geostrophic flow from hydrographic data and with the northward Gulf Stream transport through the Florida Straits. However, the assumption that the entire North Atlantic is in Sverdrup balance leads to an inconsistency with previous estimates of the meridional flux of heat (Wunsch and Roemmich 1985). Furthermore, the seasonal cycle of the North Atlantic Sverdrup transport is an order of magnitude larger and has the wrong phase compared to seasonal variations of transport through the Florida Straits (Niiler and Richardson 1973).

In the North Pacific, the Sverdrup balance for the mean flow has been shown to hold by comparison with geostrophic transport calculations from a basin-wide

hydrographic section along 24°N (Hautala et al. 1994). However, seasonal variations of the transport of the Kuroshio inferred from sea level differences across the Tokara Strait are out of phase with the Sverdrup transport (Blaha and Reed 1982).

A problem common to all previous attempts to validate the Sverdrup relation is the lack of suitable, direct observations of winds and currents. Conventional wind climatologies derived from ship observations are spatially and temporally biased and the effects of these sampling errors have not been adequately investigated. Estimates of volume transport by ocean currents are derived from sparse, non-synoptic hydrographic data often taken during different seasons in different years. The controversy about the validity of the Sverdrup relation is even greater at high latitudes in the Southern Hemisphere (Baker 1982; Clarke 1982), where the sparsity of observations is more critical and a well-defined eastern boundary does not exist in most basins.

Large-scale low-frequency variability of surface currents and winds can now be remotely observed from satellite altimetry and scatterometry with spatial and temporal coverages far exceeding those of any in situ observational system. The main goal of this thesis is to exploit these modern remote sensing techniques to test Sverdrup dynamics in the Pacific at mid-latitudes.

In Chapter 2 we use a barotropic, flat-bottom, time-dependent Sverdrup theory to estimate sea level changes in the South Pacific forced by wind stress curl fields derived from winds measured by the Seasat scatterometer from July to September 1978. These theoretical sea level changes are compared with coincident sea level changes observed by the Seasat altimeter for the same 3-month period. This chapter has been published as a note in the Journal of Physical Oceanography (Mestas-Nuñez et al. 1992) and is copyrighted by the American Meteorological Society. The main conclusion is that the South Pacific sea level change computed

from the scatterometer winds assuming a barotropic ocean in Sverdrup balance is consistent with the sea level change measured by the altimeter.

A much longer data record from which to investigate large-scale, wind-forced sea level variability is the 2-year Geosat satellite altimeter data. The longer record length of the Geosat data increases the degrees of freedom by nearly an order of magnitude compared with the 3-month Seasat data record. Unfortunately, there are not simultaneous scatterometer wind observations during the Geosat mission. It has been argued that the best surface wind stress data available for the Geosat period is the one derived from the European Centre for Medium-range Weather Forecasts (ECMWF) analyses (Trenberth et al. 1990). In Chapter 3, the quality of the Trenberth et al. global wind stress fields is evaluated by comparison with Seasat scatterometer wind stress and buoy wind measurements. This chapter has also been published in the Journal of Physical Oceanography (Mestas-Nuñez et al. 1994) and is copyrighted by the American Meteorological Society. We show that the Trenberth et al. wind stress is biased systematically high owing to an error in the reference height of the wind fields assumed by Trenberth et al.. The error is easily corrected and it is therefore possible to use the ECMWF wind stress fields to investigate the wind-forced response from Geosat data.

In Chapter 4, two years of Geosat sea level observations in the South Pacific are compared with ECMWF wind stress curl fields and sea level estimated from the barotropic, flat-bottom, time-dependent Sverdrup theory. The Geosat sea level observations are also compared with sea level fields produced by the Naval Research Laboratory (Hurlburt et al. 1992) and the Semtner and Chervin (1992) wind-forced models. Empirical Orthogonal Functions (EOFs) are used to extract the large-scale sea level variability. The first EOF of Geosat sea level is significantly correlated with the first EOF of the wind stress curl and of sea level from the theory and models.

This suggests that the large-scale variability of Geosat sea level observations in the South Pacific is wind driven. However, the dynamical coupling between wind and sea level variability is unclear for several reasons. First, the uncertainties in the Geosat data are large compared to the small sea level signal associated with the wind-driven response. Second, the analyses of sea level from the models give no indication of the vertical structure of the flow. Third, in the numerical model results it was evident that topographic effects are important over a large region in the eastern South Pacific which raises questions about the validity of the flat-bottom model used here. Fourth, the contribution of heating and cooling to the Geosat sea level observations is unknown.

In Chapter 5 we investigate Sverdrup dynamics in the western North Pacific using high-quality TOPEX/POSEIDON (TP) sea level observations and model output from the Parallel Ocean Program (POP) model of the Los Alamos National Laboratory. The TP data are not contaminated by some of the measurement errors inherent in the Geosat data. We choose the North Pacific because it has better Sverdrup-like qualities than the South Pacific. In particular, it is deeper and has more regular topography than the South Pacific and has well defined eastern and western boundaries at all latitudes. Our main finding is that the large-scale, seasonal transport variations from the simple Sverdrup balance agree well with the results of the POP model. The meridional flow near the subtropical and subpolar North Pacific western boundaries and the zonal flow of the Kuroshio Extension are stronger in winter and weaker in summer/fall. The volume transports of the Sverdrup theory are compared with sea level observations by TP for the same time period assuming that the variability on large space and time scales is barotropic and geostrophic. Only in the Kuroshio do variations of TP and Sverdrup sea level compare well.

2. EVIDENCE OF TIME-DEPENDENT SVERDRUP CIRCULATION IN THE SOUTH PACIFIC FROM THE SEASAT SCATTEROMETER AND ALTIMETER

Alberto M. Mestas-Nuñez, Dudley B. Chelton, and Roland A. deSzoeke

College of Oceanic and Atmospheric Sciences
Oregon State University, Corvallis, OR 97331

2.1. Abstract

Seasat scatterometer and altimeter data are analyzed to investigate time-dependent Sverdrup dynamics in the Southern Ocean (40°S to 60°S) over seasonal time scales. Sverdrup dynamics are shown to be inadequate to describe the circulation in the South Atlantic and Indian oceans. The Sverdrup circulation in the South Pacific is reasonable north of 55°S. The changes in Sverdrup circulation from July to September 1978 indicate an eastward acceleration along 55°S and westward acceleration along 40°S, suggesting a southward shift in the subpolar eastward flow. Sea level in the South Pacific is estimated for July and September 1978 from scatterometer vector wind data based on Sverdrup dynamics assuming a flat-bottom ocean with barotropic flow. The changes in Sverdrup sea level are compared with the changes in sea level observed by the altimeter for the same time period. Both estimates indicate a rise in sea level along a zonal band centered at about 50°S. This sea level rise inferred from both the scatterometer and altimeter data is supported by a similar rise in sea level observed from tide gauge measurements at two locations in New Zealand. The spatial correlation between the two satellite estimates of sea level change is about 0.5. This agreement suggests that time-dependent Sverdrup dynamics may account for about 1/4 of the spatial variance of sea level change in the South Pacific over the 3-month Seasat mission.

2.2. Introduction

The simplest model of wind forced ocean circulation is the classical Sverdrup model for the ocean interior (Sverdrup 1947). In the Sverdrup model, the vorticity input by the wind at the sea surface (given by the wind stress curl) is balanced by the advection of planetary vorticity in the water column. Stommel (1957) suggested the possibility of a Sverdrup balance for the Antarctic Circumpolar Current (ACC) with the Scotia Island Arc 2000 km to the east of Drake Passage (Fig. 2.1) acting as an eastern boundary. Baker (1982) and Godfrey (1989) presented evidence supporting this hypothesis for the region at and north of 55°S. The quality of the wind fields used in these studies has been questioned, however, and Chelton et al. (1990a) were unable to demonstrate a Sverdrup balance at 55°S from 3 months of high quality scatterometer winds. In addition, the modeling study of Clarke (1982) suggests that the Sverdrup balance may not hold south of 55°S.

The validity of the Sverdrup balance for the mean flow in the ACC is thus not completely established. However, recent evidence suggests that Sverdrup dynamics may describe the variability of the ACC over seasonal time scales. Peterson (1988) argued that changes in wind stress curl would produce changes in the meridional transport across the northern and southern boundaries of the ACC and therefore changes in the pressure field within the current, consistent with Sverdrup dynamics. His comparisons of time series of zonally averaged wind stress curl along the boundaries of the ACC with bottom pressure records at a northern and a southern location in the Drake Passage are generally consistent with the required condition of pressure changes being inversely related to the curl in the north and directly related to it in the south.

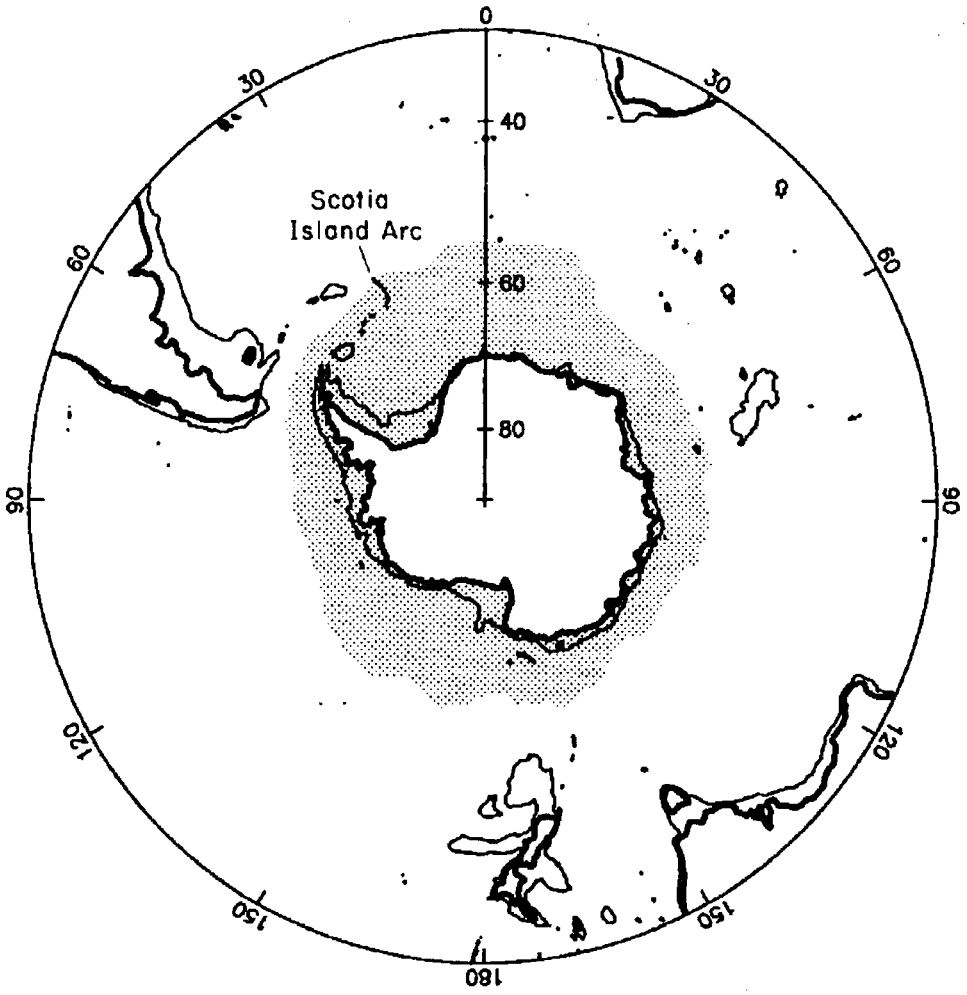

FIGURE 2.1. Map of the Southern Ocean with the 1000 m bathymetry (thin lines) and maximum ice boundary (shaded region) for the Seasat period.

In this paper, time-dependent Sverdrup dynamics in the Southern Ocean are investigated over a 3-month period using a barotropic model of the temporal variability of ocean circulation. The assumption of barotropic variability yields a very simple relation between sea level and wind stress. There is some justification from observations for modeling the variability as barotropic. Whitworth and Peterson (1985) have argued that the mean flow through Drake Passage is 70% baroclinic, but fluctuations about the mean are almost totally barotropic. The barotropic circulation is considered here to be in equilibrium with the monthly mean winds so that the interior ocean is governed by a time-dependent Sverdrup balance.

The wind and sea level data used in this study were measured simultaneously by the scatterometer and altimeter aboard the Seasat satellite, which operated from July 7 to October 10, 1978. The satellite data are described in section 2.3. The global Sverdrup circulation computed from the scatterometer data for the first and last months of the Seasat mission (July and September 1978) are presented and interpreted in section 2.4. In section 2.5, a simple model relating the Sverdrup transport streamfunction to sea level is introduced; the temporal changes in sea level in the South Pacific estimated from the scatterometer data are then compared with the changes observed by the altimeter. The implications of the results are discussed in section 2.6.

2.3. Data Description

2.3.1. Wind Stress

The Seasat-A Satellite Scatterometer (SASS) vector winds used here were produced by Atlas et al. (1987) (see also Chelton et al. 1989). The spatial resolution of these vector winds is about 100 km. The data were binned into 2° × 2° boxes

for the three one-month periods "July", "August", and "September", defined to be July 7 to August 6, August 7 to September 6, and September 7 to October 10, respectively, to allow three complete months of data from the Seasat mission.

The SASS estimates of 19.5 m neutral-stability wind speed and direction were used to generate the vector average of the surface stress following the methodology of Chelton et al. (1990a). Briefly, the wind speed was first corrected for a 1 m/s bias known to exist in the Atlas et al. (1987) SASS data. The 19.5 m neutral-stability wind vectors were brought to a height of 10 m by a neutral-stability multiplicative scaling factor of 0.943. The surface wind stress τ was then computed for each SASS observation of 10 m winds using the bulk aerodynamic formula with the wind speed dependent drag coefficient of Large and Pond (1982). Observations south of a maximum ice boundary determined from passive microwave remote sensing (Fig. 2.1) were eliminated.

The raw 2° × 2° average τ fields showed zonally periodic structure symptomatic of sampling error from spatially inhomogeneous sampling in the monthly averages. The same bell-shaped low-pass filter used by Chelton et al. (1990a) was applied here to generate smoothed 2° × 2° fields analogous to 5° latitude by 16° longitude averages, though with a much better wavenumber transfer function than a simple running average.

2.3.2. Wind Stress Curl

The wind stress curl was computed in spherical polar coordinates to allow for the convergence of meridians at high latitudes (Neumann 1955). The expression for the radial component of the wind stress curl at each grid point is

$$(\nabla \times \tau)_r = \frac{1}{R\cos\theta}\left[-\frac{\partial(\tau_\phi \cos\theta)}{\partial\theta} + \frac{\partial\tau_\theta}{\partial\phi}\right], \qquad (1)$$

where θ and ϕ are latitude and longitude, respectively, and R is the radius of the earth. The subscripts r, θ and ϕ denote the radial, latitudinal and longitudinal vector components. Except at the extreme northern and southern latitudes, the spatial derivatives were computed using quotients of centered finite first differences on the $2^\circ \times 2^\circ$ grid; the meridional derivatives at the extreme latitudes were computed using uncentered differences. Elsewhere, derivatives were not computed if any of the required observations for centered differences were missing (i.e., observations near land or the maximum ice boundary).

2.3.3. Sea Level

The sea level fields used in this study were produced by Fu and Chelton (1985). Each gridded time series of sea level (relative to an unknown reference level) was obtained from crossover sea-level differences between ascending and descending satellite ground tracks near the grid point. The technique can be explained briefly by considering a small area A containing M ascending and N descending tracks. Estimation of the $M+N$ unknown along-track mean sea levels over A from the $M \times N$ crossover difference observations in A is an overdetermined problem. The solutions are determined by least squares, subject to the requirement that the solution for mean sea level along one of the tracks through A be specified to avoid a singular matrix. The time series of sea level is obtained by ordering the solutions by time and setting the value of mean sea level along the first track across the area A to zero.

Fu and Chelton (1985) performed the analysis for 229 areas in the Southern Ocean, each with approximate area $A \approx 200 \times 200$ km^2. The locations of the centers of the areas resemble a 4° latitude by 10° longitude irregular grid (see their Fig. 8).

To increase the signal-to-noise ratio, each time series was smoothed with an effective 20-day running average. The sea level data analyzed here are thus representative of variability over spatial scales larger than 200 km and time scales longer than 20 days. For the analysis presented here, the Fu and Chelton (1985) gridded sea level fields were interpolated onto the regular 2° × 2° grid by cubic spline interpolation and low-pass filtered in space to resolve the same scales as the wind stress described in section 2.3.1.

2.4. Southern Hemisphere Sverdrup Circulation

It can easily be shown (Sverdrup 1947) that the depth-integrated linearized, steady-state equations of motion of an inviscid flat-bottom ocean in spherical coordinates reduce to the Sverdrup balance

$$\frac{\beta}{R\cos\theta}\frac{\partial\psi}{\partial\phi} = \frac{(\nabla\times\tau)_r}{\rho_\circ}, \tag{2}$$

where ψ is the streamfunction of vertically integrated volume transport, $\rho_\circ$ is a representative density of the water column, and $\beta = (2\Omega\cos\theta)/R$ is the meridional gradient of the Coriolis parameter $f = 2\Omega\sin\theta$ for earth rotation rate Ω. The volume transport streamfunction ψ can be obtained by zonal integration of the Sverdrup equation (2) from an eastern boundary starting with a constant initial value $\psi_\circ$, imposed to satisfy the boundary condition of no normal flow. This constant is set to zero at Africa and South America, but not at Antarctica (to allow for Drake Passage throughflow), nor at Australia–New Guinea (considered as a single land mass) or New Zealand to allow circulation around "islands" as first suggested by Godfrey (see Godfrey (1989), deSzoeke (1987), and Chelton et al. (1990a)). Using the nomenclature of deSzoeke (1987) and his Fig. 15 to define the closed integration

paths, the streamfunction values $\psi_\circ$ for New Zealand and Australia can be written as

$$\psi_{NZ} = \frac{1}{f_S - f_N}\frac{1}{\rho_\circ}\oint \tau \cdot d\boldsymbol{l} \tag{3a}$$

$$\psi_{AUS} = \frac{1}{f_{TAS} - f_{NG}}\left[\frac{1}{\rho_\circ}\oint \tau \cdot d\boldsymbol{l} - (f_S - f_{TAS})\psi_{NZ}\right] \tag{3b}$$

respectively, where f_{NG}, f_{TAS} are the values of the Coriolis parameter at the limiting northern (New Guinea) and southern (Tasmania) latitudes of Australia-New Guinea, and f_N, f_S are the same for New Zealand.

The latitude circles that pass through Drake Passage lack a well defined eastern boundary. However, as first noted by Stommel (1957), the Scotia Island Arc imposes a severe restriction on the flow 2000 km downstream of Drake Passage because no latitude can cross it without encountering water depths shallower than 1000 m (Fig. 2.1). Hence, in the present study, the integration of (2) at these latitudes is initiated at the Scotia Island Arc which is considered as an extension of the Antarctic Peninsula. According to Whitworth and Peterson (1985) the mean transport through Drake Passage is 120 Sv (1 Sv = 10^6 m^3s^{-1}). Since $\psi_\circ$ is zero along the boundary of South America, the corresponding mean value of ψ_{ANT} on the Antarctic continent (including the Scotia Island Arc) must be 120 Sv. For the analysis presented here, we allow ψ_{ANT} to increase from 110 Sv for July 1978 to 130 Sv for September 1978, consistent with Whitworth and Peterson's (1985) 20 Sv seasonal increase in the transport through Drake Passage (see their Fig. 7).

The global Sverdrup circulation north of 55°S forced by the 96-day average Seasat winds has previously been presented by Chelton et al. (1990a). Here we attempt to include the latitude band between 55°S and 60°S as discussed above, and examine the changes in Southern Hemisphere subtropical Sverdrup circulation from the beginning to the end of the Seasat mission. The streamfunctions ψ for July

and September computed by integrating (2) and the differences (September minus July), which are proportional to the accelerations of the Sverdrup flow, are shown in Fig. 2.2.

Since equation (2) is strictly valid only for steady-state motions, some discussion of the concept of time-dependent Sverdrup dynamics is necessary. Over the short time scales resolvable by the 3-month Seasat dataset, only the barotropic circulation can come into equilibrium with the wind forcing. The spin-up time of the depth-integrated barotropic circulation is given by the time required for barotropic Rossby waves to cross the basin. The time-dependent barotropic response to wind stress is given by

$$\frac{\partial}{\partial t}\nabla^2\psi_{bt} + \frac{\beta}{R\cos\theta}\frac{\partial\psi_{bt}}{\partial\theta} = \frac{(\nabla\times\tau)_r}{\rho_\circ}. \tag{4}$$

(The effects of advection and diffusion of vorticity, variation of bottom topography, and bottom drag have been neglected.) Neglect of the unsteady term gives a barotropic version of the Sverdrup equation (2). At the basin scales of forcing disturbances evident in Fig. II.2, the relative vorticity is approximately $\nabla^2\psi_{bt} \approx -L^{-2}\psi_{bt}$, where $L \gtrsim$ O(1000 km). This makes (4) resemble a simple one-dimensional wave equation with a westward phase speed of order $\beta L^2 \approx 18$ m s^{-1} at 40°S. For a basin width of 1.2×10^4 km in the South Pacific, the corresponding adjustment time is about 8 days. On longer time scales, say months, the quasi-steady response embodied in (2), ought to be well established.

For latitudes south of Australia and New Zealand, the basin width is more than twice as large (the circumpolar span of the ACC). The circulation adjustment of the full Southern Ocean is therefore more than two weeks and an equilibrium adjustment to monthly mean winds at high southern latitudes is more difficult to rationalize. The computed Sverdrup circulations are nonetheless indicative of the tendency of the ocean to respond to temporal changes in wind forcing. The degree of

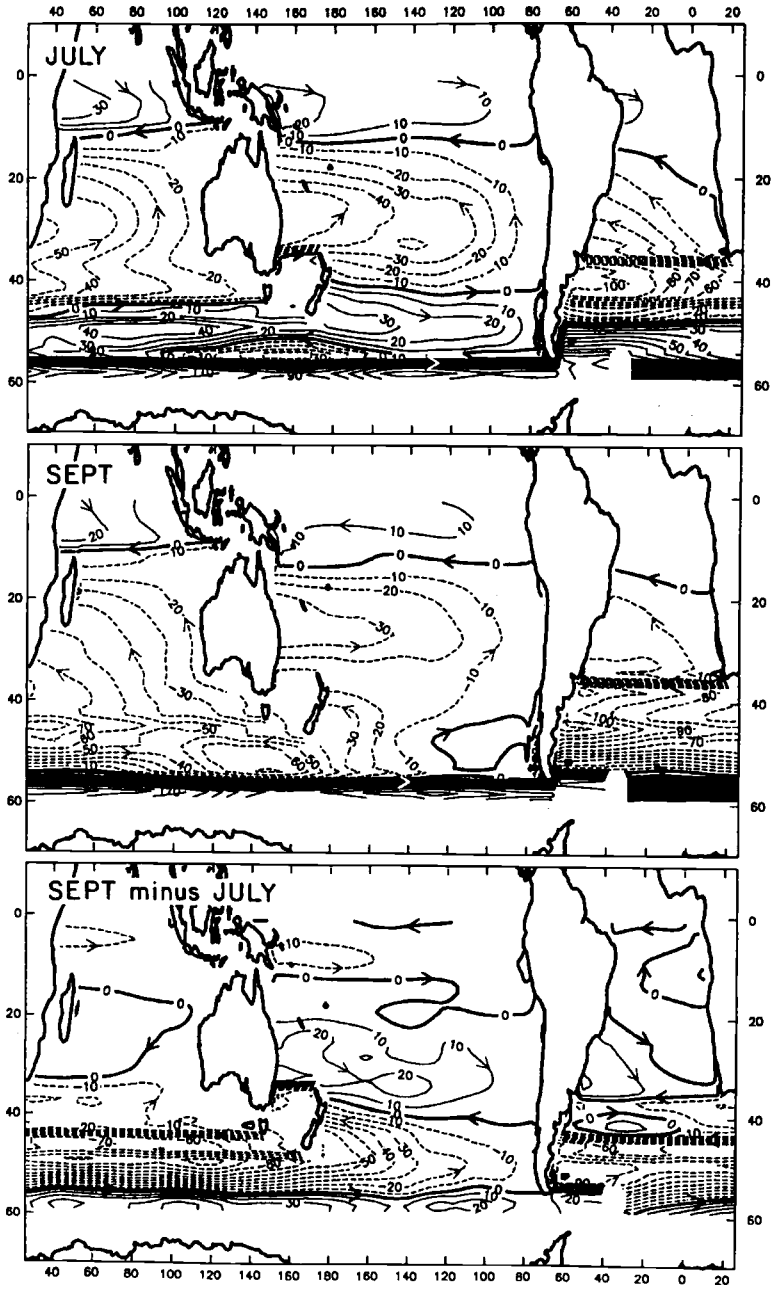

FIGURE 2.2. Sverdrup transport streamfunction in Sv computed from the SASS winds for July 1978 (upper) and September 1978 (middle). The change in Sverdrup circulation (September minus July) is shown in the lower panel.

accuracy of the resulting circulation patterns for each month depends on the relative importances of barotropic vs. baroclinic flow, as well as on the validity of the simple Sverdrup dynamics.

Several shortcomings of the simple Sverdrup model are immediately apparent. The most outstanding is the discontinuity in streamfunction emanating from the southern tip of South America and the northern tip of the Antarctic Peninsula/Scotia Island Arc at 55°S, and associated with the 120 Sv transport across Drake Passage. This discontinuity is purely zonal with no meridional migration as it girdles the pole (although its strength varies somewhat as streamlines leave or join it) and is the model's representation of the ACC core. Similar zonal jet discontinuities extend westward from the southern boundaries of all land masses in the Southern Hemisphere (Africa, Tasmania and New Zealand) and westward from the northern boundaries of New Zealand and Australia. These zonal jets are present in both July and September, but are especially pronounced in July, when they are augmented by a divergent Sverdrup circulation in the South Pacific along 40°S (Fig. 2.3; see also Fig. 5 of Chelton et al. (1990a)).

These jet-like discontinuities could have been ameliorated in the model by including frictional mechanisms to smear the cores across internal zonal boundary layers (Gill 1968), just as friction can be invoked to close the Sverdrup circulation on western boundaries of ocean basins. Indeed the zonal jets in the model exist to lead off the surplus or bring in the deficit water transport in the western boundary currents on the continents and islands where the land masses abruptly end. Along latitudes interrupted by a land mass, the zonal integration of (2) must be stopped at the eastern boundary of the land mass and restarted at the western boundary with a new value of the streamfunction, imposed as zero for South America and Africa, computed by the island rule (3) for Australia and New Zealand, or imposed

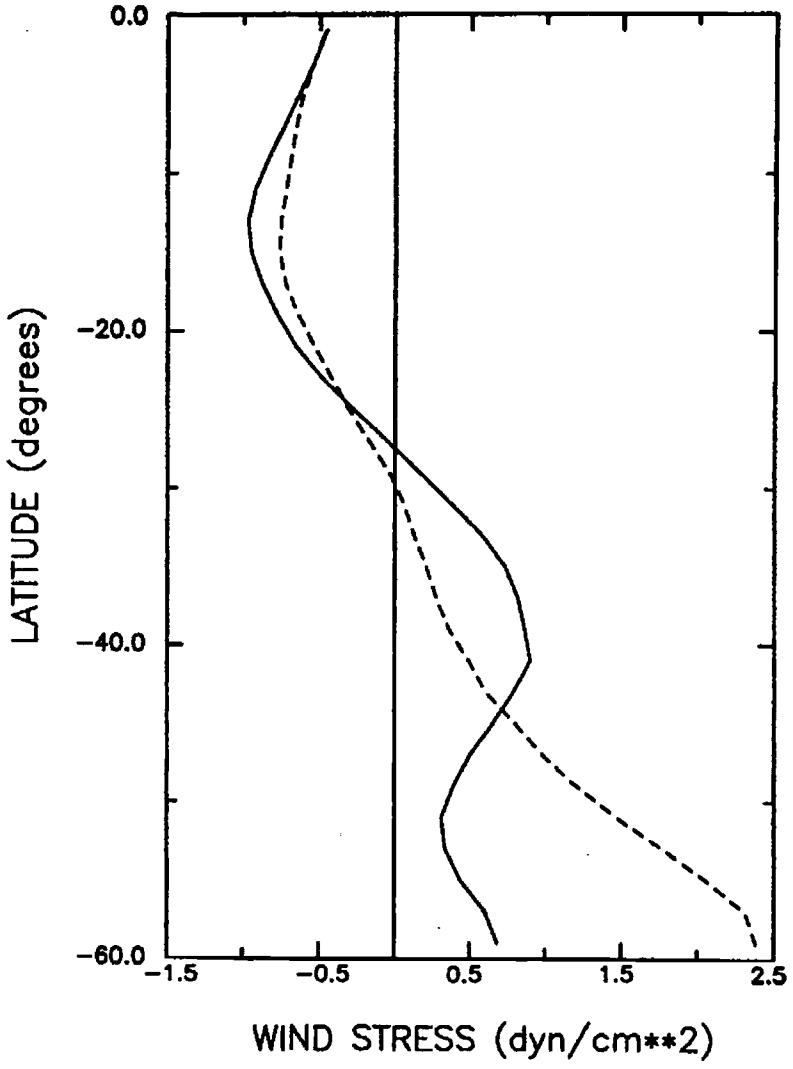

FIGURE 2.3. Latitudinal profiles of zonally averaged eastward component of SASS wind stress in the South Pacific for July (solid line) and September (dashed line).

as the transport through Drake Passage for the Antarctic Peninsula/Scotia Island Arc. The difference between the streamfunction value along the boundary of the land mass and the value just east of the land mass computed from (2) defines the transport of the western boundary current at that location.

At the latitudinal extremities of Australia and New Zealand, the western boundary currents need not vanish. The boundary currents must therefore feed or be supplied by zonal jets extending westward from those extremities. The jets do not waver because they must follow constant latitude lines in the flat-bottom Sverdrup model. It has been remarked that the zonal meandering of the core of the ACC is associated with bottom topography (Gordon et al. 1978; Chelton et al. 1990b). Given the lack of topography in the simple Sverdrup model, it is not surprising that the model jets cannot reproduce this meandering. Such zonal jets do not appear in maps of northern hemisphere Sverdrup circulation because there are no significant unconnected land masses to interrupt the zonal integration of the Sverdrup equation (2). Because of these shortcomings, the Sverdrup circulations are not realistic in the South Atlantic and South Indian and throughout the Southern Ocean south of 55°S where the zonal jets are most pronounced.

Stommel's (1957) suggestion for estimating Sverdrup circulation in the Southern Ocean evidently does not produce quantitatively accurate circulation patterns south of 55°S. In general, then, a suitable model of the circulation must include higher order dynamics such as eddy fluxes and topographic pressure drag (e.g., Johnson and Bryden 1989). The only region where the Sverdrup circulation in Fig. 2.2 appears reasonable is the South Pacific, equatorward of 55°S, a region where the Sverdrup balance has previously been shown to provide a good description of the mean circulation (deSzoeke 1987). In the remainder of this paper, attention is therefore restricted to the subtropical circulation in the South Pacific.

The dramatic changes from July to September in the South Pacific merit special attention. The model net meridional transport between South America and New Zealand is given simply by $-\psi_{NZ}$, which is the sum of the interior Sverdrup transport plus the western boundary current transport along the east coast of New Zealand. Between July and September 1978, this model meridional transport changed from 8 Sv southward to 25 Sv northward. Since ψ_{AUS} remained nearly constant (16 Sv in July and 17 Sv in September), most of this 33 Sv northward increase was compensated by a 32 Sv southward increase in the model meridional transport within the Tasman Sea; the net meridional transport in the Tasman Sea (given by the difference $\psi_{NZ} - \psi_{AUS}$) changed from 24 Sv northward in July to 8 Sv southward in September. The 1 Sv change in meridional transport in the total South Pacific (South America to Australia) from July to September was balanced by a 1 Sv increase in the Indonesian throughflow from the Pacific to the Indian Ocean. The mass balance between the Tasman Sea and the interior South Pacific was achieved by the zonal jets west of the extreme latitudes of New Zealand discussed above. The zonal flow along the northern latitude of New Zealand (approximately coincident with the Tasman Front – see Stanton (1981), Mulhearn (1987)) changed from 33 Sv eastward in July to 12 Sv westward in September. At the same time, the zonal flow west of the southern latitude of New Zealand changed from 25 Sv eastward to 12 Sv westward.

The extreme changes in Sverdrup circulation within the Tasman Sea are remarkable. It should be emphasized that these "circulations" are the equilibrium circulations that would be achieved eventually if the model ocean were allowed to adjust to the winds of the respective months. The largest factor in the changes is the dramatic variation of ψ_{NZ} computed from the island rule (3) between July and September. These changes in the equilibrium Sverdrup circulation are indicative of

very large changes in the wind forcing over the South Pacific during the three-month period of the Seasat mission. The feature in the meteorological fields responsible for the July circulation pattern was an anomalous blocking high southeast of New Zealand accompanied by a strong cutoff low to the northeast (Chelton et al. 1990a); the Sverdrup circulation computed from the July 1978 winds is therefore not representative of the long-term average July circulation. Indeed, the July 1978 circulation of the South Pacific is difficult to reconcile with the traditional view of the surface circulation inferred from hydrographic data (Gordon et al. 1978). In particular, the Sverdrup flow near 55°S was everywhere westward in the South Pacific, counter to the mean ACC.

The westward Sverdrup transport at high southern latitudes is not unique to the scatterometer data set. We have computed similar westward transports from surface wind analyses produced by the European Centre for Medium Range Weather Forecasts (ECMWF) (not shown here). While such westward Sverdrup transport deviates from conventional wisdom, Godfrey (1989) and Chelton et al. (1990a) have pointed out that the depth-integrated flow inferred from hydrographic data is westward south of Australia and New Zealand (Wyrtki 1971; Reid 1986). It must be kept in mind that the temporal variability of the vertically integrated transport at these latitudes is not presently well known. This is especially true during the southern hemisphere winter season of the Seasat mission and during anomalous meteorological conditions such as experienced in the South Pacific during July 1978. It is noteworthy that an apparent westward surface flow extending from the southeast to the central South Pacific between 40°S and 45°S has previously been suggested by Deacon (1977) based on climatological as well as single-season (May-July 1968) water mass characteristics. The possibility of westward vertically integrated trans-

port at high latitudes in the South Pacific during July 1978 therefore cannot be categorically rejected.

In contrast to July 1978, the meteorological conditions were nearly normal during September 1978 (Chelton et al. 1990a). The resulting Sverdrup circulation was eastward at the highest latitudes (near 55°S) with broad equatorward flow over most of the interior basin, turning westward north of about 25°S. This circulation pattern is consistent with the circulation inferred from hydrographic data.

Despite the limitations of the time-dependent Sverdrup model, it can be argued that the circulation computed from models with more sophisticated dynamics would probably also yield a significant response to the large changes in wind forcing between July and September. The change in Sverdrup circulation in the lower panel of Fig. 2.2 can therefore be considered as the tendency for change in the barotropic circulation from July to September 1978. The flow pattern in the interior South Pacific indicates opposing zonal acceleration north and south of approximately 50°S, with eastward acceleration on the south side and westward acceleration on the north side. This can be interpreted as a southward shift of the subpolar eastward flow in the South Pacific. Indeed, while the maximum of the trade winds in the South Pacific maintained its position (15°S) and strength from July to September 1978, the maximum of the westerlies shifted southward from 40°S to 60°S and increased in amplitude by a factor of two (Fig. 2.3).

2.5. Sea Level Changes in the South Pacific

The validity of the changes in Sverdrup circulation in Fig. 2.2 inferred from the scatterometer data can be investigated by comparison with changes in the geostrophic surface circulation inferred from Seasat altimeter data. As noted previ-

ously, only the barotropic component can adjust quickly enough to reach equilibrium over the full South Pacific over the seasonal time scales resolvable by the 3-month Seasat dataset. A barotropic Sverdrup model therefore seems appropriate as a first-order model of the circulation over short time scales.

Since the motion is geostrophic, the relationship of sea level change over three months to the change in barotropic streamfunction is

$$\Delta\eta = \frac{f}{gH}\Delta\psi_{bt} \tag{5}$$

where H is mean water depth, which we take to be 4 km. Hence (2) becomes

$$\frac{\beta gH}{fR\cos\theta}\frac{\partial\Delta\eta}{\partial\phi} = \Delta\left[\frac{(\nabla\times\tau)_r}{\rho_o}\right], \tag{6}$$

where the right hand side is the change in wind stress curl over the three months.

The Sverdrup sea level changes in the South Pacific were computed by zonally integrating (6) for comparison with the altimeter data. Since the sea level change from July to September 1978 in the barotropic model is equal to the change in Sverdrup streamfunction scaled by the factor f/gH, the pattern of sea level change (Fig. 2.4) is very similar to the change in Sverdrup circulation in the South Pacific (Fig. 2.2, lower panel). The two patterns are opposite in sign because $f < 0$.

The field of sea level change from the altimeter is shown in Fig. 2.5. The Sverdrup and altimeter estimates of sea level change both indicate a ridge of sea level rise in the western South Pacific along approximately 50°S, with nodal lines along approximately 40°S and 55°S. A scatter plot comparison of the two gridded fields of sea level change is shown in Fig. 2.6. The two outlier points (circled) come from the region east of the East Pacific Rise, where the altimeter observed sea level decreases larger than 10 cm which the Sverdrup model did not reproduce. This disagreement might be attributable to neglect of topographic effects in the

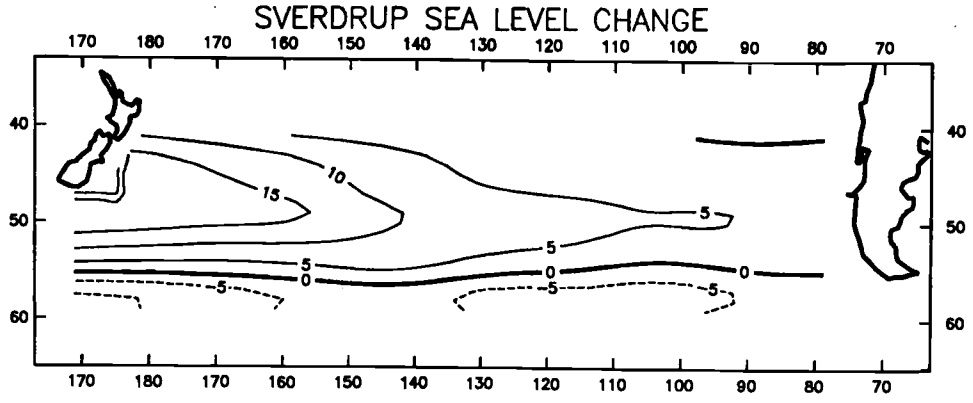

FIGURE 2.4. Map of Sverdrup sea level changes in cm over the South Pacific (September minus July).

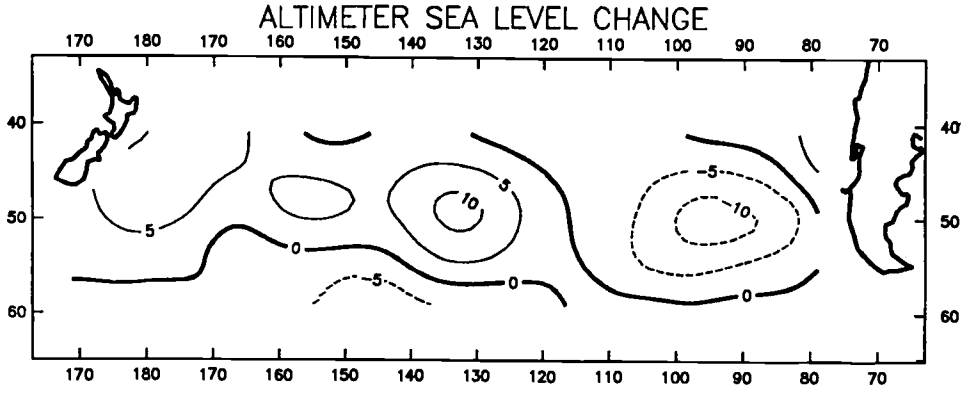

FIGURE 2.5. Map of altimeter sea level changes in cm over the South Pacific (September minus July).

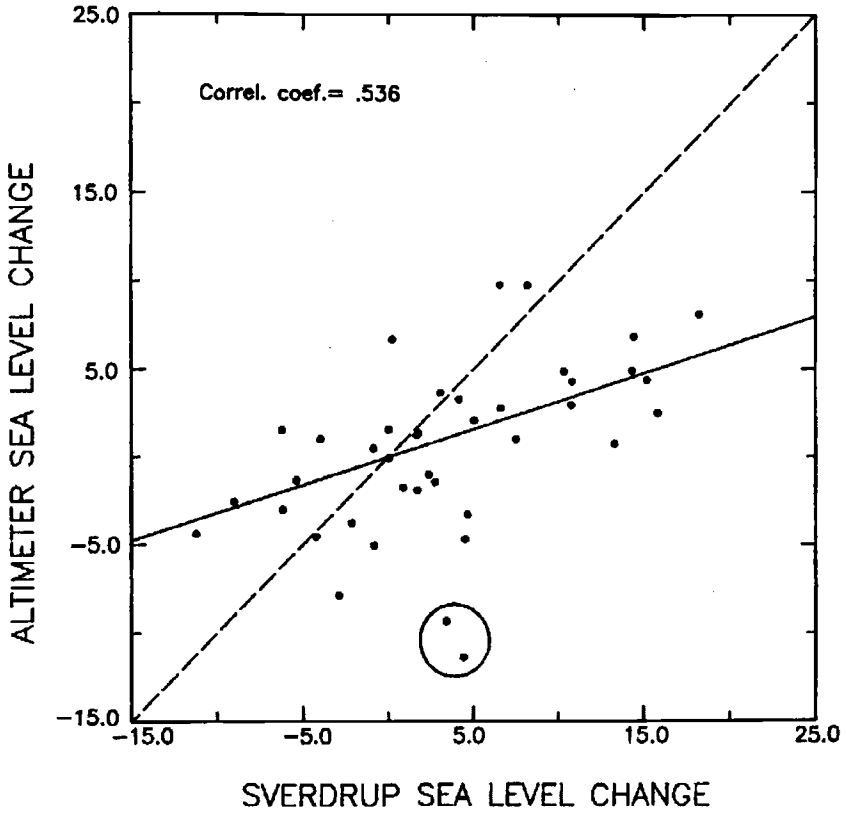

FIGURE 2.6. Scatter plot comparison of Sverdrup and altimeter sea level changes (both in cm) in a 4° by 14° grid for the South Pacific. The regression line through the origin (solid line) has slope 0.3.

model. The spatial correlation between Sverdrup and altimeter estimates of sea level change is 0.54. Using a bootstrap technique (Effron 1979), we estimate the ± 1 standard deviation uncertainty of this correlation to be ± 0.09. Since the 95% confidence interval on the sample correlation is approximately twice the standard deviation, the sample correlation is statistically significant with greater than 95% confidence. The regression coefficient between $\Delta\eta_{\rm alt}$ and $\Delta\eta_{\rm Sv}$ from Fig. 2.6 is 0.3, indicating that the observed sea level change is only about 1/3 of that predicted by the Sverdrup model. The possibility of mechanisms other than Sverdrup dynamics playing a relevant role cannot be ruled out.

The altimeter and Sverdrup sea level changes for the of July-August period (not shown) are qualitatively consistent with the July-September results presented in this section. However, the dynamic range of the July-August sea level change is rather small and further quantitative comparisons become impractical.

2.6. Summary and Discussion

We have calculated the Southern Hemisphere Sverdrup circulation from spatially-smoothed monthly average Seasat scatterometer estimates of wind stress during July and September 1978. These quasi-equilibrium monthly Sverdrup circulations ought to represent the large scale barotropic response to changes in wind forcing.

In contrast to the northern hemisphere, calculation of the Sverdrup circulation in the Southern Hemisphere is complicated by the presence of "islands" (New Zealand and Australia) that interrupt the zonal integration of the wind stress curl and by the fact that there is no meridional land mass barrier at which to begin the zonal integration between 55°S (the southern tip of South America) and 65°S (the

northern tip of the Antarctic Peninsula). These problems were dealt with here by using the "island rule" to determine the streamfunction values along the coasts of New Zealand and Australia and by considering the Scotia Island Arc as an extension of the Antarctic Peninsula and specifying the streamfunction around Antarctica to give the empirically determined Drake Passage mass transport.

A remarkable feature of the July-September change in the Seasat scatterometer winds is the large change in the value of ψ_{NZ} by the island rule, from 8 Sv to -25 Sv. Independent evidence for such a change may be cited from New Zealand tide gauge data. The monthly mean sea levels at Waitemata (174.8°E, 36.8°S) and Wellington (174.8°E, 41.3°S), corrected for a 1 cm/mb inverse barometer effect, rose by 10 cm and 9 cm, respectively, from July to September. This is of the same order as the 8 cm barotropic Sverdrup sea level change computed from (5).

The island rule leads to the shedding of zonal jet discontinuities west of the latitudinal extremities of New Zealand, Australia, Africa and South America. These discontinuities, which might have been moderated by the inclusion in the model of higher order effects such as friction, dominate the charts of Fig. 2.2, except in the South Pacific north of 55°S. For this reason we have focused attention on the Sverdrup circulation in the subantarctic/subtropical sector of the South Pacific. Over the 3-month period of the Seasat mission, only the barotropic circulation can equilibrate with the wind forcing. A barotropic model of the Sverdrup circulation furnishes a simple relation between the wind-generated streamfunction and sea level. The resulting change in Sverdrup sea level in the South Pacific from July to September 1978 compares favorably with the spatially-smoothed sea level change measured by the altimeter. Both patterns of sea level change consist of a zonal band of sea level rise along approximately 50°S with a larger amplitude in the western part of the

basin. Both estimates of sea level also show nodal lines along approximately 40°S and 55°S.

The calculated and observed sea level change over the 3-month Seasat mission can be interpreted as a southward shift of the subtropical front. A very similar change in the circulation has been inferred by Large and van Loon (1989) from analysis of the drift velocities of FGGE buoys during 1979. They argue that the zonal bands of eastward and westward acceleration are a seasonal barotropic response to a semiannual latitudinal shift in the westerly winds of the southern hemisphere. The zonal bands of acceleration in the South Pacific inferred here from three months of Southern Hemisphere winter Seasat scatterometer and altimeter data have also been observed during two consecutive Southern Hemisphere winters from Geosat altimeter data (Chelton et al. 1990b). The Geosat data confirm that this is part of a semiannual signal as suggested by Large and van Loon (1989).

The effects of bottom topography have been neglected in the simple model considered here. For seasonal changes at mid-latitudes, the relation that is believed to hold is the topographic Sverdrup balance (Gill and Niiler 1973; Willebrand et al. 1980). However, Koblinsky et al. (1989) found that the topographic Sverdrup equation could explain the variability of deep ocean currents only at localized regions in the North Pacific. The validity of the topographic Sverdrup balance at those locations has also been questioned by recent numerical experiments (Cummings 1991). Greatbatch and Goulding (1989) showed that away from the western boundary currents the barotropic seasonal changes of the North Pacific circulation are well represented by a flat bottom model. They considered this result to be related to the simple zonal structure of the f/H contours in that basin. In the South Pacific this argument cannot be made since the f/H contours are more complicated.

In the southeastern Pacific, for example, f/H contours are closed (see Plate 1 of Koblinsky 1990).

We have investigated the extreme case of the topographic Sverdrup model in the South Pacific. The resulting acceleration bands follow f/H contours. In the southwestern South Pacific, the f/H contours are nearly zonal but the zonal acceleration bands were opposite in direction to the zonal bands inferred from the flat bottom Sverdrup model, which contradicts the altimetric observations. In addition, in the southeastern South Pacific where the f/H contours are closed, the topographic Sverdrup model becomes inappropriate. We have therefore presented only the results for the flat bottom case.

Anderson and Killworth (1977) (see also Anderson et al. 1979) studied the spin-up of a two-layer ocean with topography and showed that the topography induces interaction between the dynamic modes. As a result of this interaction, the barotropic adjustment occurs on two time scales. First, there is a rapid adjustment (days) to a topographic Sverdrup balance. On a slower time scale (years) the baroclinic mode smooths out the effects of bottom topography and forces the barotropic mode more towards a flat bottom Sverdrup balance. For an intermediate stage of incomplete baroclinic adjustment, such as for a time scale of several months, the barotropic response dominates and the effects of the baroclinic adjustment are difficult to quantify.

In the present study we have neglected baroclinic effects based on arguments presented by Whitworth and Peterson (1985) from analysis of pressure gauge observations at Drake Passage. However, it has been argued that pressure gauges could effectively filter out baroclinic motions (Willebrand et al. 1980). Indeed, a vertical modal decomposition of current meter observations (using empirical orthogonal functions) shows that the low-frequency variability at Drake Passage is surface in-

tensified and can be interpreted as a superposition of barotropic and first baroclinic modes (Inoue 1985), suggesting that coupling between the dynamic modes cannot be neglected. The success of the flat bottom barotropic Sverdrup model in explaining the altimeter sea level patterns could be coincidental. An alternative explanation is that, even on seasonal time scales, the coupling between the first two dynamic modes (as suggested by Inoue) is important and could smooth out the topographic effects on the barotropic mode.

In conclusion, although the statistical significance of the results presented here is rather limited by the short 3-month duration of the Seasat mission, the analysis is suggestive of a Sverdrup-like response of the large-scale circulation of the South Pacific to changes in wind forcing. The discrepancy between modeled and observed sea level response indicates that time-dependent Sverdrup dynamics may not be the only important mechanism. The nature of this response appears to be a seasonal signal associated with large seasonal changes in the wind forcing. At present there are other wind products such as the ECMWF surface wind analyses (e.g. Trenberth et al. 1990) that may be appropriate for investigating this question, although the quality of these analyses at high latitudes in the Southern Hemisphere is still uncertain. Based on the analysis presented in this paper, the South Pacific is a promising region to investigate large-scale response to time-variable wind forcing from a more sophisticated model than the simple Sverdrup model considered here.

Acknowledgements. We thank Robert Atlas for providing the SASS vector wind data and Gary Mitchum for providing the New Zealand tide gauge data used in this investigation. We also thank Ayal Anis, Michael Freilich, Ricardo Matano, Jim Richman and Donna Witter for many helpful discussions and comments on an early draft of this manuscript. The research described in this paper was supported

by Contract 957580 from the Jet Propulsion Laboratory funded under the NSCAT Announcement of Opportunity, and by NASA Grant NAGW-730.

3. AN EVALUATION OF ECMWF-BASED CLIMATOLOGICAL WIND STRESS FIELDS

Alberto M. Mestas-Nuñez, Dudley B. Chelton, Michael H. Freilich, and James G. Richman

College of Oceanic and Atmospheric Sciences
Oregon State University, Corvallis, OR 97331

3.1. Abstract

A new mean monthly wind stress climatology derived from seven years (1980–1986) of operational weather analyses by the European Centre for Medium-range Weather Forecasts (ECMWF) has been made available by Trenberth et al. (1990). This climatology (referred to here as the TLO climatology) potentially represents a significant improvement over climatologies derived only from conventional wind observations. An attempt is made here to quantify the absolute accuracy of the TLO climatology by comparison with global wind stress fields constructed from vector winds measured by the Seasat-A Satellite Scatterometer (SASS) during 1978. From a simulated SASS data set, it is shown that the magnitudes of the SASS stresses must be increased by about 7% to account for a systematic error that can be attributed to the scatterometer spatial and temporal sampling characteristics. After applying this correction, differences between the TLO climatology and SASS winds in the tropics are most likely related to known limitations of the ECMWF analyses. At latitudes south of 50°S, interannual variability and uncertainties in the operational weather analyses are so large that it is not possible to evaluate the TLO climatology on the basis of comparisons with SASS data. Outside of these equatorial and high-southern latitude bands, the TLO stresses are shown to be systematically stronger than SASS by almost 50%. It is found that this difference can be entirely accounted for if the 1980–1986 ECMWF 1000 mb analyses are not interpreted as 10 m winds, as they were in constructing the TLO climatology. This conclusion is supported by an independent comparison of the synoptic ECMWF wind speed estimates with coincident buoy observations.

3.2. Introduction

A significant limitation to present-day modeling of ocean circulation is uncertainty in the wind stress over large areas of the global ocean. Large-scale ocean models have traditionally been forced with mean monthly climatic wind stress fields such as those derived from ship observations by Hellerman and Rosenstein (1983, hereafter HR). Because the vast majority of ship observations are confined to standard shipping routes, the quality of these wind stress fields in remote areas of the ocean is questionable. A new mean monthly surface wind stress climatology has recently been computed by Trenberth et al. (1990, hereafter TLO; see also Trenberth et al. 1989), based on seven years (1980–1986) of twice-daily 1000 mb wind analyses from the European Centre for Medium-range Weather Forecasts (ECMWF). The ECMWF analyses include significantly more ocean data than are available from ship reports alone, particularly over the Southern Hemisphere. In addition to the ship measurements, the analyses assimilate wind and sea level pressure observations from buoys and islands and atmospheric soundings of temperature, humidity and velocity from radiosondes, upward looking radars and satellite observations. The first guess for the analysis at a particular time is given by past information that has been carried forward in a dynamically consistent way by numerical integration of the model. This first guess is updated at each analysis time to be consistent in a weighted least squares sense with the observations. The analyses have relatively coarse spatial (2.5°) and temporal (12 hr) resolutions in addition to known inaccuracies in the tropics (Lambert 1988; Reynolds et al. 1989; Trenberth et al. 1989; 1990) and unknown accuracies in regions of sparse observations, particularly at high southern latitudes. An independent global estimate of the wind stress is needed to assess the accuracy of the TLO climatology, especially in the data-sparse regions.

In this study, high quality global estimates of near-surface winds over the ocean from satellite scatterometry are compared with the 7-year TLO wind stress climatology. The primary advantage of scatterometer data for evaluating the TLO climatology is that the spatial and temporal coverages are far better than those of any other observational system for surface vector winds. Three months of scatterometer data (7 July to 10 October 1978) are available from the Seasat-A Satellite Scatterometer (SASS). Although of disappointingly short duration, these data have previously proven useful for identifying large, systematic errors in the HR wind stress climatology, particularly at high southern latitudes (Chelton et al. 1990). Other scatterometer data such as those from the Active Microwave Instrument (AMI) onboard the European Space Agency ERS-1 satellite launched in July 1991 and the NASA scatterometer (NSCAT) to be launched in 1996 onboard the Japanese ADEOS satellite promise wind observations over longer periods. These data products will be crucial for checking the quality of present wind climatologies and for developing a new, globally accurate climatology.

It is important to bear in mind that the differences between the SASS wind stress field and the 7-year TLO climatology are not necessarily indicative of errors in either data set. The winds during the 1978 SASS observational period may not have been representative of the long-term mean and the differences from TLO must therefore be interpreted with caution. From the comparison of the SASS wind stress field with the HR climatology, Chelton et al. (1990) identified several regions of moderate interannual variability (up to 0.6 dyn cm^{-2} differences) north of 30°S. The differences between SASS and HR winds at higher southern latitudes were much larger (more than 2 dyn cm^{-2} in some regions). On the basis of Southern Hemisphere sea level pressure fields from the Australian Bureau of Meteorology (ABM), Chelton et al. (1990) argued that these differences at high southern latitudes are larger

than can be accounted for by interannual variability alone; although July 1978 was anomalous, sea level pressure was nearly normal in the 3-month average July–September 1978. Because the large-scale winds are approximately linearly related to the pressure fields, it can be inferred that the near-surface winds were approximately normal at high southern latitudes during this same period. However, surface wind stress is nonlinearly related to the vector wind field. Consequently, small deviations from the climatological average wind can be amplified in the stress fields. In order to use the SASS data to assess the accuracy of the TLO climatology, a secondary objective of this study is therefore to attempt to determine how representative the wind stress field at high southern latitudes was of climatological conditions during the period sampled by SASS.

Another secondary objective of this study is to quantify the effects of sampling errors in spatially and temporally averaged wind stress fields constructed from SASS data. Although the quantity and geographical distribution of scatterometer data far exceed those of any other near-surface wind observations, the effects of the irregular and rather complex satellite sampling pattern on the accuracy of the wind fields is still a concern. This important issue has not been addressed by previous analyses of vector wind and wind stress fields constructed from scatterometer and simulated scatterometer data (e.g., Legler and O'Brien 1985; Chelton et al. 1989; 1990; Kelly and Caruso 1990).

Summaries of the data processing used to construct the TLO and SASS wind stress fields used in this study are given in section 3.3. The effects of sampling errors for the SASS instrument (including the actual gaps in the SASS data set) are investigated in section 3.4. In section 3.5, the TLO wind stress climatology is shown to be systematically higher than the SASS wind stress field at extratropical northern latitudes and middle southern latitudes. It is also shown that this systematic

difference can be entirely eliminated when the ECMWF-based TLO wind stress climatology is recomputed with the ECMWF 1000 mb winds corrected to a height of 10 m by applying a multiplicative scaling factor derived on the basis of comparisons between the twice-daily ECMWF wind analyses and coincident buoy observations. The implication of these results is that the TLO wind stress climatology is sytematically high by almost 50%. A three-way comparison of the TLO climatology at high southern latitudes with wind stress fields constructed from SASS and ABM data in section 3.6 concludes that it is not possible to evaluate the quality of the TLO climatology south of 50°S.

3.3. Wind Stress Fields

3.3.1. ECMWF-Based Wind Stress

The TLO mean monthly wind stress climatology was derived from 7-year vector averages (1980–1986) of twice-daily wind stresses computed from ECMWF 1000 mb winds on a 2.5° × 2.5° grid. TLO argued that since ship wind observations were directly assimilated at the 1000 mb level prior to a model change in September 1986, the ECMWF 1000 mb winds for this period were more representative of the winds at a height of 10 m above the sea surface than at 1000 mb. The 1000 mb winds were therefore treated as 10 m winds in deriving the TLO climatology. In defense of this interpretation, Trenberth et al. (1989) cited Böttger (1982) who showed that the ECMWF 1000 mb winds compared favorably with surface observations at ocean weather ship Lima (57°N, 20°W) for the first half of 1982, a period during which wind speeds were as high as 30 ms^{-1}. Some wave modeling studies appear to offer additional support for the interpretation of the ECMWF 1000 mb analyses as 10 m

winds; for example, Janssen et al. (1989) found that accurate wave predictions could be made when the ECMWF 1000 mb winds were treated as 10 m winds.

In the TLO climatology, the ECMWF assumed 10 m winds u_{10} were converted to surface wind stress using the bulk aerodynamic formula with the two-branch Large and Pond (1982) wind speed dependent neutral stability drag coefficient C_N extended to include two additional branches for wind speeds lower than 3 ms^{-1},

$$10^3 C_N = \begin{cases} 0.49 + 0.065 u_{10} & \text{for } u_{10} > 10 \text{ ms}^{-1} \\ 1.14 & \text{for } 3 \leq u_{10} \leq 10 \text{ ms}^{-1} \\ 0.62 + 1.56 u_{10}^{-1} & \text{for } 1 \leq u_{10} \leq 3 \text{ ms}^{-1} \\ 2.18 & \text{for } u_{10} \leq 1 \text{ ms}^{-1} \end{cases} . \quad (1)$$

The form of the 1–3 ms^{-1} wind speed branch was based on the notion that the drag coefficient increases as the wind speed approaches zero; the slope and intercept were calculated from the Large and Pond (1982) value of the drag coefficient at 3 ms^{-1} and empirical fits to the Dittmer (1977) and Schacher et al. (1981) drag coefficients at 2 ms^{-1} (see Fig. 2 of Trenberth et al. 1989). For wind speeds below 1 ms^{-1}, TLO fixed the neutral-stability drag coefficient at the extrapolated value pertaining to 1 ms^{-1}. The Large and Pond (1982) stability correction to the drag coefficient was applied to each gridded, synoptic ECMWF wind vector based on climatological mean monthly values of air and sea surface temperatures and relative humidity derived from the Comprehensive Ocean-Atmosphere Data Set (COADS). The air density needed to estimate wind stress by the bulk aerodynamic formula was computed individually for each ECMWF wind vector from the concurrent ECMWF estimates of air temperature, humidity and pressure.

In section 4, the TLO wind stress climatology is recomputed after reducing the ECMWF 1000 mb winds to 10 m winds using a scaling factor derived from comparisons with buoy winds. This corrected ECMWF-based climatology was gen-

erated using the TLO drag coefficient formulation (1). The Large and Pond (1982) stability correction to the drag coefficient requires both air and sea surface temperatures. The separate COADS air and sea surface temperature climatologies used by TLO were not readily available but their COADS climatological air-sea temperature difference field was. We used the Shea et al. (1990) mean monthly sea surface temperature climatology and derived a mean monthly air temperature field by combining the sea surface temperature climatology with the TLO air-sea temperature difference climatology. As in TLO, the air density used in the bulk aerodynamic formula to estimate wind stress was computed individually for each ECMWF wind vector from the concurrent ECMWF estimates of air temperature, humidity and pressure.

3.3.2. SASS Wind Stress

The wind vectors used in this study were generated by Atlas et al. (1987) who removed the SASS directional ambiguities using an atmospheric general circulation model. This method gives good results for temporally and spatially averaged winds (Chelton et al. 1989). The SASS estimates of 19.5 m neutral-stability wind vectors were used to generate a 2-month vector average surface stress on the ECMWF $2.5° \times 2.5°$ grid for the period 1 August to 30 September 1978. The methodology is essentially the same as that described by Chelton et al. (1990). Briefly, the wind speed was first corrected by subtracting a 1 ms^{-1} bias known to exist in the Atlas et al. (1987) SASS data. Because the SASS measurements of radar backscatter are calibrated to estimate neutral-stability winds at a height of 19.5 m, the appropriate scaling factor and drag coefficient to estimate surface wind stress are those corresponding to neutrally stable atmospheric conditions. The 19.5 m neutral-stability

wind vectors were therefore reduced to winds at a height of 10 m by a multiplicative scaling factor of 0.943, computed from the boundary-layer model of Liu et al. (1979) for neutral stability. In the Southern Hemisphere, observations were eliminated south of a maximum ice boundary determined from passive microwave remote sensing (see Fig. 1 of Mestas-Nuñez et al. 1992).

Surface wind stress was computed for each SASS estimate of neutral-stability 10 m winds using the bulk aerodynamic formula with the TLO neutral-stability drag coefficient (1). Reliable global synoptic estimates of the air density needed in the bulk formulation were not available for the 1978 SASS observational period. It was therefore necessary to use a climatological mean monthly air density. This was computed on the 2.5° grid from the 7-year average of the twice-daily ECMWF estimates of air temperature, humidity and pressure for the TLO period.

As will be shown in the next section, contours of the $2.5° \times 2.5°$ average wind stress from SASS exhibit a zonal quasi-periodic structure symptomatic of sampling errors in the 2-month average (see upper panel of Fig. 3.1). The bell-shaped low-pass filter described in detail in the appendix of Chelton et al. (1990) was applied to smooth the 2.5°-averaged wind stress field with spatial resolution analogous to 5° latitude by 16° longitude moving averages, though with a sharper low-pass cut-off in the wavenumber domain. This smoothing also removes much of the short scale structure in the true wind field that is not resolved by the ECMWF synoptic analyses, thus making the averaged SASS fields more compatible with the TLO climatology.

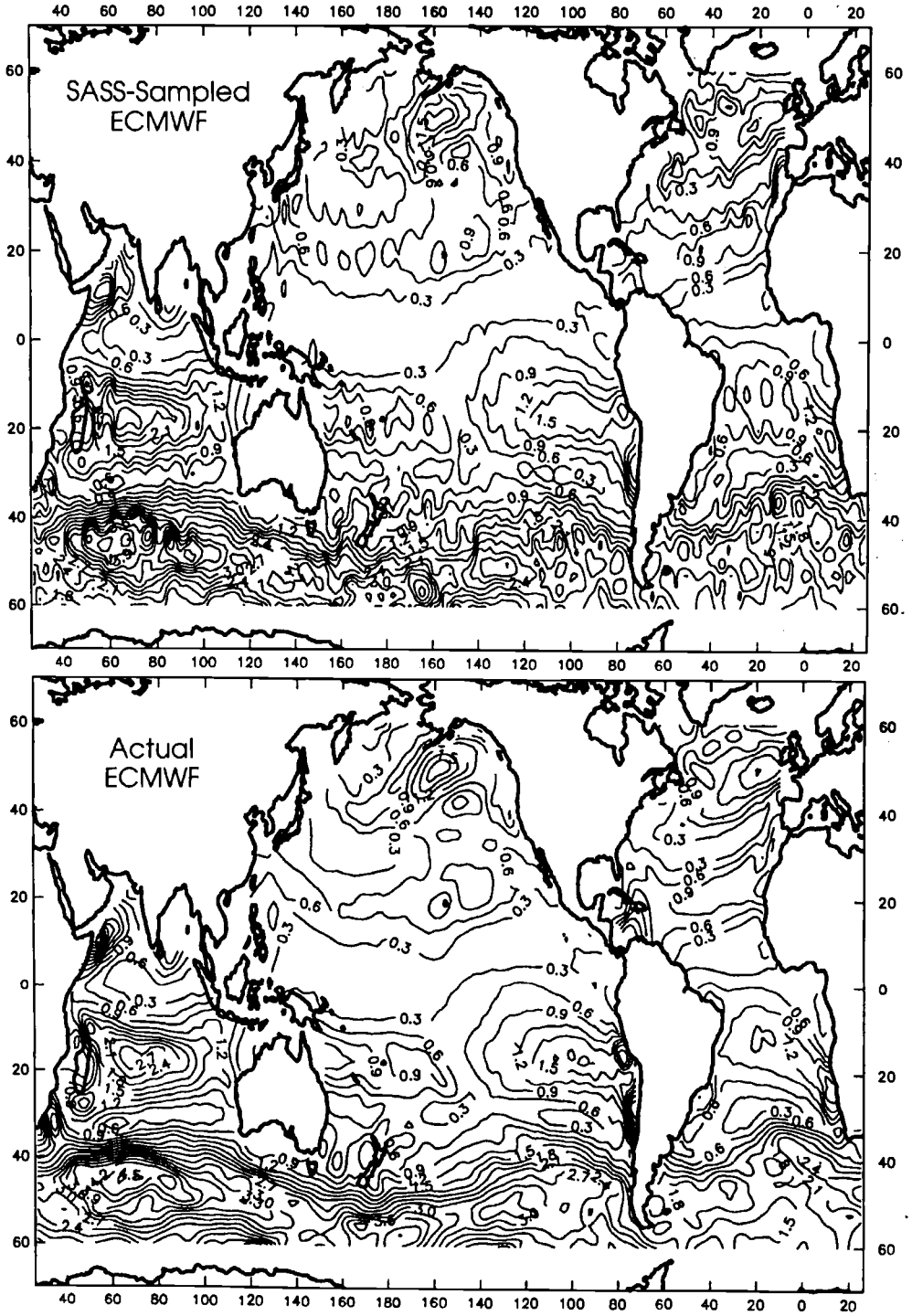

FIGURE 3.1. Magnitude of the August–September 1985 vector average wind stress constructed from the SASS-sampled ECMWF analyses (upper) and the complete ECMWF analyses (lower). Contour interval is 0.3 dyn cm^{-2}.

3.4. Scatterometer Sampling Error

As noted in the introduction, the spatial and temporal coverage of scatterometer data far exceed those of any other available wind observational system. For SASS and NSCAT, the wind field is sampled sequentially in time along the satellite orbit across two swaths of approximately 600 km width separated by a gap of about 400 km centered on the satellite ground track. The AMI samples the wind field over only one such swath and consequently has even greater problems with sampling errors than SASS or NSCAT. These spatial and temporal sampling characteristics are further complicated by spatial overlap of swaths from adjacent orbits at the higher latitudes and by overlap of measurements from ascending and descending orbits. The effects of this complex sampling pattern on the accuracy of spatially and temporally averaged wind stress fields constructed from scatterometer data have not previously been investigated.

An attempt to quantify the effects of SASS sampling errors is made here by simulating SASS measurements of a known wind field and directly comparing averages of the sampled values with the "true" mean quantities. The August–September 1985 twice-daily ECMWF surface analyses were used to define the "true" field, and the ECMWF 1000 mb winds were considered to be 10 m winds for the purposes of this analysis. Sample locations and times (relative to 0000h on 1 August) were taken from the actual SASS data. The SASS-sampled wind vectors were converted to wind stress using the method of TLO and then vector averaged over the 2-month period.

The ECMWF analyses define the "true" winds only at the model grid points in space and time. However, the SASS instrument had higher spatial resolution within the sample swaths and data were acquired continuously in time along the

satellite orbit (rather than at the twice-daily analysis times). The simulation therefore requires interpolation of the ECMWF winds to the SASS measurement locations and times. Schaefer and Doswell (1979) have noted that there is no unique method for interpolating a vector field. Even simple tri-linear interpolation (in two spatial and one temporal dimension) is ambiguous, as systematically different results are obtained if the interpolation is carried out on components rather than on wind speed and direction.

The direction of the interpolated wind vector can be obtained consistently by interpolating zonal and meridional components. However, the magnitude of the interpolated vector can be calculated either by interpolating scalar speeds or by taking the magnitude of the vector defined by the interpolated components. While the two results are identical when the direction of the wind field is spatially constant, the magnitudes obtained by interpolation of scalar speeds are systematically larger than the magnitudes from the component-wise interpolation when the wind direction changes across grid points (see Schaefer and Doswell, 1979; the systematic difference is a simple manifestation of the Schwarz inequality). Care must therefore be taken to assure that the results of the simulations are indicative of the effects of sampling errors, as opposed to interpolation errors. This problem is addressed here by demonstrating that the results are not strongly dependent on the (arbitrary) interpolation scheme used in the artificial simulations. In the following, systematic errors in simulated SASS fields constructed by component-wise interpolation are compared with those in simulated fields constructed by scalar speed and direction interpolation.

Simulated SASS vector wind stress estimates were first obtained by linear space and time interpolation of each ECMWF vector wind component separately to the SASS sample times and locations. The magnitudes of the 2-month vector

average "true" and SASS-sampled wind stress fields for August–September 1985 are contoured in Fig. 3.1. The geographical patterns of high and low wind stress regions in the "true" field are clearly identifiable in the SASS-sampled field. However, the SASS-sampled field also exhibits a zonal wiggliness and patchiness of the contour lines. As the methodology used to compute the individual wind stresses and vector averages is exactly the same for both fields, this effect must be associated with sampling errors related to the SASS orbital characteristics. This is a clear indication that the similar structure noted in section 2.2 and seen previously by Chelton et al. (1990) in the gridded SASS wind stress fields indeed results from scatterometer sampling errors. The upper panel of Fig. 3.2 shows that the Chelton et al. (1990) low-pass filter outlined in section 2.2 eliminates the sampling-related spatial structure of the SASS-sampled field. The same smoothing applied to the "true" 2-month average (lower panel of Fig. 3.2) results in only minor changes in the wind stress field; the contours are somewhat smoother and the extremes of the high and low wind stress regions are reduced slightly in magnitude.

A scatter plot comparison between the smoothed "true" and the smoothed SASS-sampled fields (Fig. 3.3) shows that the scatterometer sampling introduces a systematic error in the wind stress magnitude. A least squares fit line through the origin of Fig. 3.3 (not shown) has a slope of 0.90. The scatter in the comparison of the unsmoothed fields shown in Fig. 3.1 is larger but the slope is the same. On the basis of this comparison, the SASS sampling errors based on component-wise interpolation of the "true" winds thus result in a 10% underestimate of the magnitudes of 2-month vector average wind stresses.

When the SASS-sampled 2-month vector average wind stress field is constructed from vector winds determined by the speed and direction interpolation technique, the regression coefficient increases to 0.97, which is indeed larger than the

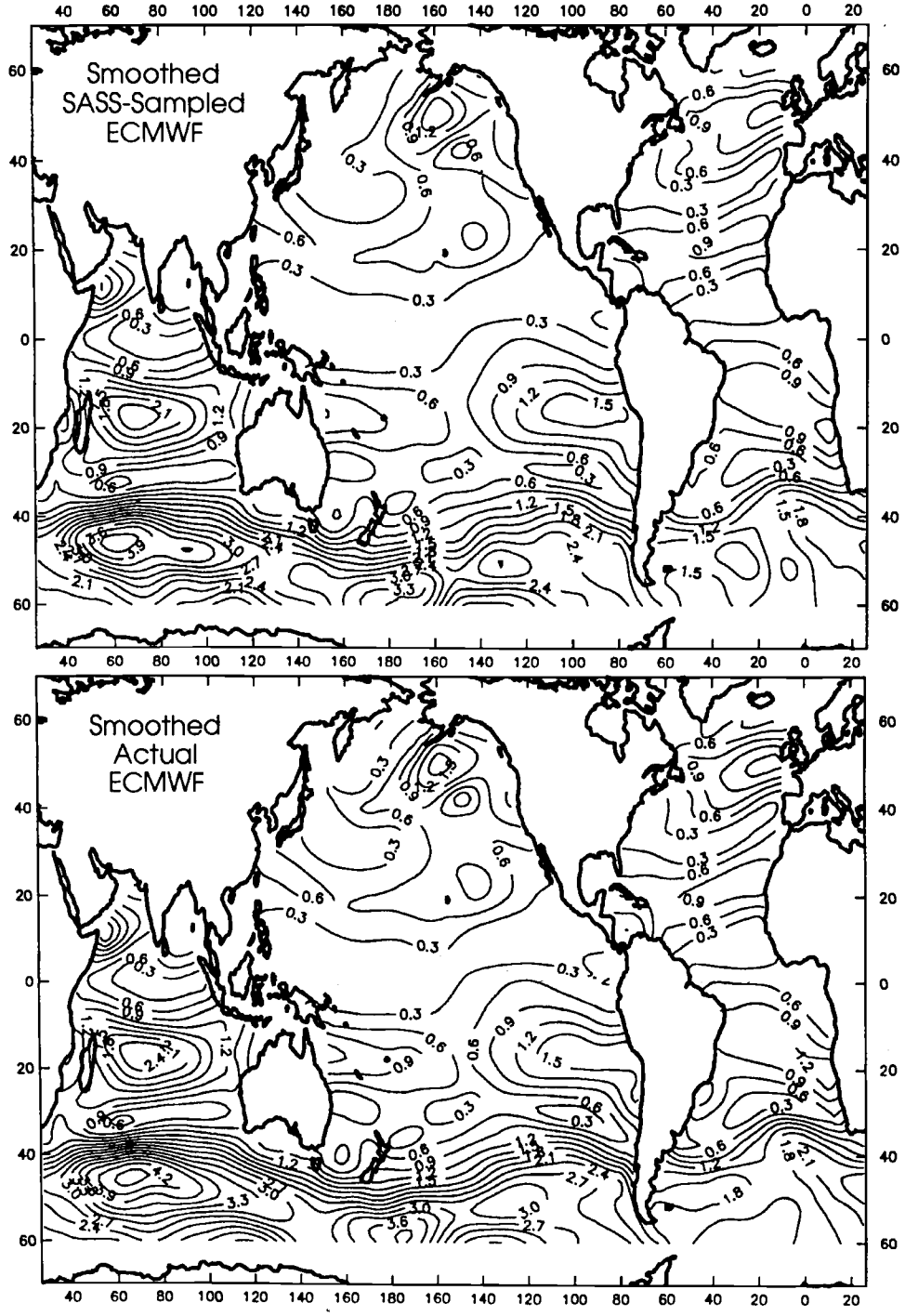

FIGURE 3.2. The same as Fig. 3.1, except both fields have been smoothed as described in the text.

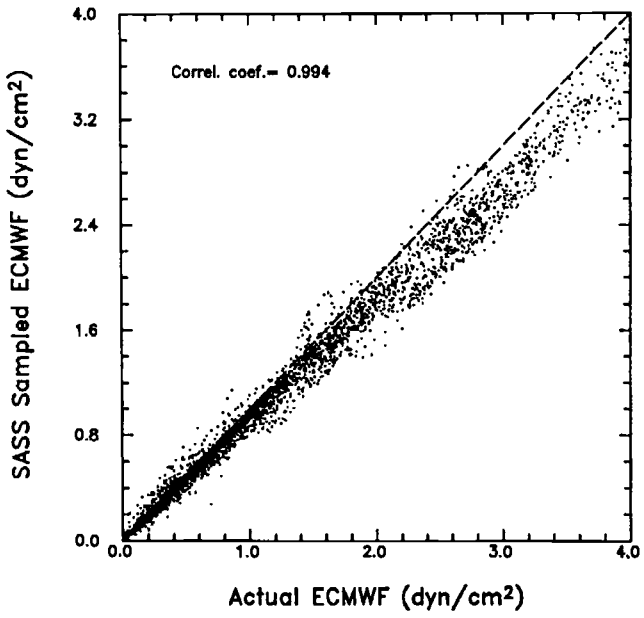

FIGURE 3.3. Scatter plot comparison of SASS-sampled and ECMWF wind stress magnitudes for August–September 1985 in dyn cm^{-2}.

value obtained by the component-wise vector interpolation technique. Although the scaling factors differ somewhat, both vector interpolation methods indicate that the effects of SASS sampling errors are to reduce the magnitudes of the SASS-sampled 2-month vector average wind stress field.

The conclusion that SASS sampling errors bias the 2-month vector average wind stress fields low was further investigated by a third analysis consisting of comparisons between "true" and SASS-sampled 2-month scalar-averaged wind stress magnitudes. After linearly interpolating the wind speeds to the SASS observation times and locations, computing the wind stress magnitude corresponding to each interpolated wind speed and then scalar averaging over the 2-month period, the regression coefficient for the comparison was found to be 0.93. This 7% underestimate of the scalar wind stress magnitude field computed from the simulated SASS data

lies half way between the 0.97 and 0.90 values deduced from vector averaging using the two vector interpolation methods.

All three methods of comparing the "true" and SASS-sampled wind stress fields thus lead to a consistent conclusion that sampling errors result in a systematic underestimate in the 2-month average wind stress fields derived from SASS observations. That the 2-month vector-average wind stress estimates are systematically low in the SASS-sampled data is not surprising. Wentz et al. (1986) have pointed out that wind speeds are approximately Rayleigh distributed. Because of the irregular temporal sampling interval of scatterometer data and the asymmetry of the Rayleigh distribution, the probability of observing high wind speed events within a given 2.5° region is lower than that of observing low wind speed events, thus biasing the magnitudes of averaged wind fields low.

From the above estimates of sampling errors, we recommend increasing the magnitude of wind stress estimates obtained from SASS wind observations by 7% when using the bulk formula with 2-month vector averages. Such a correction is equivalent to increasing the drag coefficient by 7% to compensate for scatterometer sampling errors when computing stress from SASS wind vectors. Hereafter, SASS wind stress fields inflated by 7% are referred to as "corrected SASS".

3.5. TLO and SASS Wind Stress Comparison

Meridional profiles of the zonally averaged eastward components of corrected 2-month vector average SASS and TLO wind stress estimates are shown in Fig. 3.4. The shaded region represents the ±2 standard deviation range of interannual variability over the seven individual August–September ECMWF wind stress fields from which the TLO climatology is constructed. Interannual variability is largest in the

major wind belts, particularly in the Southern Hemisphere westerlies. In general, the profile derived from SASS data falls within the range of natural variability, complicating the ability to distinguish systematic errors in the wind stress estimates from differences associated with interannual variability. In the tropics, however, the difference between SASS and TLO wind stress profiles exceeds the 2 standard deviation range of interannual variability, suggesting an error in one or both of the fields. After removal of the 1 ms^{-1} bias as discussed in section 2.2, there is no documented evidence for any geographical dependence of the accuracies of SASS winds that would account for errors in the SASS wind stress magnitudes in the tropics (Davison and Harrison, 1990). In contrast, Lambert (1988), Reynolds et al. (1989), Trenberth et al. (1989) and TLO have all noted shortcomings of the ECMWF analyses in the tropics, apparently arising from limitations in the ability of the model to analyse the divergent component of the vector wind field in the highly convective tropical regions. The differences between the SASS and TLO wind stress fields in the tropics therefore most likely arise from errors in the ECMWF analyses. The TLO climatological wind stress estimates within the tropical regions (conservatively defined here to be within $\pm 25°$ of the equator) are therefore not considered further in this study.

The August–September TLO and SASS average and difference wind stress fields generated as described in section 2 are shown in Fig. 3.5. For consistency, the TLO wind stress field has been smoothed in the same manner as the SASS wind stress field as described in sections 2.2 and 3. At middle latitudes in the Pacific and Atlantic oceans, the two wind stress fields generally agree to within better than 0.3 dyn cm^{-2}. Previous comparisons of SASS with HR (Chelton et al., 1990) suggested that most of the differences in the Northern Hemisphere could be attributed to apparent anomalous wind stress during the SASS sampling periods.

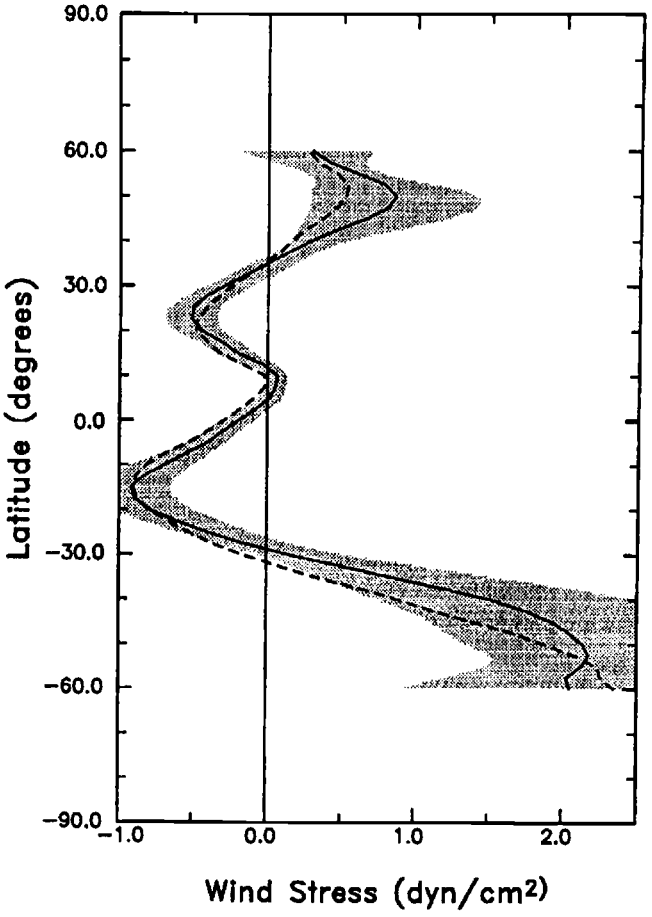

FIGURE 3.4. Latitudinal profiles of zonally averaged eastward components of wind stress from the August–September TLO climatology (solid line) and corrected SASS (dashed line) in dyn cm^{-2}. The ± 2 standard deviation range of natural variability of ECMWF-based wind stress fields during the seven years from which the TLO climatology was constructed is indicated by the shading.

The same conclusion can be drawn here from the SASS and TLO comparison. For example, the band of large differences along 50°N in the North Atlantic is apparently an indication that the westerlies were weaker than normal during the Seasat mission since a similar feature is present in the September differences between SASS and HR. Similarly, the small regions of significant differences off the northwest U.S. coast, the Somali coast and in the western tropical Pacific are also present in the SASS minus HR wind stress fields. Some other Northern Hemisphere differences in Fig. 3.5 may be attributable to anomalous winds during the TLO sampling period. For example, the region of 0.6 dyn cm^{-2} differences south of the Aleutian Peninsula is not present in the differences between SASS and HR (see Fig. 10 of Chelton et al. 1990). This feature is probably related to the deeper-than-normal Aleutian low during the 1980–1986 period noted by TLO.

The main feature of the SASS and TLO difference field in Fig. 3.5 is the band of very large differences at high southern latitudes where the generally eastward TLO wind stress is much stronger than the SASS wind stress. This is also the region of largest interannual variability in the ECMWF analyses (Fig. 3.4). The maximum difference exceeds 1.8 dyn cm^{-2} in the Indian Ocean sector of the Southern Ocean. Evaluation of the TLO climatology is therefore more problematic at these high southern latitudes than elsewhere; discussion of the wind stress field south of 50°S is deferred to section 5.

Stress-dependent systematic differences between the SASS and TLO wind stress fields at extratropical northern latitudes and at middle southern latitudes can be identified even in the presence of the "noise" introduced by interannual variability. The differences between the magnitudes of the two vector-averaged wind stress fields were binned into 0.1 dyn cm^{-2} intervals according to the average of the two wind stress magnitudes. As described previously by Wentz et al. (1986) and Chelton

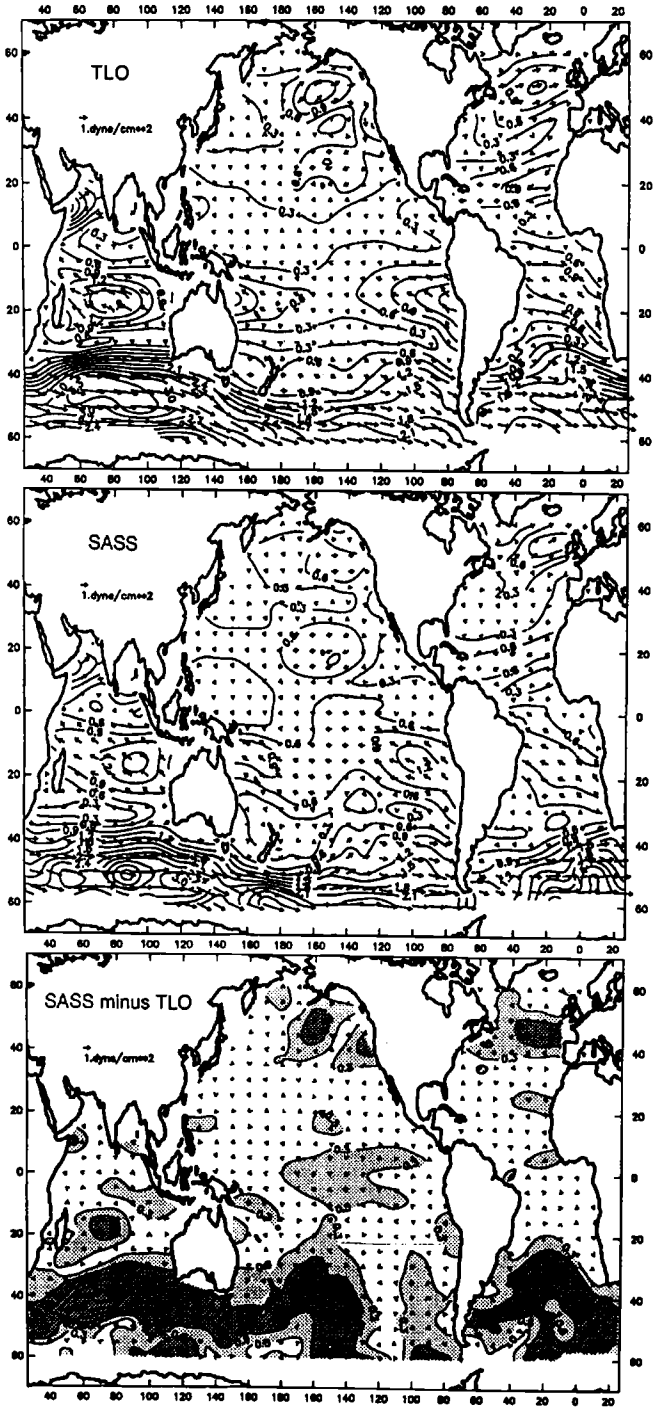

FIGURE 3.5. August–September vector average wind stress from the TLO climatology (upper) and from corrected SASS (middle). Both wind stress fields have been smoothed as described in the text. The wind stress difference (SASS minus TLO) is shown in the lower panel. The contour interval is 0.3 dyn cm^{-2}.

and Wentz (1986), this method of presentation is preferable to the more traditional scatter plot comparison between the the SASS and TLO wind stress magnitudes because it avoids introducing artificial biases at high and low winds; at a location where one of the wind stress estimates is extreme (high or low), it is likely that the other will be less extreme.

The mean and ± 1 standard deviation of the TLO minus SASS wind stress magnitude differences are displayed as a function of the mean stress in Fig. 3.6 for three latitudinal bands. In the extratropical northern and middle southern latitude bands, the differences between the TLO and SASS wind stress fields are very similar and suggestive of a simple scaling difference. From a least squares fit line through the mean differences, the TLO wind stresses are systematically stronger than SASS by 45.7% in the extratropical northern latitudes (25°N to 60°N) and by 46.4% in the middle southern latitudes (25°S to 50°S).

The large and consistent differences between the binned TLO and SASS wind stress magnitudes in Figs. 3.6a and 3.6b are almost certainly indicative of systematic errors in one of the fields. After unsuccessfully exploring several other candidate explanations for these differences, we eventually investigated the possibility that the TLO interpretation of ECMWF 1000 mb winds as 10 m winds might be incorrect. To test this hypothesis, some other reliable estimate of the winds is required. Moored buoy data from the National Data Buoy Center (NDBC) (Meindl and Hamilton 1992) are well suited to such purposes because the data set includes the air and sea surface temperature measurements required for boundary-layer conversions of the buoy winds to a consistent reference height of 10 m. These buoys are located in the Northern Hemisphere primarily along the U.S. coasts. Only the open-ocean buoys north of 25°N were considered for this study to avoid problems in the interpretation of the gridded ECMWF analyses near continental boundaries and

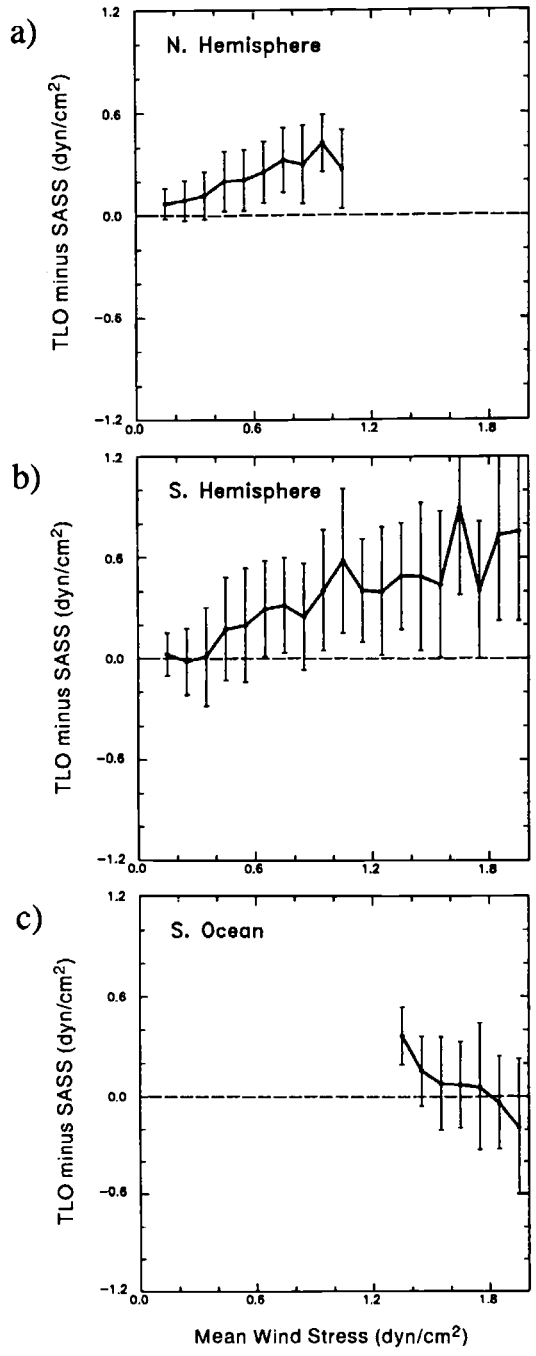

FIGURE 3.6. Comparisons betweeen the magnitudes of the TLO and corrected SASS vector-average wind stress fields a) in the extratropical Northern Hemisphere between 25°N to 60°N; b) in the midlatitude Southern Hemisphere between 25°S and 50°S; and c) and in the Southern Ocean south of 50°(bottom). The mean differences (TLO minus SASS) and ± 1 standard deviations are plotted against the average of the two wind stress estimates in 0.1 dyn cm^{-2} bins.

in the tropical latitudes. The locations of the open-ocean NDBC buoys for August 1980 and September 1985, as well as the nearest ECMWF grid points, are shown in Fig. 3.7. The buoy distributions during these two months are representative of the 7-year period 1980–1986 from which the TLO climatology was constructed.

The NDBC hourly 8-min averages of wind speed were adjusted to a reference height of 10 m, taking into account the stability of the atmosphere (Large and Pond 1982). Although some selected recent NDBC buoys measure relative humidity, this was not the case with the buoys considered during the period of interest in this study. Atmospheric stability was therefore estimated from the buoy measurements of air-sea temperature difference and the climatological mean monthly relative humidity derived from COADS data by TLO (see section 2.1). The buoy estimates of 10 m wind speeds for the August–September periods of 1980–1986 were then compared with concurrent twice-daily ECMWF 1000 mb wind speeds at the nearest ECMWF grid locations.

The results are shown in Fig. 3.8, which has the same format as Fig. 3.6; the differences between the two estimates of wind speed are plotted against their average in 0.4 ms^{-1} bins. A least squares analysis of this comparison of 7378 buoy and ECMWF wind speeds suggest that the ECMWF speeds are 16.5% too high. The corresponding scaling factor of $1/1.165 \approx 0.86$ necessary to reduce the ECMWF 1000 mb wind speeds to the values consistent with coincident 10 m buoy wind speeds falls within the 0.7–0.9 range of published reduction coefficients for converting model isobaric and geostrophic winds to surface winds (e.g., Findlater et al. 1966; Aagaard 1969; Hasse and Wagner 1971; Clarke and Hess 1975; Willebrand 1978; Reynolds et al. 1989; Lalbeharry et al. 1990; Chelton et al. 1990; Freilich and Dunbar 1993). The systematic difference between ECMWF 1000 mb winds and 10 m NDBC buoy winds in Fig. 3.8 thus suggests that the ECMWF 1000 mb analyses during the 1980–

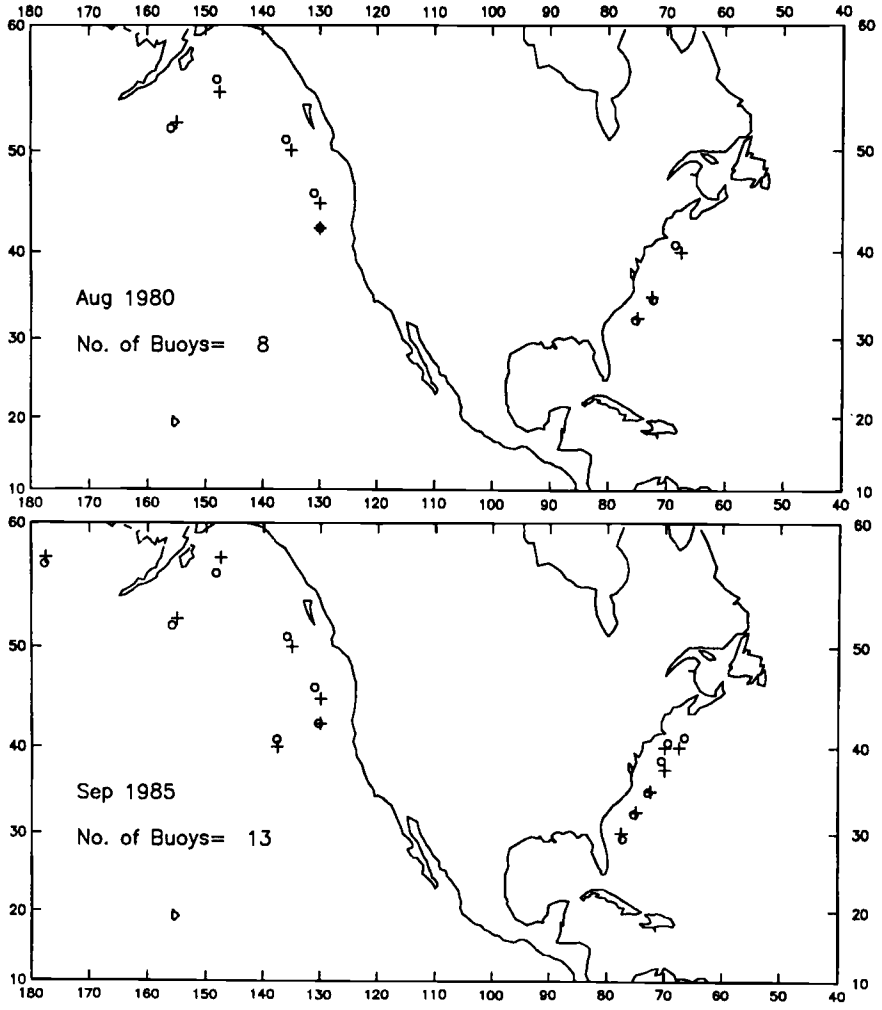

FIGURE 3.7. Map of the National Data Buoy Center (NDBC) buoy locations (open circles) for August 1980 and September 1985. The locations of the nearest ECMWF grid points are indicated as plus symbols.

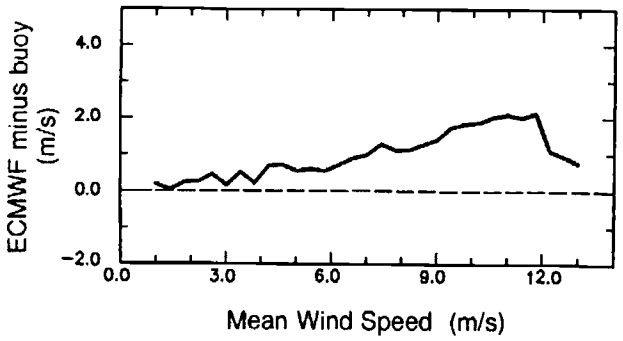

FIGURE 3.8. Comparisons of 7378 concurrent synoptic ECMWF and NDBC buoy wind speeds for the August–September periods of 1980–1986. The mean difference (ECMWF minus buoy) are plotted against the average of the two estimates in 0.4 ms^{-1} bins.

1986 period really are representative of 1000 mb winds rather than of 10 m winds as assumed by TLO.

When the vector-average TLO climatology is recomputed as described at the end of section 2.1 after reducing the ECMWF wind speeds by 14% to convert the 1000 mb winds to 10 m winds, the systematic differences between the 2-month vector average SASS and TLO wind stress estimates are completely eliminated (Fig. 3.9). Thus, as a consequence of the apparent scaling error, the wind-speed dependence of the drag coefficient and the two-month vector averaging, the magnitudes of the wind stresses in the TLO wind stress climatology are too high by almost 50%. We conclude that the ECMWF 1000 mb winds during the 1980–1986 period should not be interpreted as 10 m winds.

This conclusion may have significant implications for the wave modeling results that evidently formed part of the basis for treating the ECMWF 1000 mb analyses as 10 m winds in the TLO climatology. Wave predictions are very sensitive to errors in the wind stress fields used to force the wave model (Janssen et al.,

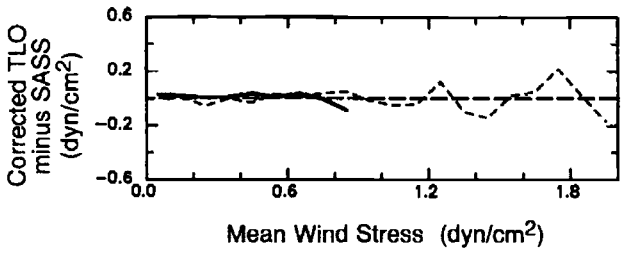

FIGURE 3.9. Comparisons of corrected SASS and corrected TLO wind stress fields for August–September in the extratropical Northern Hemisphere (solid line) and the midlatitude Southern Hemisphere (dashed line).

1991; Beal, 1991; Lionello et al., 1992), with 10% errors in wind speeds resulting in approximately 20% errors in wave height predictions. Operational wave models are forced by twice-daily wind stress fields derived from operational analyses like the ECMWF analyses used to construct the TLO climatology. A proper interpretation of the weather model "surface winds" is clearly important when calculating the stresses used to force the wave models. The exact procedures used by wave modelers when calculating surface stresses from operational weather analyses are often vague. Furthermore, errors in the wave models themselves can be compensated for by errors in the wind stress forcing. For example, in the recent study by Lionello et al. (1992), an operational wave model forced by ECMWF-based wind stress fields was shown to overpredict wave heights within storm regions, but to overestimate the dissipation, and hence underpredict wave heights, outside of the immediate area of the storm system. The model therefore underpredicted wave heights in a global average sense. Increasing the magnitude of the wind stress forcing (by, for example, substituting 1000 mb winds for the 10 m winds used to force the model) could thus apparently offset errors in the wave model, increasing the overall skill of the wave

model. Compensating errors such as these may in fact be responsible for the unreferenced TLO comment that treating the ECMWF 1000 mb winds as 10 m winds yielded more accurate wave model predictions.

3.6. The High Southern Latitude Wind Stress Field

The qualitative impact of the apparent overestimate of wind stress in the TLO mean monthly climatology on ocean modeling can be investigated using the Sverdrup model. In this simple linear model, a 46% overestimate of wind stress results in a 46% overestimate of transport everywhere, but leaves the patterns of circulation unchanged. The effects of such large errors in the wind stress on more sophisticated ocean circulation models may differ in magnitude and are likely to be much more complex spatially but are almost certainly significant.

The Sverdrup circulations derived from the corrected SASS wind stress field and from the corrected TLO wind stress field are shown in Fig. 3.10. Because of the large differences between the two wind stress fields at high southern latitudes (see Fig. 3.5), the differences between the Sverdrup circulations are exceptionally large in this region; streamfunction differences larger than 50 Sv are found in the Indian and Atlantic sectors of the Southern Ocean. The line of zero wind stress curl in the SASS data is displaced considerably more southward (about 5°in the Indian Ocean and more than 10°in the Atlantic) than in the TLO data (Fig. 3.11). This may be indicative of anomalous atmospheric conditions during the 1978 SASS observational period. Alternatively, the possibility of systematic errors in the ECMWF analyses at these latitudes cannot be discounted. The large differences between the two circulations underscore the importance of determining the accuracies of presently

available climatological wind stress fields for ocean circulation modeling at high southern latitudes.

Assessing whether the high southern latitude wind stress field was climatologically normal during the SASS 1978 observational period is very difficult. In the Southern Ocean latitude band, where interannual variability is large as discussed previously, the mean differences between the gridded SASS wind stress values and the TLO climatology are smaller in all but one of the bins than the standard deviation of interannual variability (Fig. 3.6c). It is generally agreed that the ECMWF analyses are presently the most accurate operational weather analyses available globally. However, it is also generally conceded that the best available Southern Hemisphere weather analyses during 1978 were those produced by the Australian Bureau of Meteorology (ABM), although this has not been quantitatively demonstrated to our knowledge. We compared the ABM and ECMWF analyses by computing an independent mean monthly vector average wind stress climatology from the ABM analyses of 1000 mb winds for the 1980–1986 period (the same period used to construct the TLO climatology). From empirical analysis, we found that a very close agreement between the ABM and corrected TLO wind stress fields could be obtained when each gridded ABM 1000 mb vector wind is reduced in magnitude by 21% and rotated 14° counterclockwise prior to computing the vector average wind stress.

The differences between the two 7-year wind stress climatologies are shown in Fig. 3.12a. Over most of the Southern Hemisphere, the differences are very small. The most significant difference is the 0.3 dyn cm^{-2} dipole south of Australia that arises because the jetstream in this region is apparently displaced to higher southern latitudes in the TLO climatology than in the ABM climatology. The 21% scaling factor can be compared with the 14% scaling factor deduced in section 4 for con-

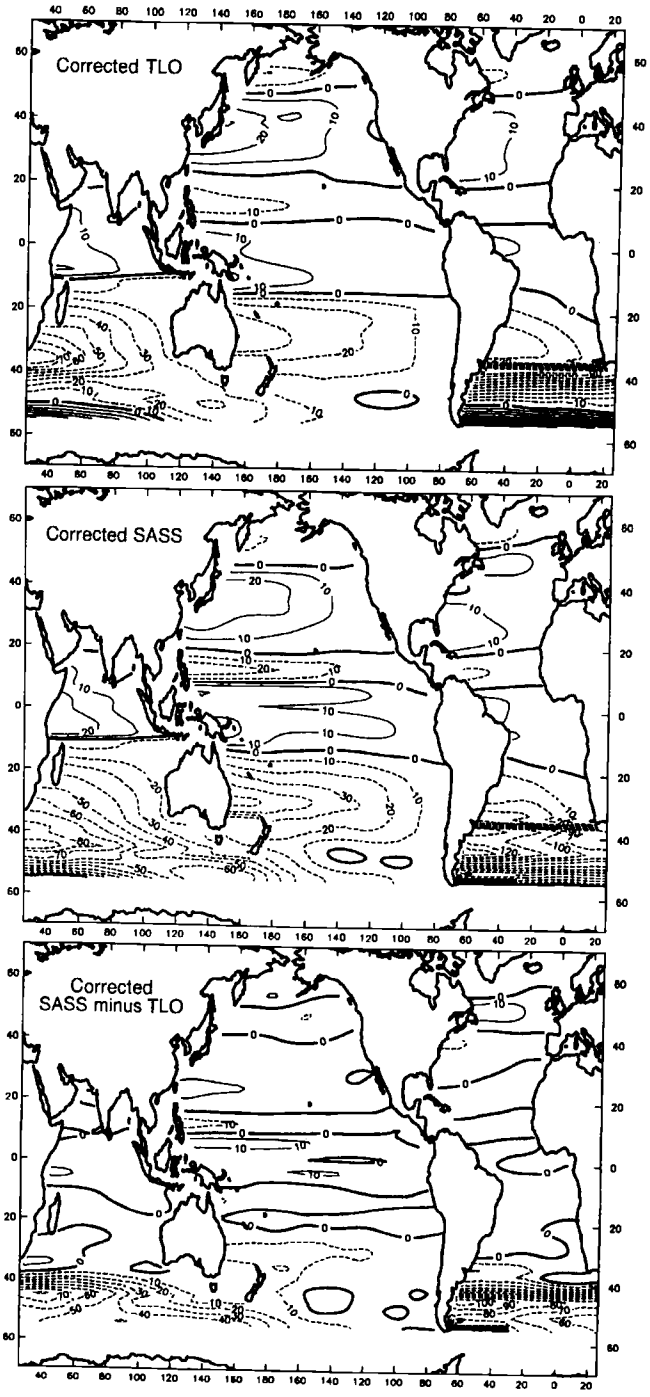

FIGURE 3.10. Sverdrup transport streamfunction field constructed from the corrected August–September TLO wind stress field (top) and the corrected SASS wind stress field (middle). The difference field (SASS minus TLO) is shown in the lower panel. Contour interval is 10 Sv (1 Sv$\equiv 10^6$ m^3 s^{-1}). The computational details of these Sverdrup circulation fields are described by Chelton et al. (1990) and Mestas-Nuñez et al. (1992).

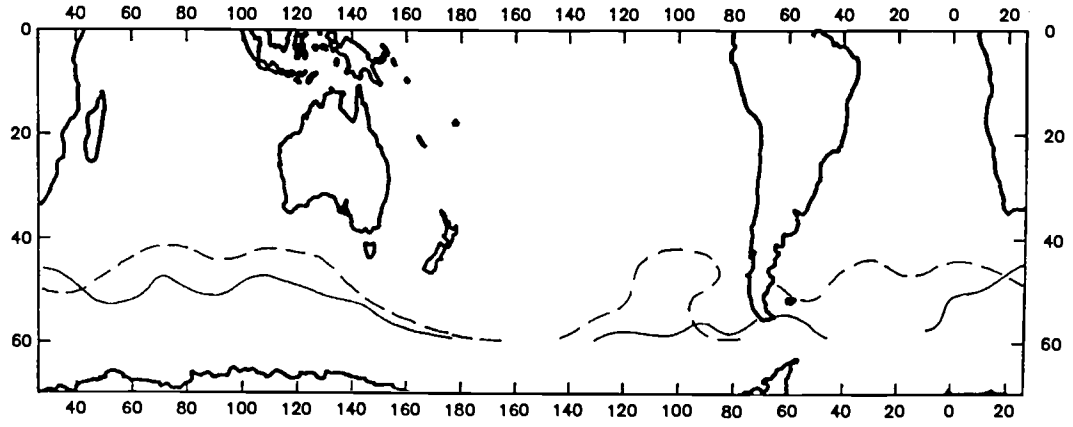

FIGURE 3.11. The line of zero wind stress curl in the southern hemisphere westerlies from the August–September 1978 SASS data (solid line) and the August–September 1980–1986 TLO climatology (dashed line).

verting the ECMWF 1000 mb analyses to 10 m winds. As noted above, both scaling factors are within the range of values used in previous studies to convert model isobaric and geostrophic winds to surface winds. The somewhat larger scaling factor and the 14° rotation angle required to optimize the agreement between the ABM and TLO climatologies apparently indicates that the ABM analyses are representative of somewhat higher altitude winds than the Southern Hemisphere ECMWF analyses. For present purposes, the important point is that the wind stress fields produced from the two operational weather analysis models are remarkably consistent for the 1980–1986 period after appropriate scaling adjustments.

Although there is no assurance that the ABM analyses during 1978 were of comparable quality to the 1980–1986 ABM analyses, an attempt can be made to determine how anomalous the wind stress field was during the Seasat period by comparing the August–September 1978 ABM wind stress field with the 1980–1986 ABM climatology for the August–September period. The difference field (Fig. 3.12b)

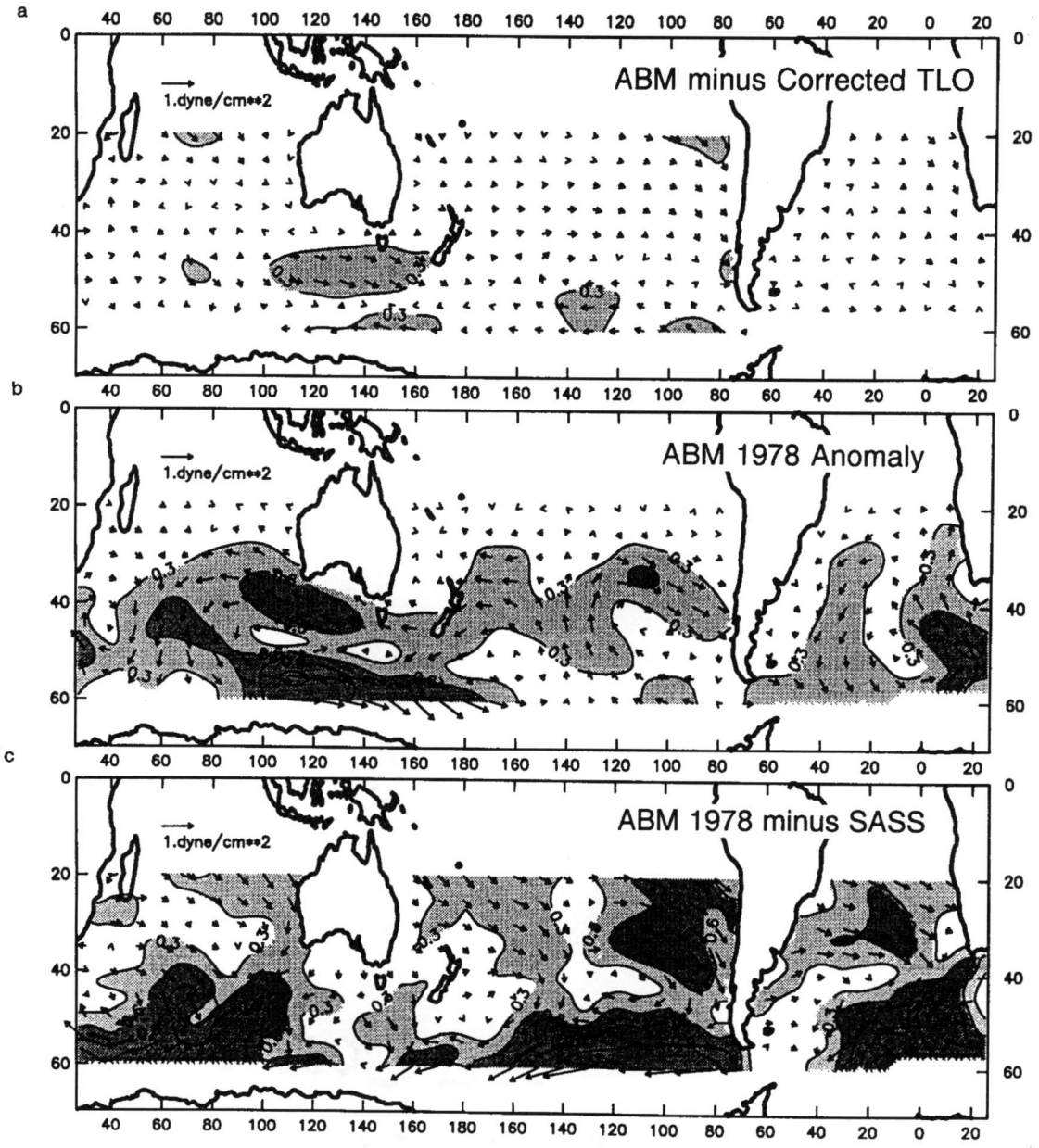

FIGURE 3.12. Differences between a) the ABM and TLO 7-year average August–September wind stress fields (corrected as described in the text); b) the August–September 1978 ABM wind stress and the 7-year ABM climatological average for the same period; and c) the August–September 1978 ABM wind stress and the corrected SASS wind stress for the concurrent period.

suggests that, in 1978, the maximum surface stress associated with the Southern Hemisphere westerlies was displaced southward between about 80°E and 180°E. However, a comparison between the August–September 1978 ABM wind stress field and the concurrent SASS wind stress field (Fig. 3.12c) casts doubt on the quality of stress fields derived from the ABM analyses during this period; there is very little correspondence between Figs. 3.12b and 3.12c. Differences of more than 0.6 dyn cm^{-2} between the ABM and SASS wind stresses are common at latitudes higher than 50°S. As noted previously, there is no reason to suspect that SASS winds were less accurate at high southern latitudes than at other latitudes. However, it is easy to imagine limitations in the accuracies of operational analyses (contemporary as well as during 1978) in this region of sparse observational data.

The analysis in this section unfortunately sheds little definitive light on the accuracy of climatological wind stress fields at high southern latitudes. The consistency between the TLO and ABM wind stress fields for the 7-year period 1980–1986 is encouraging. However, the large discrepancies between SASS and ABM wind stress fields during August–September 1978 are evidently indicative of errors in the ABM analyses during this time period. This implies that the quality of the TLO and ABM wind climatologies at high southern latitudes must be considered suspect; unless there were major improvements in the quality of the ABM analyses between 1978 and the 1980–1986 period, the more recent ABM, as well as the ECMWF, analyses also likely contain large systematic errors. This could account for the large discrepancies in Fig. 3.5 between the SASS and TLO wind stress fields at high southern latitudes. We conclude that a longer record of scatterometer measurements will be necessary to produce a reliable wind stress climatology at high southern latitudes.

One feature of the Sverdrup circulations shown in Fig. 3.10 that merits some discussion is the westward transport south of Australia and New Zealand. This

westward transport is weaker in the Sverdrup circulation calculated from the TLO wind stress than in that calculated from the SASS wind stress, but is nonetheless unambiguously present. The existence of westward Sverdrup transport in this region has previously been discussed by Godfrey (1989) and Chelton et al. (1990), who have also noted that the sparse historical hydrographic data in this region support the possibility of westward transport. Although westward transport in this region is highly inconsistent with the conventional view of the Antarctic Circumpolar Current as a strong eastward flow throughout the Southern Ocean, there is mounting evidence for a strong tendency for westward wind-driven transport from all available wind stress fields (HR, TLO, ABM and SASS), despite limitations in the various wind stress fields.

3.7. Summary and Discussion

In this study, Seasat scatterometer observations and NDBC buoy observations of winds have been used to investigate the accuracy of the Trenberth et al. (1990) ECMWF-based mean monthly wind stress climatology. Although the August–September 1978 scatterometer data are not contemporary with the 1980–1986 TLO climatology, they do offer the advantage of providing a global data set for comparison. The extent to which such a comparison is useful depends upon the degree to which systematic errors can be detected in the presence of interannual variability. The independent point comparisons of ECMWF winds with contemporaneous buoy observations supports an interpretation that interannual variability indeed averages approximately to zero in the Northern Hemisphere and at middle latitudes of the Southern Hemisphere.

An important problem with the SASS data is the sampling error introduced by irregular sampling in space and time. The analysis of section 3 demonstrates that the overall effects of SASS sampling can be diminished by inflating the magnitude of the mean SASS wind stress vectors by about 7%. This result has important implications for the Chelton et al. (1990) comparison of 3-month vector average SASS and HR wind stress fields. Although the systematic underestimate of time-averaged wind stress fields arising from SASS sampling characteristics should have been obvious in that study, as well as in other scatterometer studies (e.g., Legler and O'Brien 1985; Kelly and Caruso 1990), it has been overlooked until now. One reason for this oversight is that the 19% difference between SASS and HR wind stress estimates found by Chelton et al. (1990) was apparently fortuitously consistent with previous independent conclusions by Harrison (1989) and P. Schopf (personal communication, 1989) that HR wind stress estimates were too high by 17–30%. Moreover, the differences between SASS and HR wind stress fields (see the scatter plot in Fig. III.18 of Chelton et al. 1990) matched almost perfectly the 20% difference between the drag coefficients used in the two data sets.

We have repeated the comparison between SASS and HR wind stress fields over the August–September 2-month period after increasing the SASS wind stress amplitudes by 7% to account for SASS sampling errors. It is also necessary to increase the HR wind stress amplitudes by 2% because HR used a constant air density of 1.2×10^{-3} g/cm^3 rather than the 1.223×10^{-3} value of Chelton et al. (1990). After these corrections, the HR wind stress estimates are too high by about 10%, which is smaller than the 20% difference between the two drag coefficients. Consequently, after adjusting for the difference between the HR drag coefficient and the Large and Pond (1982) drag coefficient used with the SASS data, the HR wind stress estimates are about 10% lower than SASS. This result should not be surprising based on the

analysis in section 3 which showed that the drag coefficient must be inflated by about 7% when constructing vector-averged stress fields from the irregularly spaced SASS vector wind observations. The drag coefficient should be inflated similarly for constructing climatological monthly mean wind stress fields from ship observations, which are even more irregularly distributed in space and time than the SASS data. Increasing the drag coefficient by about 10% could apparently compensate for biases introduced by sampling errors in the ship data.

The comparison between TLO and SASS wind stress fields presented in section 4 showed that the TLO wind stress climatology is about 46% higher than SASS in extratropical northern latitudes and middle southern latitudes. From the point comparisons between ECMWF synoptic wind analyses and NDBC buoy winds, this difference is entirely consistent with an error in the TLO interpretation of 1000 mb winds as 10 m winds. Other authors have independently reached similar conclusions. Anderson et al. (1991), for example, found that the 1000 mb ECMWF winds correspond to a height of approximately 30 m, and thus must be reduced in magnitude to be compared with 10 m measurements. The systematic difference between TLO and SASS wind stress magnitudes can be eliminated by reducing the ECMWF 1000 mb wind speeds by 14% to convert the 1000 mb winds to 10 m winds prior to calculating the wind stress from the bulk aerodynamic formula.

A crude method of correcting for the apparent systematic errors in the TLO climatology is to reduce each mean monthly gridded wind stress estimate by 46%. Although the scaling error probably does not deviate much from 46% throughout the year, it should be kept in mind that the analysis described in this study is restricted to the August–September time period. Owing to the wind-speed and stability dependencies of the drag coefficient and the complicating effects of vector averaging in regions of low wind directional steadiness, the scaling factor may vary somewhat

geographically and at other times of year. A complete analysis would require comparisons between ECMWF synoptic 1000 mb wind analyses and concurrent buoy observations for each month of the year. Using the scaling factor determined from such an analysis to convert the 1000 mb winds to 10 m winds, the complete vector-average monthly wind stress climatology should be recomputed as we have done here for the August–September period.

A similar scaling error in the TLO climatology is expected south of 50°S. At these high southern latitudes, however, interannual variability is large, there are no contemporaneous buoy measurements, and a systematic scaling error cannot be isolated based on comparisons with SASS data. We have argued in section 5 that a reliable estimate of mean monthly wind stress does not presently exist at high southern latitudes. Moreover, it will not be possible to construct such a field in this region of sparse conventional wind observations until a sufficiently long record of highly accurate scatterometer winds have been acquired (at least three years, and preferably five or more years). Until such time, the details of model simulations of the Antarctic Circumpolar Current must be considered tentative at best.

Acknowledgements. We thank Robert Atlas for providing the SASS vector wind data used in this investigation and Kevin Trenberth for providing the TLO mean monthly wind stress climatology, the climatological air-sea temperature difference and humidity fields and the sea surface temperature climatology used to calculate wind stress. We also thank Steve Esbensen for helpful discussions during the course of this research. The research described in this paper was supported by Contracts 957580, 957581, and 959351 from the Jet Propulsion Laboratory funded under the NSCAT Announcement of Opportunity and by NASA Grant NAGW-3062.

4. LARGE-SCALE FLUCTUATIONS OF SEA LEVEL AND WIND FORCING IN THE SOUTH PACIFIC

Alberto M. Mestas-Nuñez, Dudley B. Chelton, and James G. Richman

College of Oceanic and Atmospheric Sciences
Oregon State University, Corvallis, OR 97331

4.1. Abstract

The relationship between the large-scale variability of sea level and wind forcing in the South Pacific is investigated using Empirical Orthogonal Function (EOF) analysis. Observed sea level comes from nearly two years of Geosat altimeter data (December 1986 to October 1988). Wind stress curl forcing is calculated from ECMWF 1000 mb analyses. Simulated sea level comes from the flat-bottom, time-dependent barotropic Sverdrup theory and two numerical models driven with winds based on the ECMWF analyses. The numerical models are the Navy layered and the Semtner and Chervin z-level. The EOF analysis reveals the complicated nature of Geosat sea level and wind stress curl variability in the South Pacific. The first EOF of Geosat sea level shows a zonally coherent basin-scale oscillation which is significantly correlated with the first EOF of the wind stress curl and of sea level from theory and models. The analysis supports an interpretation of this mode as a response of the South Pacific to seasonal changes in the wind forcing. The mechanisms appear to be a barotropic response of a stratified ocean over topography.

4.2. Introduction

There are several studies in the literature regarding the large-scale response of the ocean to wind fluctuations on monthly to seasonal time scales. However, the dynamical mechanisms connecting wind and current variability are not well understood. Veronis and Stommel (1956) showed theoretically that in a two-layer unbounded ocean forced with time-dependent winds with periods from a day to a year, the response is in part barotropic and in part baroclinic. Later, Gill and Niiler (1973) used scaling arguments to propose a barotropic topographic Sverdrup balance at annual forcing. Thompson et al. (1986) reviewed more recent theoretical

and numerical studies suggesting the validity of the topographic Sverdrup balance for forcing periods between 2 months and 1 year. Those studies show that for forcing time scales shorter than about 2 months Rossby waves are excited and for forcing time scales longer than 1 year baroclinic effects become important. After baroclinic adjustment a flat-bottom Sverdrup balance should be expected.

Koblinsky (1990) presented scaling arguments supporting the validity of the topographic Sverdrup balance in the frequency band from 10 to 100 days in the North Pacific. Observations showed that the topographic Sverdrup balance could explain the variability of deep ocean currents in that frequency band at localized regions in the North Pacific (Koblinsky et al. 1989). However, the validity of the topographic Sverdrup balance at those locations has been questioned by numerical experiments from a barotropic quasi-geostrophic model (Cummings 1991). In that study, Cummings argued that the presence of barotropic Rossby waves could extend even beyond periods of about 100 days.

In a previous study, we analyzed simultaneous observations of winds and sea level by the Seasat satellite over a 3-month period (July to September, 1978) in the Southern Ocean (Mestas-Nuñez et al. 1992). In the western South Pacific, spatial patterns of sea level change from July to September, measured directly by the altimeter, showed consistency with indirect estimates derived from the surface wind stress measured by the scatterometer using the simple time-dependent flat-bottom barotropic Sverdrup theory. Both estimates of sea level change showed a band of sea level rise along approximately 50°S that were consistent with tide gauge observations at two locations in New Zealand. The spatial correlation between the direct and indirect satellite estimates of sea level change south of 40°S was 0.5 and was shown to be significant, although the theory overestimated the magnitude of the changes by a factor of three and did not describe an observed decrease in sea

level in the eastern portion of the basin (east of 110°W). The baroclinic effects were neglected based on arguments presented by Whitworth and Peterson (1985) from observations at Drake Passage. The barotropic topographic Sverdrup balance was not appropriate because of closed f/H contours.

Although the results of the Seasat study in the South Pacific were encouraging, considering the simplicity of the Sverdrup theory, their statistical significance was limited by the short 3-month duration of the Seasat mission. Analysis of the longer series of Geosat sea level observations over the full Southern Ocean by Chelton et al. (1990) revealed dominant seasonal (annual and semiannual) variability. Since seasonal variability also dominates the wind forcing field in the Southern Hemisphere (van Loon and Rogers 1984), it was expected that a relationship between the two could be found.

The goal of this research is to study the large-scale variability of sea level in the South Pacific and its relation to wind forcing using 23 months (December 1986 to October 1988) of Geosat altimeter observations. Variability of a time series is defined here as deviations of monthly values with respect to a temporal mean calculated over the whole record length. The spatial and temporal characteristics of the large-scale sea level variability observed by the Geosat altimeter are described efficiently using Empirical Orthogonal Function (EOF) analysis (e.g. Preisendorfer 1988). This technique was previously applied to altimeter sea level observations in the Southern Ocean by Fu and Chelton (1985) and Chelton et al. (1990). The physical mechanisms are investigated by comparing the dominant modes of the observed sea level variability with the corresponding modes of variability of wind stress curl forcing and of sea level from theory and two ocean models. The theory is the flat-bottom, time-dependent barotropic Sverdrup balance and the models are the Navy layered, and the Semtner and Chervin z-level. The EOF analysis has

proven a useful technique for comparing model results with observations in other studies (e.g. Garzoli and Philander 1985; Garzoli et al. 1992).

Remotely sensed winds from a satellite scatterometer are not available during the Geosat mission. We therefore use wind stress data based on European Centre for Medium-range Weather Forecasts (ECMWF) 1000 mb wind analyses; the same winds on which the forcing functions of the NRL and SC models were based. The geographical region of interest in this study ranges meridionally from 30°S to 55°S, and zonally from 180°E (just east of New Zealand) to the coast of South America.

The sea level and wind data is described in section 2. A brief review of EOF analysis and the methods used are given in section 3. The results of the EOF analysis of sea level and wind stress curl forcing and the comparison of the EOFs of Geosat with the EOFs of the curl and of sea level from theory and models are presented in section 4. Discussion of the results is provided in section 5.

4.3. Data Description

4.3.1. Geosat Sea Level

The sea level data used here consist of 23 months (December 1986 to October 1988) of satellite altimeter smoothed estimates from the Geosat Exact Repeat Mission. The details of the data processing techniques, applied to the raw data to obtain smoothed sea level fields with 2° longitude and latitude spatial grid spacings and 15 days temporal grid spacing, are described in Matano et al. (1993). The spatial and temporal resolution of the sea level fields are approximately 10° longitude by 5° latitude by 30 days, and thus resolve the large-scale, low-frequency variability of sea level. The 2°×2° gridded time series are not all independent, since the grid spacings are somewhat smaller than the spatial resolution.

For the South Pacific subset used in this study the 15-day gridded time series were subsampled to centered monthly values from December 1986 to October 1988 using cubic spline interpolation. These 23 monthly maps of sea level were assumed to correspond to monthly averages and were further interpolated to a 2.5° longitude by 2.5° latitude (2.5°×2.5°) grid using two-dimensional spline interpolation. This 2.5°×2.5° grid is considered the common grid for the analysis and comparisons presented in this study because it coincides with the original grid of the ECMWF winds. Thus, the wind stress curl and Sverdrup sea level data can be used directly without requiring further spatial interpolations.

4.3.2. ECMWF Wind Stress Curl and Sverdrup Sea Level

The ECMWF wind stress data used in this study consist of monthly averages on a 2.5°×2.5° grid from the 23-month period. The methodology for computing the wind stress from the 1000 mb winds is essentially the same as that of Trenberth et al. (1990). However, the 1000 mb wind speeds were first reduced to a 10 m reference height using a constant scaling factor of 0.86 as suggested by Mestas-Nuñez et al. (1994), in a comparison of the synoptic ECMWF wind speeds and coincident buoy observations for the August-September periods of 1980-1986 in the Northern Hemisphere.

Two wind-related variables are of interest in this study, namely wind stress curl and Sverdrup sea level. The curl was computed from each individual monthly-mean stress field using centered first differences in spherical coordinates. Sverdrup sea level was derived by westward integration of the curl from the South American coast where the sea level is set to zero. The underlying assumptions are that the ocean is 4 km deep, the bottom stress is small, the advection and diffusion of vorticity

are negligible, and the quasi-steady surface response to wind forcing is barotropic (see Mestas-Nuñez et al. 1992).

4.3.3. NRL Sea Level

The Naval Research Laboratory (NRL) layered model evolved from the original two-layer model of Hurlburt and Thompson (1980) with significant upgrades introduced by Wallcraft (1991). This is a nonlinear, primitive equation model with a semi-implicit free surface. An updated description of the model is given by Hurlburt et al. (1996). In this study we use the output from a global 6-layer hydrodynamic version which can handle realistic rough bottom topography confined to the lowest layer. Bottom topography for this simulation comes from ETOP05 (NOAA 1986). Since all thermodynamics effects in this version are neglected, the density remains constant in space and time within each layer (isopycnal). From top to bottom, the σ_T layer densities are 25.24, 26.47, 26.99, 27.23, 27.39 and 27.77. The corresponding initial layer thicknesses are 155, 185, 210, 225, 225 and 5500 meters.

The model was spun up from rest on a 0.7° longitude by 0.5° latitude grid using monthly Hellerman and Rosenstein (1983) wind stress climatology and an eddy viscosity of 1500 $m^2\ s^{-1}$. Statistical equilibrium was reached after 249 years. The latitudinal grid spacing was then switched to 0.25° and the model was run for one year with an eddy viscosity of 300 $m^2\ s^{-1}$. Then the model was run for another 26 years with an eddy viscosity of 100 $m^2\ s^{-1}$. At this point the longitudinal grid spacing was decreased to 0.35° and the simulation continued using ECMWF daily-averaged stresses for the January 1981-June 1993 period. The long-term mean of the ECMWF wind stresses over this period was replaced by the annual mean of Hellerman and Rosenstein. The sea level data was stored every 3.05 days.

In this study, monthly mean sea level fields were generated from the 3.05-day files on the 0.35°longitude by 0.25° latitude grid for the period December 1986 to October 1988. The monthly mean fields were then interpolated to the 2.5°×2.5° comparison grid using two-dimensional spline interpolation.

4.3.4. Semtner and Chervin Sea Level

The Semtner and Chervin (SC) sea level data used here come from files archived at NCAR that were produced by the global Parallel Ocean Climate Model (POCM). The POCM is a free-surface version of the Bryan-Cox-Semtner model following Killworth et al. (1991). In this formulation, coastlines and bathymetry can be prescribed at the local model resolution. The POCM has a longitudinal grid spacing of 0.4° and a latitudinal grid spacing of 0.4×cos(latitude) degrees. Thus, the model latitudinal grid size is 0.33° at about 34° latitude and 0.2° at 60° latitude. The average latitudinal spacing over the full range of latitudes is approximately 0.25°. Over the latitude range of interest in this study (30°S to 55°S) the average latitudinal spacing is approximately 0.29°. The model has a maximum of 20 vertical levels.

In the SC simulation, heat and salt fluxes were modeled by simple restoring to seasonal cycles of Levitus (1982) in the uppermost of the 20 levels, using the method of Haney (1971). Subsurface restoring of temperature and salinity was only used north of 58°N, south of 68°S, and in the vicinity of Gibraltar. Momentum flux was determined from smoothly interpolated monthly values of ECMWF wind stress for 1985-1989, as calculated by Trenberth et al. (1990). However, no corrections for differences between ECMWF 1000 mb and 10 m winds as suggested by Mestas-Nuñez et al. (1994) were applied. A 0.5°×0.5° model initialized with Levitus temperature

and salinity was spun up for 33 years using Hellerman and Rosenstein (1983) winds. Instantaneous fields were then interpolated to the 0.4° longitude by 0.25° (average) latitude grid; and the simulation was resumed, starting with ECMWF winds of January 1985. The sea level data was stored every 3 days.

In this study, monthly mean fields were constructed from the 3-day files on the 0.4°× 0.25° (average) grid for the December 1986 to October 1988 period. The 23 monthly mean sea level fields were then interpolated to the 2.5°×2.5° comparison grid using two-dimensional spline interpolation.

4.4. EOF Analysis and Methods

The temporal mean over the 23-month period was first removed from the 2.5°×2.5° gridded records of Geosat sea level, wind stress curl, and sea level from the theory and models. Because the main focus of this research is on monthly to seasonal rather than long term variability, we also removed a linear trend from the anomaly time series of all the data fields.

The EOF analysis projects a data field onto a set of orthogonal standing modes of variability (e.g. Preisendorfer 1988). Each mode explains a fraction of the total variance of the data and is composed of a nondimensional spatial pattern and a dimensioned amplitude time series. In this study, the EOF calculation was performed efficiently using singular value decomposition of the data matrix as suggested by Kelly (1988). To aid interpretation, the spatial patterns were normalized so that the mean square value over all grid points equals 1.

Before presenting detailed results of the EOF analysis it should be noted that individual empirical modes are not always physically meaningful. In particular, modes higher than one because of the orthogonality constraint. In section 4.2, we

show and describe the first four empirical modes of Geosat sea level. Physical interpretation of these modes is investigated based on comparisons with the first four empirical modes of wind stress curl forcing (section 4.3) and of sea level from theory and two ocean models (sections 4.4 to 4.6).

The comparison of two empirical modes from different fields involves spatial pattern correlations and temporal correlations of their accompanying amplitude time series. The spatial correlations were performed by subsampling the spatial patterns into a 10° longitude by 5° latitude grid, which is the approximate spatial resolution of the Geosat data set. The standard deviation uncertainties of the spatial and temporal sample correlations were estimated using a bootstrap technique (Effron 1979). The 95.5% and 99.7% confidence limits of the correlations were estimated from the two and three standard deviation intervals, respectively.

4.5. Results

4.5.1. Variance Budget

The percentage of total variance explained by the first four EOF modes for the Geosat, wind stress curl, Sverdrup theory and two ocean model fields are shown in Table 4.1, with curves of cumulative variance explained as a function of EOF mode number depicted in Fig. 4.1. The first four modes of Geosat sea level account for 58% of the variance and 13 modes are required to explain 90% of the variance. That a large number of modes is needed to explain most of the variance illustrates the complicated nature of the Geosat sea level variability, as noted by Chelton et al. (1990).

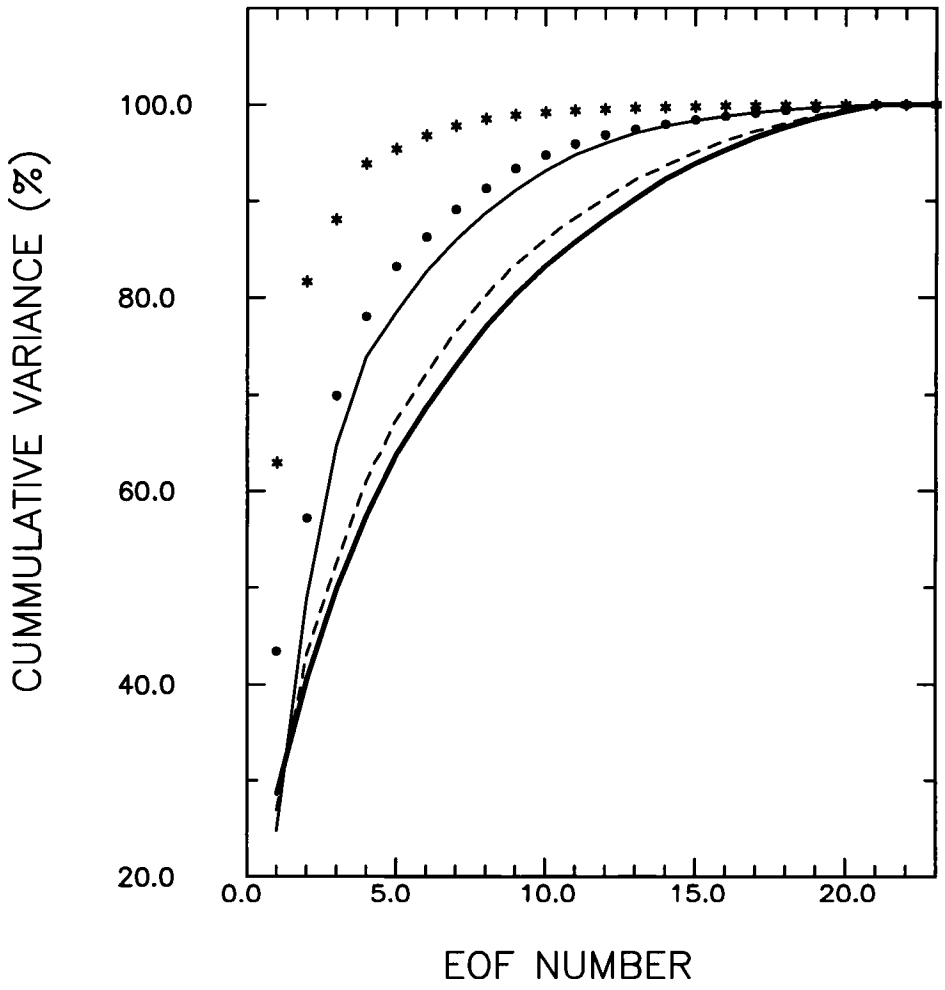

FIGURE 4.1. Cumulative percentage of variance explained as a function of mode number for the empirical orthogonal function (EOF) decomposition of Geosat sea level (heavy solid line), wind stress curl (dashed line), Sverdrup sea level (asterisks), NRL sea level (dots), and SC sea level (light solid line).

TABLE 4.1. Variance budget of the first four empirical orthogonal functions (EOFs) in percent.

EOF	Geosat	Curl	Sv.	NRL	SC
1	29	27	63	43	25
2	12	16	19	14	24
3	9	10	6	13	16
4	8	8	6	8	9
Sum	58	61	94	78	74

The first four modes of wind stress curl account for 61% of the total variance and 12 modes are needed to explain 90% of the variance. The distribution of variance among the first four modes (Table 4.1) and the cumulative distribution of variance for wind stress curl (Fig. 4.1) compare well with Geosat sea level. This suggests that the variability in Geosat sea level and in wind stress curl have similar nature.

The four most significant EOFs of Sverdrup sea level account for 94% of the total variance of Sverdrup sea level, which is 36% more variance than explained by the first four modes of Geosat. This illustrates the simpler nature of the Sverdrup sea level variability compared to the Geosat and curl variability. A simpler character for the Sverdrup variability compared to the curl is expected, considering that Sverdrup sea level at a given location is calculated by zonal integration of the curl between that point and the eastern boundary. Thus, much of the spatial variability present in the curl is smoothed out by the Sverdrup calculation.

The four most significant modes of NRL sea level account for 78% of the total variance. This is 20% more than the variance accounted for by the first four modes of Geosat sea level (58%) and 16% less than the variance explained by the first four modes of Sverdrup sea level (94%). Thus, the NRL sea level variability is more

complicated in nature than the Sverdrup sea level variability. This is a result of the NRL representation of bottom topography, stratification, and transient motions not described by the simple quasi-steady Sverdrup theory.

The first four modes of SC sea level account for 74% of the total variance of SC sea level, which is 16% more than the variance explained by the first four modes of Geosat sea level. Thus, SC is the best of the three simulated sea level fields in describing the observed distribution of sea level variance among the different modes. This was expected considering that the SC model is the most realistic because it takes into account bottom topography, stratification, and transient motions, and has higher vertical resolution than the NRL model. Furthermore, it does not require scaling down the topography to keep it confined to the deepest layer as in the NRL case.

4.5.2. Geosat Sea Level

The four most significant EOFs of Geosat sea level are shown in Fig. 4.2 and their associated amplitude time series in Fig.4.3.

The first empirical mode of Geosat sea level (Figs. 4.2a and 4.3a) accounts for 29% of the total variance (Table 4.1). Its spatial pattern (Fig. 4.2a) shows a basin-scale nearly meridional oscillation with its axis (zero contour line) meandering across the South Pacific between 40°S and 50°S. Superimposed on this large-scale pattern there are smaller scale spatial structures. The main deviation from a pure meridional oscillatory pattern is a greater than 10° northward excursion of the axis at about 110°W. The larger amplitudes of the spatial EOF in Fig. 4.2a are observed in the northeast, north of 40°S and between 140–90°W, and in a localized region southeast of New Zealand. North of the zero contour line sea level increases to a

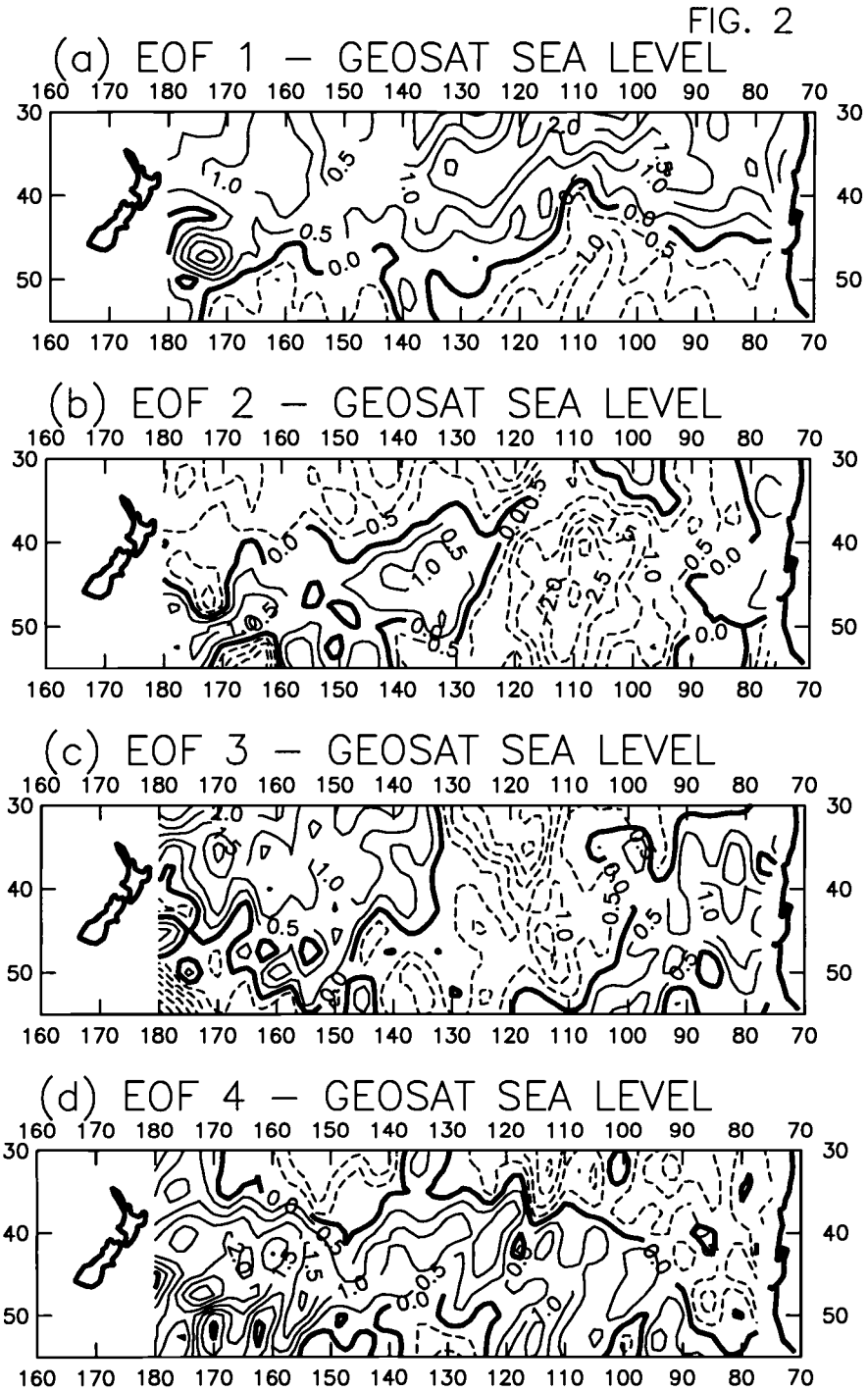

FIGURE 4.2. The spatial patterns of the first four EOFs of Geosat sea level variability in the South Pacific. The functions have been normalized so that their mean square value over all the grid points is equal to one. Negative contours are indicated with dashed lines and the contour interval is 0.5.

FIG. 3

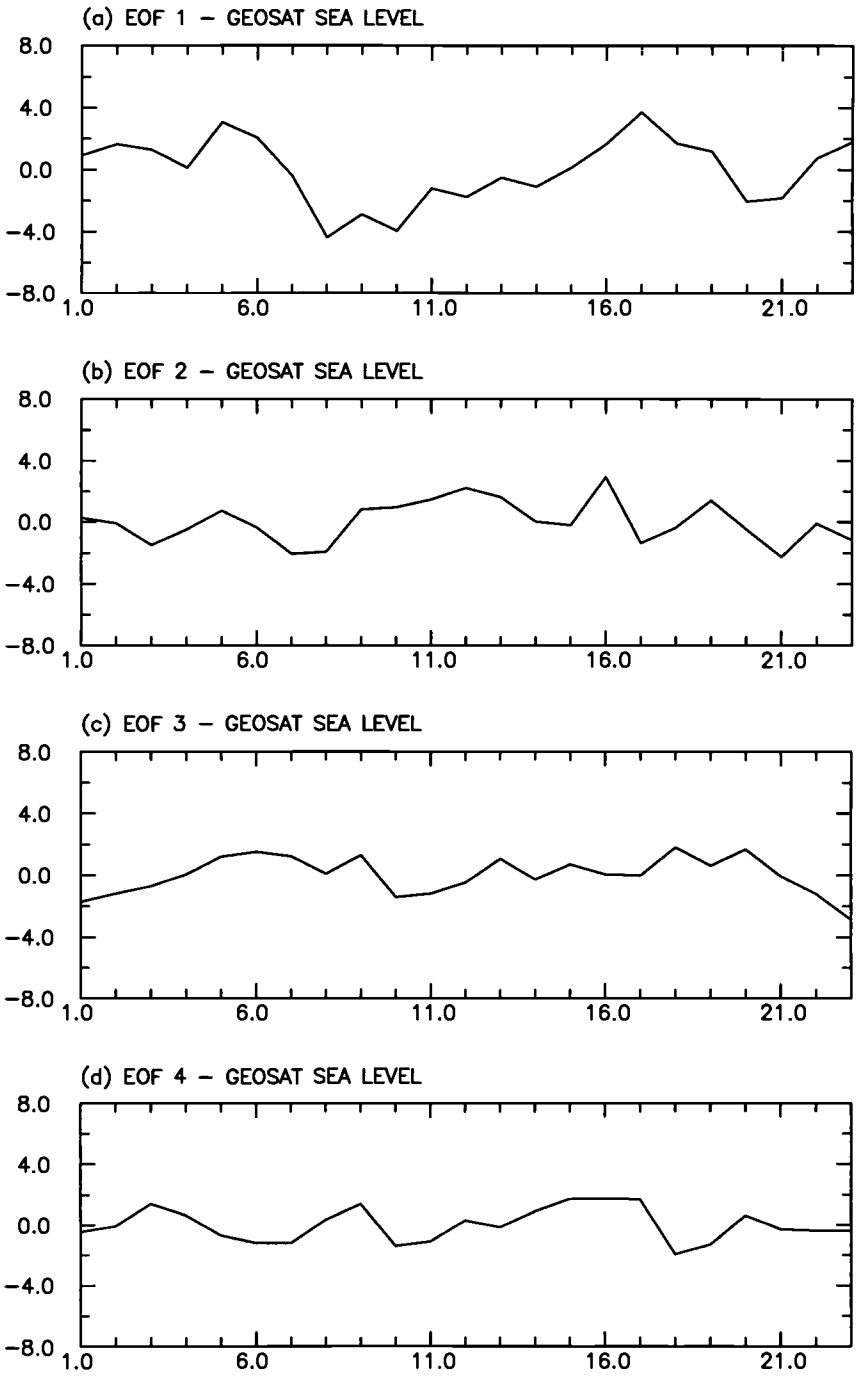

FIGURE 4.3. The amplitude time series of the first four EOFs of Geosat sea level variability in centimeters versus time in months.

maximum around April-May and decreases to a minimum around July-August. The opposite happens at higher latitudes. The rms variability of the first amplitude time series (Fig. 4.3a) is 2.1 cm (range = -4.4 cm to 3.7 cm). This meridional oscillation can be interpreted as seasonal accelerations and decelerations of the generally zonal eastward flow of the South Pacific, as suggested by Chelton et al. (1990).

The second empirical mode of Geosat sea level (Figs. 4.2b and 4.3b) explains 12% of the total variance (Table 4.1). Its spatial pattern (Fig. 4.2b) looks like a zonal oscillation with a high to the west and a low of larger amplitude to the east. Compared to the first amplitude time series (Fig. 4.3a) the second (Fig. 3b) contains more small-scale variability, does not show a dominant seasonal cycle and has smaller amplitudes. The rms variability of the second amplitude time series is 1.3 cm (range = -2.2 cm to 2.9 cm). Physical interpretation of this and higher order empirical modes is more difficult because of the orthogonality condition of the EOFs.

The third empirical mode of Geosat sea level (Figs. 4.2c and 4.3c) explains 9% of the total variance (Table 4.1). Its spatial pattern (Fig. 4.2c) shows a zonal oscillation, with two highs to the west and east separated by a low near the center of the domain. The rms variability of the third amplitude time series (Fig.4.3c)) is 1.2 cm (range = -2.9 cm to 1.8 cm).

The fourth empirical modes of Geosat sea level (Figs. 4.2d and 4.3d) explains 8% of the total variance (Table 4.1). Its spatial pattern (Fig. 4.2d) shows a nearly-meridional oscillation with the axis tilting northward from the southeast to the northwest corners of the domain. The larger amplitudes are in the region southeast of New Zealand. The fourth amplitude time series (Fig. 4.3d) particularly during the first year looks like a semiannual oscillation with maxima in February and August.

The rms variability of the fourth amplitude time series is 1.1 cm (range = -1.9 cm to 1.7 cm).

4.5.3. Wind Stress Curl

The spatial patterns of the first four EOFs of the curl are shown in Fig. 4.4 and their associated time series in Fig. 4.5. The spatial and temporal correlations between the curl and Geosat EOFs are shown in Table 4.2 and Table 4.3 (columns labeled Curl).

TABLE 4.2. Spatial sample correlations (±1 standard deviation uncertainties, computed as explained in the text)

EOF	Curl	Sv.	NRL	SC
1	0.50±0.08	0.43±0.07	0.62±0.07	0.56±0.09
2	0.32±0.11	0.37±0.08	0.31±0.10	0.52±0.10
3	(-0.09±0.12)	(0.09±0.12)	(-0.04±0.15)	(0.09±0.12)
4	(-0.12±0.11)	0.25±0.10	0.26±0.12	0.26±0.10

TABLE 4.3. Temporal sample correlations (±1 standard deviation uncertainties, computed as explained in the text)

EOF	Curl	Sv.	NRL	SC
1	0.56±0.13	0.73±0.10	0.71±0.13	0.89±0.04
2	0.56±0.18	(0.34±0.22)	0.65±0.11	0.65±0.13
3	(0.23±0.24)	0.44±0.18	(0.11±0.22)	0.43±0.20
4	(0.19±0.21)	0.56±0.15	(0.28±0.21)	0.43±0.14

The first mode of the curl (Figs. 4.4a and 4.5a) accounts for 27% of the total variance (Table 4.1) and resembles the meridional seasonal oscillation described by

FIG. 4

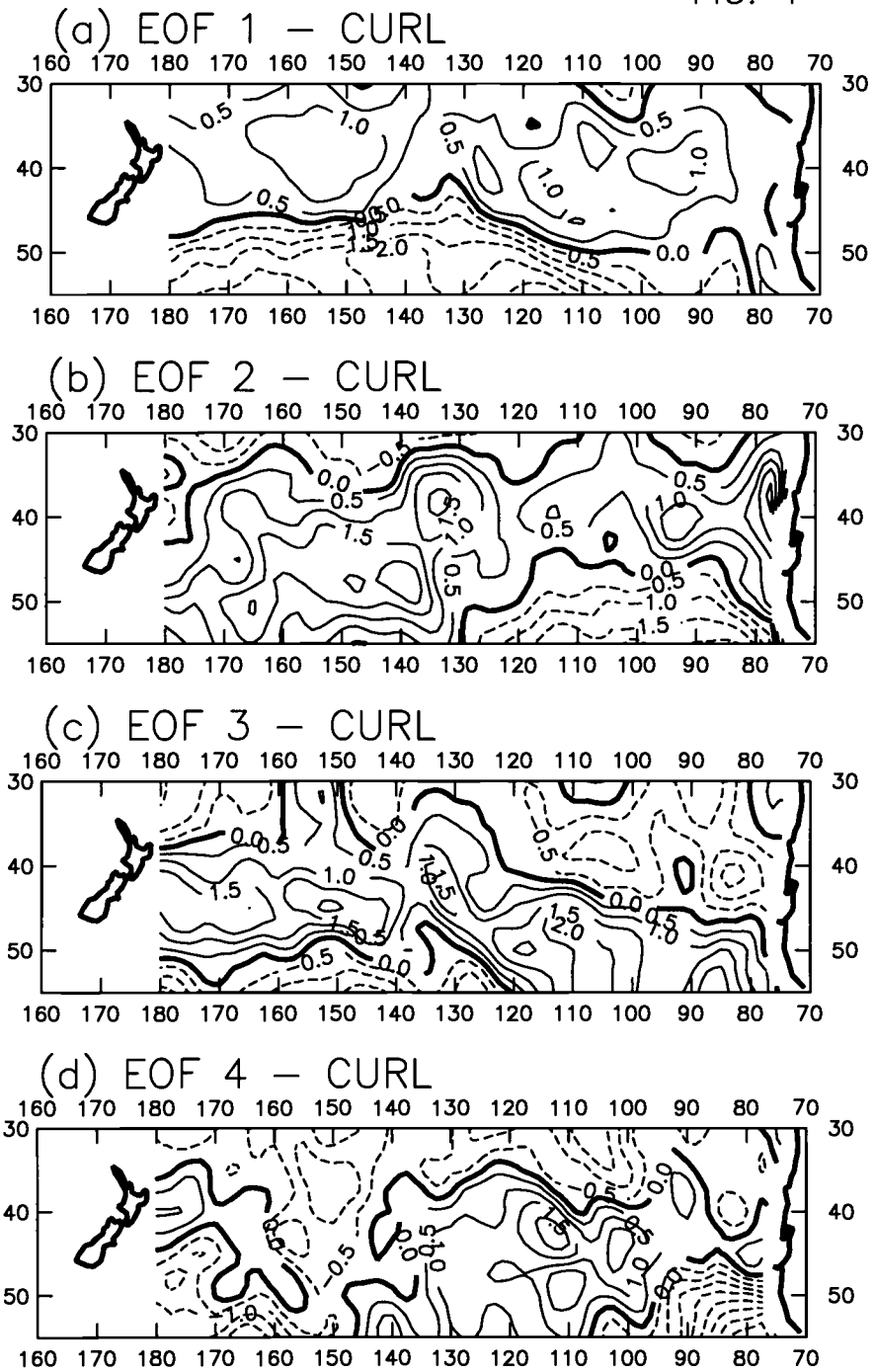

FIGURE 4.4. Same as Fig. 4.2 but for wind stress curl.

FIG. 5

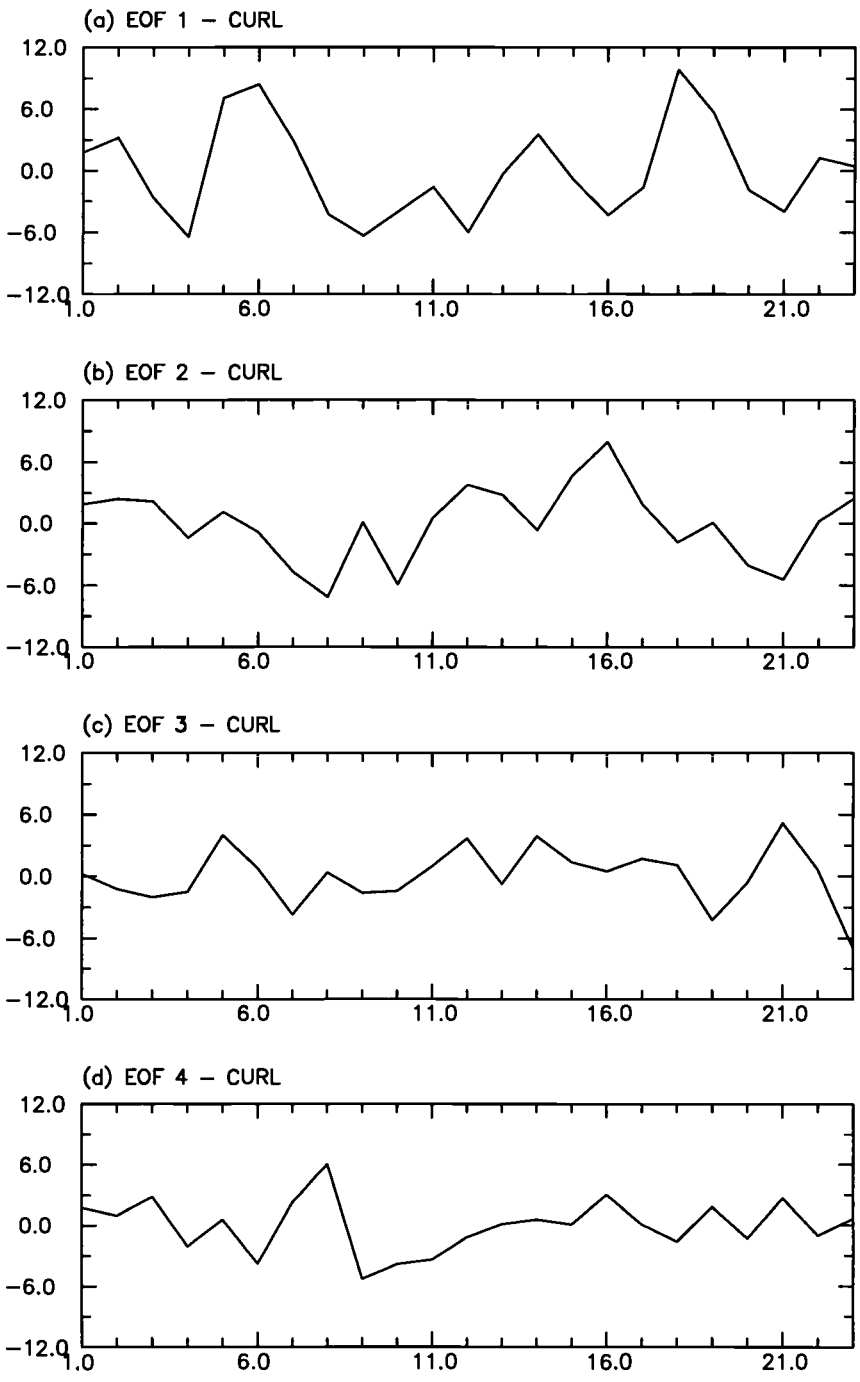

FIGURE 4.5. Same as Fig. 4.3 but for wind stress curl in 10^{-9} dyn/cm^3.

the first mode of Geosat sea level in Figs. 4.2a and 4.3a. The spatial and temporal correlations (± 1 standard deviation calculated following Effron 1979) between the first mode of Geosat and curl are 0.50 ± 0.08 and 0.56 ± 0.13. Because the 99.7% confidence interval on the sample correlation is approximately three times the standard deviation, the spatial and temporal sample correlations of the first mode are statistically significant with greater than 99.7% confidence. These high correlations suggest that the first mode of Geosat sea level may be interpreted as a basin-scale seasonal response to wind forcing. However, significant correlation alone is not sufficient to imply causality. The correlation between sea level and curl ought to be supported by the analysis of sea level from the theory and the wind-driven models.

Despite the significant correlation between the first modes of curl and Geosat, there are noticeable differences in the spatial patterns and in the amplitude time series. The spatial pattern of curl (Fig. 4.4a) has larger amplitudes in the southwest (absolute values greater than 2) rather that in the northeast, there is not a northward displacement in the zero contour line at 110°W, and there is not a localized maximum southeast of New Zealand. Regarding the differences in the amplitude time series, the curl (Fig. 4.5a) is more noisy than Geosat (Fig. 4.3a).

The second mode of wind stress curl (Figs. 4.4b and 4.5b) accounts for 16% of the total variance (Table 4.1). The spatial and temporal correlations between the second EOF of curl and Geosat are 0.32 ± 0.11 and 0.56 ± 0.18. Some suggestion of a wind-driven sea level response for the second Geosat mode can also be made because both of these correlations are significant at the 95.5% level. However, only the temporal correlation is significant at the 99.7% level.

The third (Figs. 4.4c and 4.5c) and fourth (Figs. 4.4d and 4.5d) modes of wind stress curl account for 10% and 8% of the total variance (Table 4.1). Neither the spatial pattern nor the time series of these modes compare well with their pairs

for Geosat sea level. The spatial and temporal correlations of the third mode of the curl with the third mode of Geosat are -0.09±0.12 and 0.23±0.24. The spatial and temporal correlations of the fourth mode of the curl with the fourth mode of Geosat are -0.12 ±0.11 and 0.19±0.21. Thus, these correlations are not significant with 95.5% confidence.

4.5.4. Sverdrup Sea Level

The four most significant EOFs of Sverdrup sea level are shown in Fig. 4.6 and their associated time series in Fig. 4.7. For comparison, the corresponding Geosat amplitude time series are also shown in Fig. 4.7 (dashed lines). The spatial and temporal correlations between the Sverdrup and Geosat EOFs are shown in Table 4.2 and Table 4.3 (columns labeled Sverdrup).

The first mode of Sverdrup sea level (Figs. 4.6a and 4.7a) accounts for 63% of the variance (Table 4.1). It shows a meridional seasonal oscillation similar to the first modes of Geosat sea level (Figs. 2a and 3a) and wind stress curl (Figs. 4.4a and 4.5a). The spatial and temporal correlations with the first mode of Geosat sea level are 0.43±0.07 and 0.73±0.10. These correlations are significant with greater than 99.7% confidence suggesting an interpretation of the first mode of Geosat sea level as a simple Sverdrup response. However, unlike Geosat, the Sverdrup space pattern is much smoother, has amplitudes that increase linearly from east to west, and is unable to describe the northward deviation of the zero contour line at 110°W. Furthermore, the sea level amplitudes of the first Sverdrup amplitude time series (Fig. 4.7a, solid line) are too large compared to Geosat (Fig. 4.7a, dashed line). The rms variability of the Sverdrup amplitude time series is 3.3 cm (range = -5.6 cm to 5.3 cm) which is about 57% larger than the rms variability of Geosat.

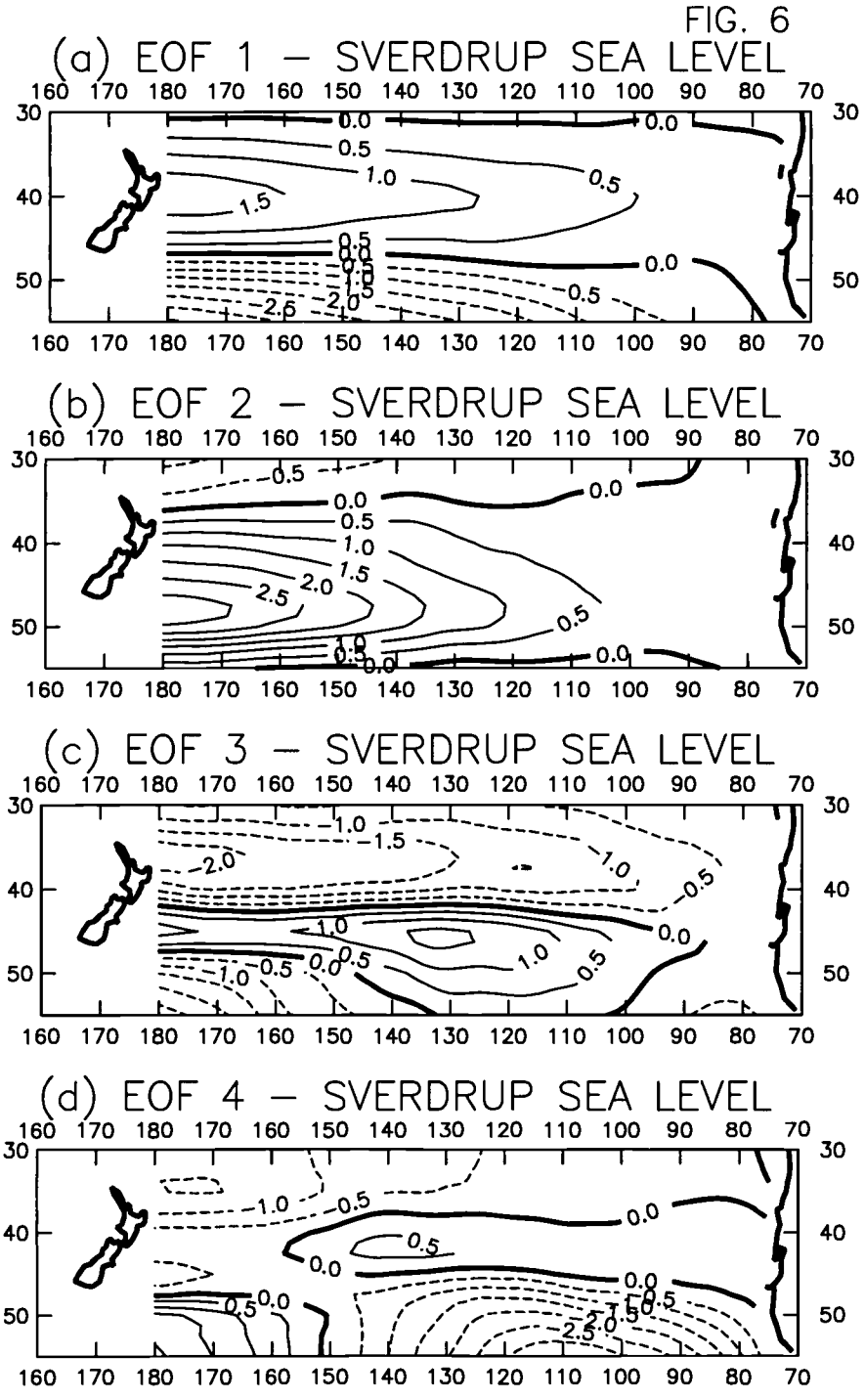

FIGURE 4.6. Same as Fig. 2 but for Sverdrup sea level.

FIG. 7

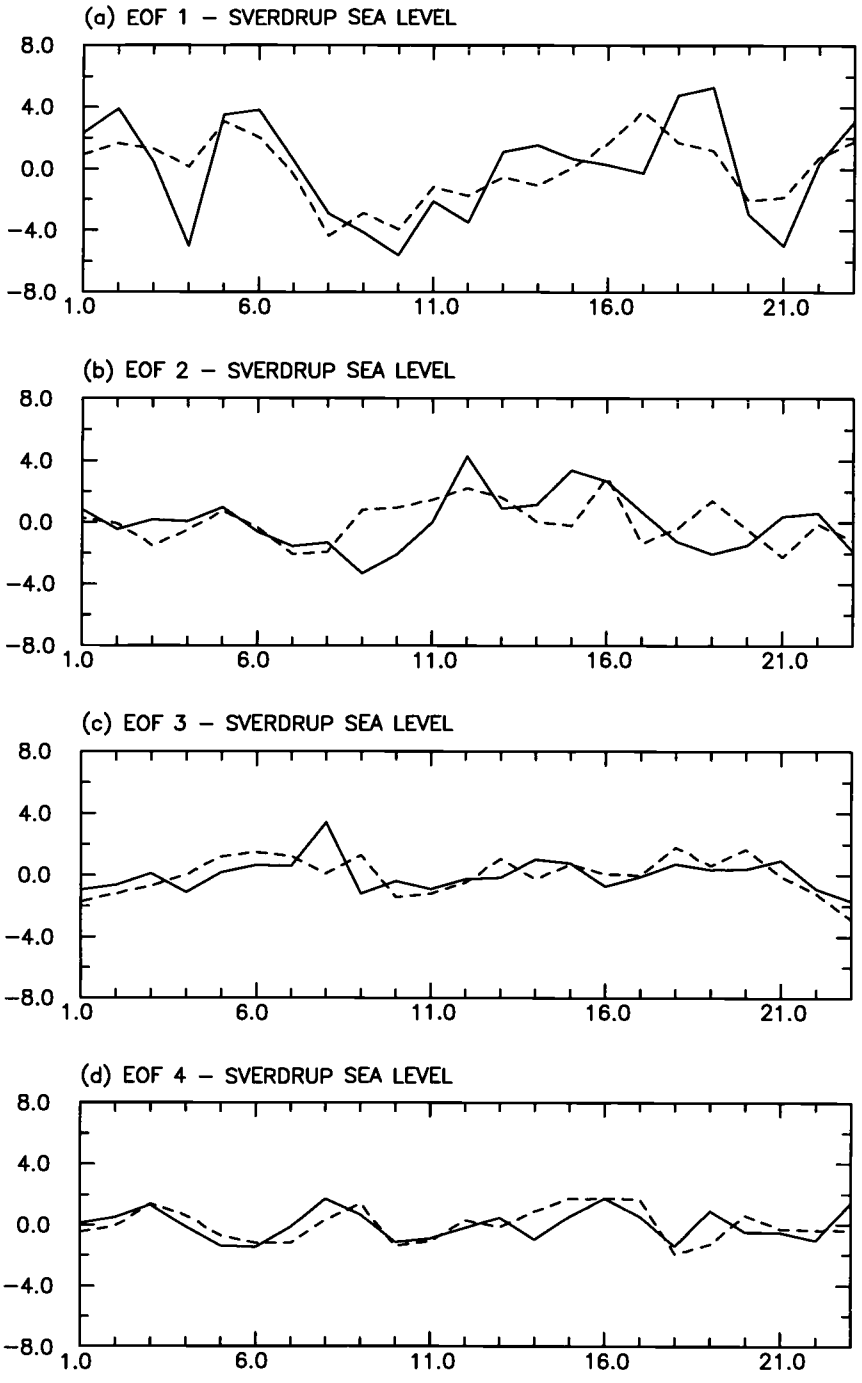

FIGURE 4.7. The amplitude time series of the first four empirical orthogonal functions (EOFs) of Sverdrup sea level variability in centimeters (solid lines). For comparison, the first four amplitude time series of Geosat sea level shown in Fig. 3 are superimposed as dashed lines.

We note that in the Seasat study (Mestas-Nuñez et al. 1992) the amplitude of the sea level estimates were about three times larger than those actually observed. This discrepancy may be slightly overestimated because the Seasat stresses should have been increased by about 7% to account for scatterometer sampling errors as suggested by Mestas-Nuñez et al. (1994).

The second mode of Sverdrup sea level (Figs. 4.6b and 4.7b) accounts for 19% of the total variance (Table 4.1). The spatial and temporal correlations between the second mode of Sverdrup and Geosat sea level are 0.37±0.08 and 0.34±0.22. Thus, only the spatial correlation is significant at the 95.5% level. The rms variability of the Sverdrup second amplitude time series (Fig. 4.7b, solid line) is 1.8 cm (range = -3.3 to 4.3 cm) which is about 38% larger than the rms variability of Geosat (Fig. 4.7b, dashed line).

The third (Figs. 4.6c and 4.7c) and fourth (Figs. 4.6d and 4.7d) modes of Sverdrup sea level, each accounts for the same fraction (6%) of total variance (Table 4.1). Their correlation with Geosat is somewhat better in time than in space. The spatial correlations of the third and fourth mode are 0.09±0.12 and 0.25±0.10. Thus, the spatial correlation of only the fourth mode is significant at the 95.5% level but neither of them are significant at the 99.7% level. The temporal correlations of the third and fourth mode are 0.44±0.18 and 0.56±0.15. Both of them are significant at the 95.5% level but only the fourth mode is significant at the 99.7% level.

4.5.5. NRL Sea Level

The four most significant EOFs of NRL sea level are shown in Fig. 4.8 and their associated time series in Fig. 4.9 (solid lines). For comparison, the corresponding Geosat amplitude time series are also shown in Fig. 4.9 (dashed lines). The

spatial and temporal correlations between the NRL and Geosat EOFs are shown in Table 4.2 and Table 4.3 (columns labeled NRL).

The first mode of NRL sea level (Figs. 4.8a and 4.9a) accounts for 43% of the total variance (Table 4.1). Its shows a meridional seasonal oscillation similar to the observed in Geosat sea level (Figs. 4.2a and 4.3a), wind stress curl (Figs. 4.4a and 4.5a), and Sverdrup sea level (Figs. 4.6a and 4.7a). The spatial and temporal correlations with the first mode of Geosat sea level are 0.62±0.07 (Table 4.2) and 0.71±0.13 (Table 4.3). As in the comparison with the first mode of the Sverdrup theory, these correlations are significant with greater than 99.7% confidence, supporting the interpretation of the first mode of Geosat as wind driven. However, the location of the axis of meridional variability of the first Geosat mode is described better by NRL than by Sverdrup. The northward excursion of the zero contour line at 110°W (Fig. 4.8a) brakes the simple zonal structure of the Sverdrup pattern (Fig. 4.6a) in two, although the tendency for amplitudes to increase from east to west is still present and is more noticeable in the western region.

The amplitude of the first amplitude time series of Geosat sea level is also described better by the NRL model than by the Sverdrup theory. The rms variability of the first amplitude time series of NRL sea level (Fig. 4.9a, solid line) is 2.2 cm (range = -6.3 cm to 2.8 cm) which is only 5% larger than the rms variability of Geosat (Fig. 4.9a, dashed line). We recall that the standard deviation of the first amplitude time series predicted by the Sverdrup theory was 57% larger than the observed by Geosat. Although the Sverdrup theory and the NRL model have been forced with winds based on ECMWF analyses, the techniques used to calculate the stress are different (see section 2). Thus, some of the differences in amplitude between Sverdrup and NRL sea level may be due to systematic differences in the wind forcing.

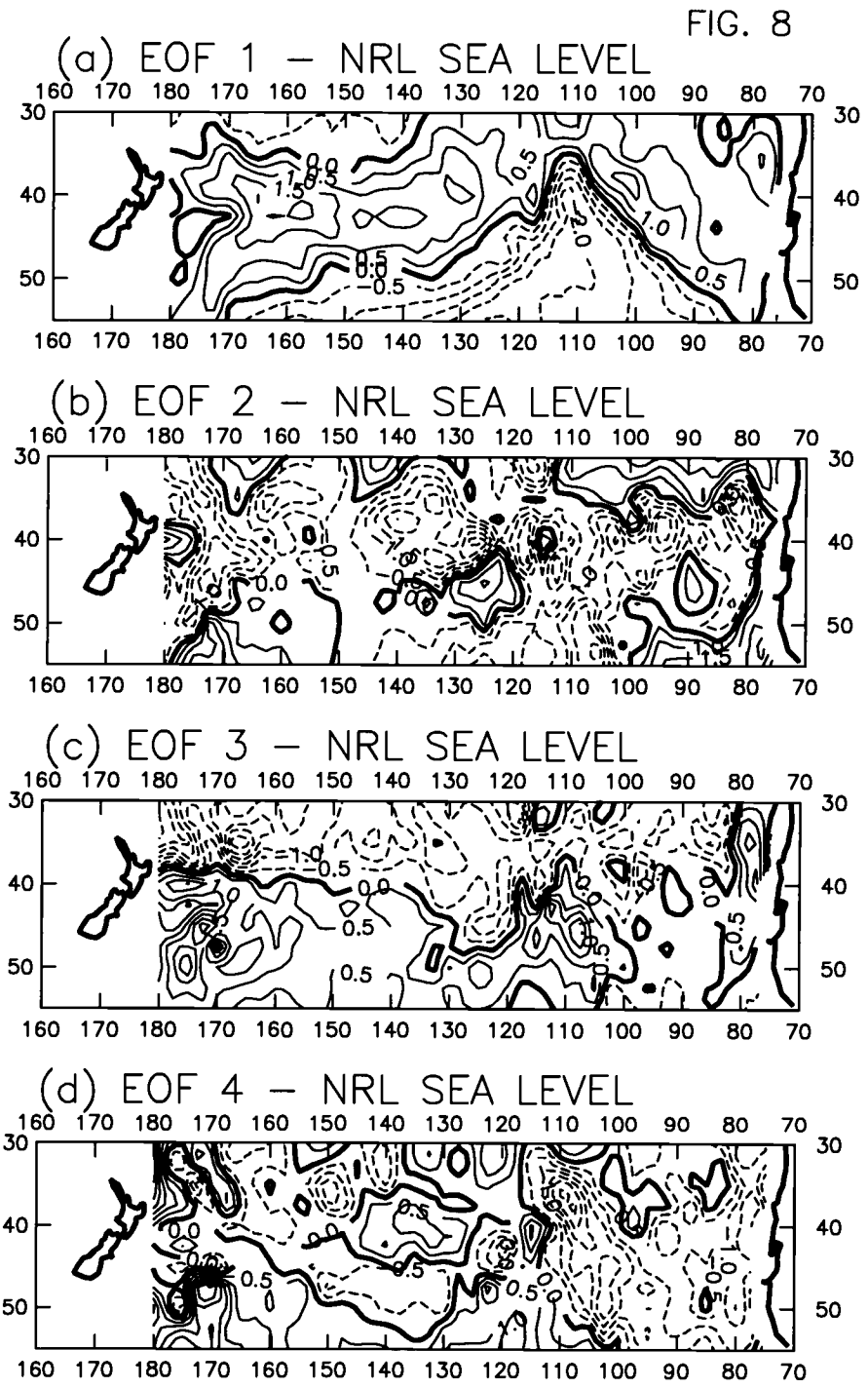

FIGURE 4.8. Same as Fig. 4.2 but for sea level from the NRL model.

FIG. 9

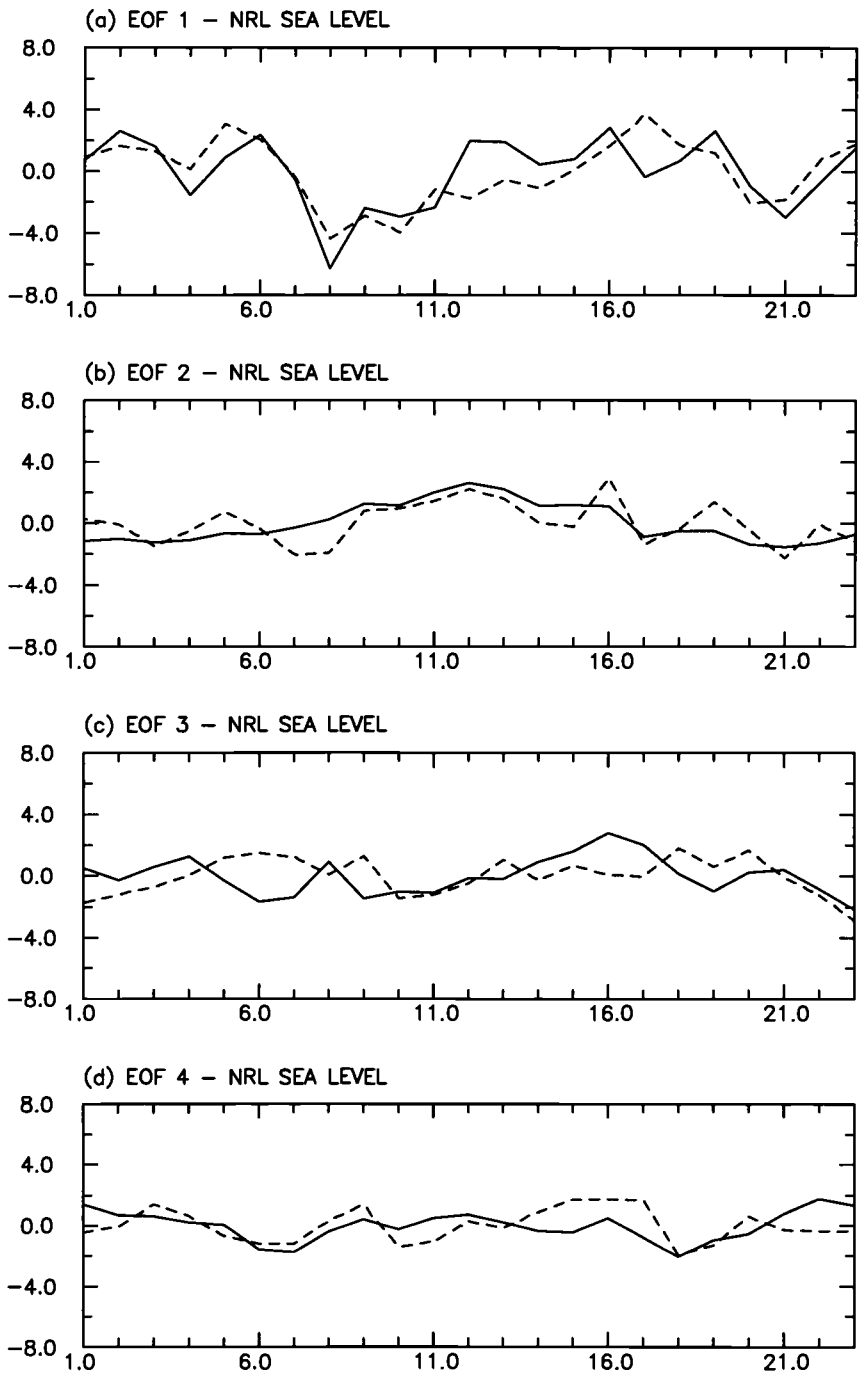

FIGURE 4.9. Same as Fig. 4.7 but for NRL sea level.

The second mode of NRL sea level (Figs. 4.8b and 4.9b) accounts for 14% of the total variance (Table 4.1). The spatial and temporal correlations between the second mode of NRL and Geosat sea level are 0.31±0.10 (Table 4.2) and 0.65±0.11 (Table 4.3). Thus, both correlations are significant at the 99.7% level. The second NRL spatial pattern (Fig. 4.8b) is similar to the second spatial pattern of Geosat sea level (Fig. 4.2b). The rms variability of the second NRL amplitude time series (Fig. 4.9b, solid line) is 1.3 cm (range = -1.5 to 2.6 cm) which is equal to the rms variability of the second Geosat time series (Fig. 4.9b, dashed line).

The third (Figs. 4.8c and 4.9c) and fourth (Figs. 4.8d and 4.9d) modes of NRL sea level account for 13% and 8% of the total variance (Table 4.1). Their spatial correlations with Geosat sea level are -0.04±0.15 and 0.26±0.12 (Table 4.2). Thus, the spatial correlation of only the fourth mode is significant at the 95.5% level but neither of them are significant at the 99.7% level. The temporal correlations of the third and fourth mode are 0.11±0.22 and 0.28±0.21 and none of them are significant at the 95.5% level (Table 4.3).

4.5.6. SC Sea Level

The four most significant EOFs of SC sea level are shown in Fig. 4.10 and their associated time series in Fig. 4.11 (solid lines). For comparison, the corresponding Geosat amplitude time series are also shown in Fig. 4.11 (dashed lines). The spatial and temporal correlations between the SC and Geosat EOFs are shown in Table 4.2 and Table 4.3 (columns labeled SC).

The first mode of SC sea level (Fig. 4.10a and 4.11a) accounts for 25% of the variance (Table 4.1). Its spatial pattern (Fig. 4.10a) shows a meridional seasonal oscillation similar to the observed in the first mode of all the other fields (Figs. 4.2a

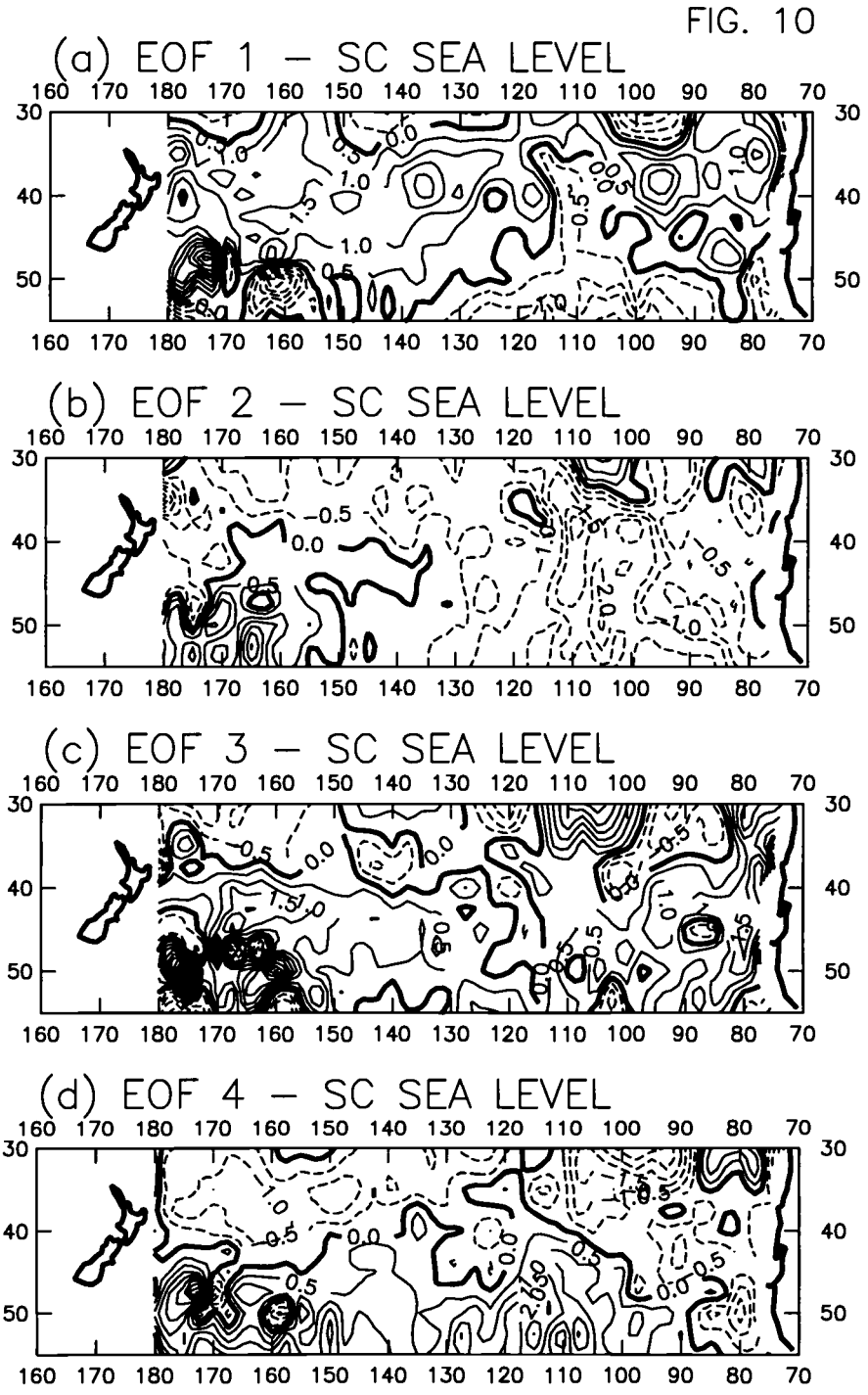

FIGURE 4.10. Same as Fig. 4.2 but for sea level from the SC model.

FIG. 11

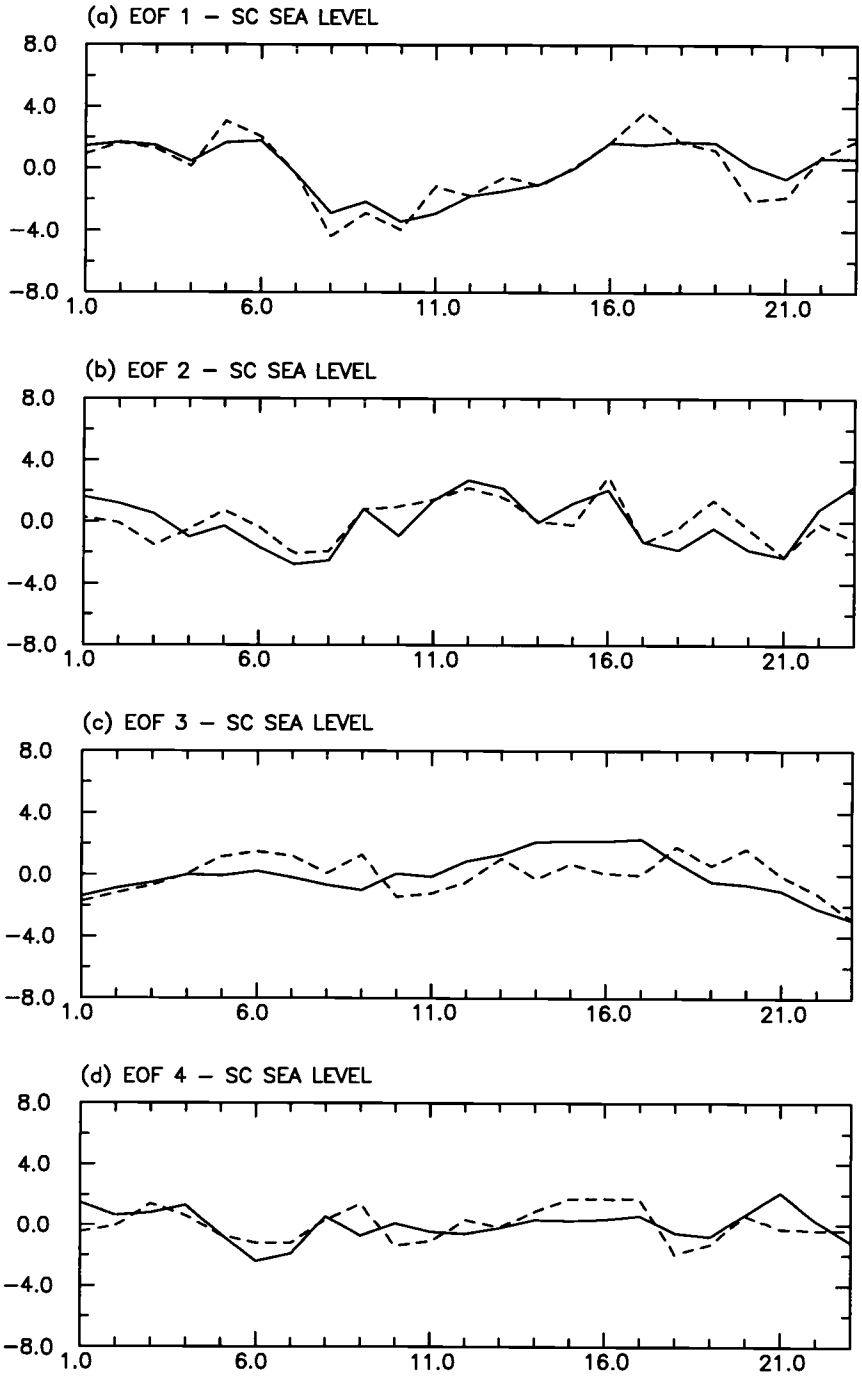

FIGURE 4.11. Same as Fig. 4.7 but for SC sea level.

and 4.3a to Figs. 4.8a and 4.9a) The spatial and temporal correlations with the first mode of Geosat are 0.56±0.09 (Table 4.2) and 0.89±0.04 (Table 4.3). Thus, these correlations are significant with greater than 99.7% confidence, as found in the analysis of the curl and the other simulated sea level fields. As noted in section 2.4, the SC model includes seasonal thermal forcing at the surface in our region of interest. However, the meridional spatial scales of the first SC spatial pattern compare well with the scales of the wind forcing, which are much smaller than the meridional scales (hemispheric) of the heating-cooling forcing pattern. Thus, the SC model also supports the interpretation of the first EOF of Geosat as a wind-driven response.

Similar to NRL, the SC first spatial pattern also shows the northward displacement of the zero contour line at 110°W which was observed by Geosat but not described by the Sverdrup theory. Unlike Sverdrup and NRL but similar to Geosat, the larger amplitudes of the SC first spatial pattern are in the northeast (east of 140°W and north of 40°S) and in the region southeast of New Zealand. Therefore, although the spatial correlations of the SC and NRL first mode with Geosat are not significantly different, the SC spatial pattern appears more consistent with Geosat.

The rms variability of the first SC amplitude time series (Fig. 4.11a, solid line) is 1.7 cm (range = -3.4 cm to 1.8 cm) which is 19% smaller than the observed by Geosat (Fig. 4.11a, dashed line). Thus, SC does better than Sverdrup but not as good as NRL in estimating the rms variability of the first amplitude time series of Geosat. However, as in the NRL case, some of the differences between the SC and Sverdrup amplitudes could be the result of systematic differences in the wind stresses (see section 2). The technique used to derive the SC stresses based on the Trenberth et al. (1990) approach, give winds that are too strong by about 50% when ECMWF analyses for the 1980-1986 period are used (Mestas-Nuñez et al.

1994). However, the accuracy of the ECMWF stresses for the Geosat period have not been determined.

The second mode of SC sea level (Figs. 4.10b and 4.11b) accounts for 24% of the total variance (Table 4.1). The spatial and temporal correlations between the second mode of SC and Geosat sea level are 0.52±0.10 (Table 4.2) and 0.65±0.13 (Table 4.3). Thus, both of these correlations are significant with greater than 99.7% confidence. The second SC spatial pattern (Fig. 4.10b) is similar to the second spatial pattern of Geosat sea level (Fig. 4.2b). However, the region of high amplitude in the second spatial pattern located in the western basin is more localized in SC than in Geosat. The rms variability of the second amplitude time series of SC sea level is 1.7 cm (range = -2.8 to 2.7 cm) which is about 31% larger than the rms variability of the second amplitude time series of Geosat.

The third (Figs. 4.10c and 4.11c) and fourth (Figs. 4.10d and 4.11d) modes of SC sea level account for 16% and 9% of the total variance (Table 4.1). Their spatial correlations with Geosat sea level are 0.09±0.12 and 0.26±0.10. Thus, the spatial correlation of only the fourth mode is significant with 95.5% confidence but neither of them are significant at the 99.7% level. Their temporal correlations with Geosat sea level are 0.43±0.20 and 0.43±0.14. Thus, both temporal correlations are significant with 95.5% confidence but the temporal correlation of only the fourth mode is significant with 99.7% confidence. We conclude that the third and fourth modes of SC sea level are better correlated in time than in space with the third and fourth modes of Geosat sea level.

4.6. Discussion

We have performed an EOF analysis of Geosat sea level observations, ECMWF wind stress curl, and sea level from Sverdrup theory and two models (NRL, and SC) for the period December 1986 to October 1988 in the South Pacific. It was shown that Geosat sea level and wind stress curl present similar distributions of variance with EOF mode number (Fig. 4.1). In both fields the variance was spread over a large number of modes, illustrating the complicated nature of sea level and curl variability at mid latitudes in the South Pacific. These results are consistent with EOF analysis of sea level in the Southern Ocean (Chelton et al. 1990) and of wind stress curl in the North Atlantic (Barnier 1986; Ehret and O'Brien 1989). Among the simulated sea level fields considered in this study, Sverdrup produced the distribution of variance that differed the most, and SC the distribution that was closest to the distribution of Geosat. These results are encouraging because the sea level simulations are organized in a sequence of increasing realism. While the theory and the models are wind driven, the Sverdrup theory assumes barotropic flow with flat bottom and does not contemplate transient motions. The NRL model has stratification with topography and allows transient motions associated with the barotropic as well as the first 5 baroclinic modes. Finally, the SC model adds stratification with greater vertical resolution and thermal forcing. Neither the theory nor the models, however, produced a distribution of variance that compared well with Geosat, illustrating the shortcomings of theory and models in describing the observed variance spectrum of sea level variability.

For modes higher than the first, some correlation between Geosat sea level and the other variables studied here was found, with temporal correlations generally larger than spatial correlations. Only for the first mode were both the temporal and

spatial correlations between Geosat and the other fields significant with greater than 99.7% confidence. Considering that modes higher than the first are affected by the orthogonality conditions, we concentrate our discussion on the first mode and discuss the implications of the high correlations.

The empirical correlation between the basin-scale seasonal oscillation, captured by the first EOF of Geosat sea level and the first EOF of wind stress curl, may indicate that this mode is a wind-driven response. However, there is no theoretical basis for this interpretation. In the topographic Sverdrup balance proposed by Gill and Niiler (1973), a correlation between the curl and the gradient of sea level along f/H contours is expected. However, as noted earlier the topographic Sverdrup balance is not appropriate in the South Pacific because of the closed f/H contours. On the other hand, the simple flat-bottom barotropic Sverdrup balance discussed by Mestas-Nuñez et al. (1992) predicts correlation between the curl and the zonal gradient of sea level. However, since the dominant pattern of the curl variability is zonally coherent (Fig. 4.4a) a correlation between the first modes of Geosat and flat-bottom Sverdrup sea level should also be expected.

The correlation between the first model of Geosat and Sverdrup sea level suggests the validity of simple Sverdrup dynamics. However, the Sverdrup theory does not reproduces the northward shift of the zero contour line at 110°W and the smaller scale structure present in the first mode of Geosat (Fig. 4.2a). This structure is better described by the first spatial pattern of NRL (Fig. 4.8a) and SC (Fig. 4.10a) models. However, the SC model describes better the spatial distribution of amplitudes of the first Geosat spatial pattern than the NRL model. A map of bottom topography in Fig. 4.12 shows that the location of the northward shift of the zero contour line in the first spatial patterns coincides with the location of the East Pacific Rise with depths smaller than 3000m. Thus, the absence of this structure in

FIG. 12

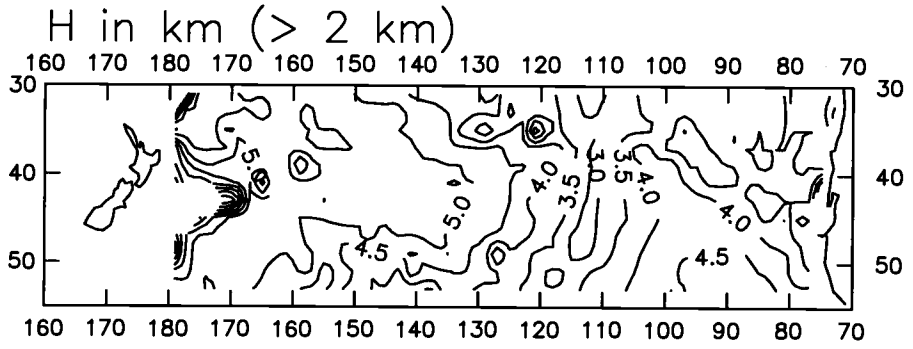

FIGURE 4.12. Topography of the ocean bottom in the South Pacific in kilometers. Depths shallower than 2 km are not shown and the contour interval is 0.5 km.

the first mode of Sverdrup sea level may be a result of neglecting bottom topography in the Sverdrup theory. We have also looked at data from a reduced gravity version of the NRL model and found that the first four EOFs compared poorly with Geosat. Therefore we reported only the results for the finite depth case. It appears then that the oscillation shown by the first empirical mode of Geosat sea level is dominated by the barotropic vertical mode and the change in orientation of its axis related to bottom topography.

Regarding the amplitude time series of the first mode, the Sverdrup theory and the NRL model showed higher rms variability than Geosat. The first SC time series compared remarkably well with the first Geosat time series but the rms variability was slightly smaller than the observed. We recall that the SC model has

been forced with the strongest wind stress. While the Sverdrup theory wind stress was adjusted for differences between ECMWF 1000 mb and 10 m winds that may result in monthly stresses about 45% too strong (Mestas-Nuñez et al. 1994), the NRL and SC wind stress forcings were not. The NRL wind forcing is weaker than the SC wind forcing because of the replacement of the ECMWF temporal mean with the Hellerman and Rosenstein mean, which is about 10% (instead of 45%) too strong (Mestas-Nuñez et al. 1994). That the rms variability of the first SC mode is smaller than Geosat, even though the SC model uses wind forcing that is too strong, may be an indication that the SC model is too dissipative. Recent comparisons with observations have shown that an earlier version of the SC model (Semtner and Chervin 1992) underestimates eddy kinetic energy by typically a factor of four over the Southern Ocean (Wilkin and Morrow 1994). This was interpreted as mainly inadequate horizontal model resolution, however, it may be another indication that the model dissipation is too high.

The correlation between the first EOF of Geosat and curl could be interpreted as the result of errors in the inverse barometer correction in the altimetric observations. However, the fact that the first mode can be reproduced by the two numerical models which do not include pressure forcing indicates that this is not the case. The correlations with the NRL and SC models suggest that the first EOF of Geosat sea level is a wind-driven response. We noted that the SC model is also driven by seasonal surface heating. It appears then that the SC first EOF at these latitudes in the South Pacific is not representating a thermal response.

In conclusion, the analysis suggests that the large-scale zonally coherent Geosat sea level variability, captured by the first EOF, may be interpreted as a response of the South Pacific to seasonal changes in the wind forcing. The dominant physical mechanisms appear to be a barotropic response of a stratified ocean

over topography. Seasonal thermal heating and cooling does not seem to be a major component of the response, apparently because the orbital removal applied to the Geosat data may have removed most of this signal. At present, high quality sea level observations from the TOPEX/POSEIDON altimeter are becoming available. The results of the Geosat study can be checked with the TOPEX/POSEIDON data.

Acknowledgements. We are indebted to M. Schlax for generating the smoothed Geosat data set and for sharing his EOF calculation routine, to J. Metzger and H. Hurlburt for providing the NRL model output, and to A. Semtner and R. Tokmakian for providing the SC model output. Technical assistance by E. Beals and D. Goff and helpful conversations with D. Dietrich and H. Hurlburt are also acknowledged.

5. WIND-FORCED VARIABILITY IN THE WESTERN NORTH PACIFIC

Alberto M. Mestas-Nuñez

College of Oceanic and Atmospheric Sciences
Oregon State University, Corvallis, OR 97331

5.1. Abstract

The large-scale, wind-forced circulation in the North Pacific during the period October 1992–June 1994 is investigated from simple flat-bottom, time-dependent Sverdrup theory. The results are compared with the vertically integrated transport streamfunction of the global ocean general circulation model developed by the Parallel Ocean Program (POP) of the Los Alamos National Laboratory and with sea level observations from the TOPEX/POSEIDON (TP) altimeter. Despite the simplicity of the Sverdrup theory, it yields large-scale low-frequency transport variations very similar to the POP model. Both theory and model predict maximum flow of the Oyashio, Kuroshio (including their recirculations) and Kuroshio Extension in the winter and minimum flow in the summer/fall. The correlations between the two estimates of the transport variations are between 0.8–0.9, indicating that simple Sverdrup dynamics account for 65–80% of the low-frequency transport variability of the POP model in the western North Pacific. The sea level differences across the Kuroshio and Kuroshio Extension predicted from the Sverdrup theory assuming geostrophic and barotropic flow compare favorably with sea level differences observed by the TP altimeter. The correlation between Sverdrup and TP sea level variations are between 0.5–0.9, indicating that time-dependent Sverdrup dynamics account for about 25–80% of the observed low-frequency variability.

5.2. Introduction

The mean circulation in the upper layers of Northern Hemisphere extratropical oceans consists of double-gyre systems with an anticyclonic subtropical gyre south of about 35°N and a cyclonic subpolar gyre to the north. This structure is mainly the result of the large-scale wind forcing. The simplest dynamical explanation for these features is that they exist because of the Sverdrup balance between the input of vorticity from the surface wind stress curl and the advection of planetary vorticity in the water column (the beta term in the vorticity equation) (Sverdrup 1947). This balance can be described in terms of potential vorticity or f/H conservation of the large-scale flow, where f is the coriolis parameter and H the mean depth of the ocean. In the subtropics, the mean wind stress curl forcing is negative (Fig. 5.1) which induces a negative vertical velocity at the bottom of the Ekman layer. This downward flow squashes the underlying water columns and, in order to conserve potential vorticity, water columns are forced to move southward (Fig. 5.2). The opposite occurs at higher latitudes where the mean wind stress curl is positive, which forces a northward Sverdrup transport of water columns across the interior basin. The interior Sverdrup transports are balanced by narrow western boundary currents in order to conserve mass and close the circulation gyres (Stommel 1948; Munk 1950).

In the subtropical North Pacific, the Sverdrup balance for the mean flow has been shown to hold by comparison with geostrophic transport calculations from a basin-wide hydrographic section along 24°N (Hautala et al. 1994). In contrast, the observed geostrophic transport along 24°N in the subtropical North Atlantic agrees with the prediction of the Sverdrup balance only east of 55–60°W (Schmitz et al. 1992). Hautala et al. gave several reasons to expect the Pacific to be more

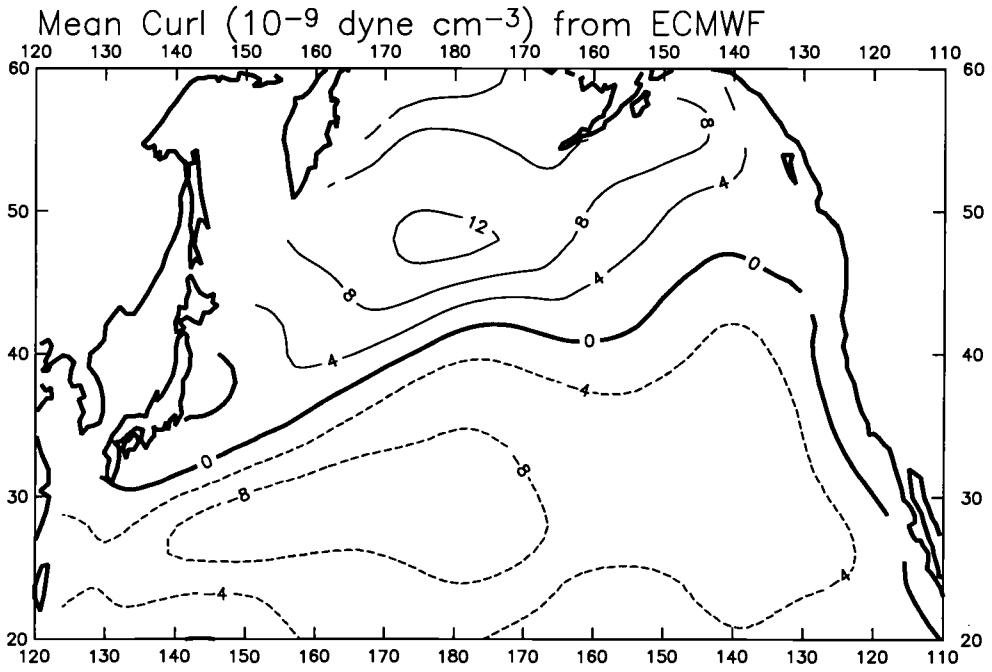

FIGURE 5.1. Mean wind stress curl (10^{-9} dyn/cm^3) in the North Pacific calculated from ECMWF winds for the period October 1992–June 1994.

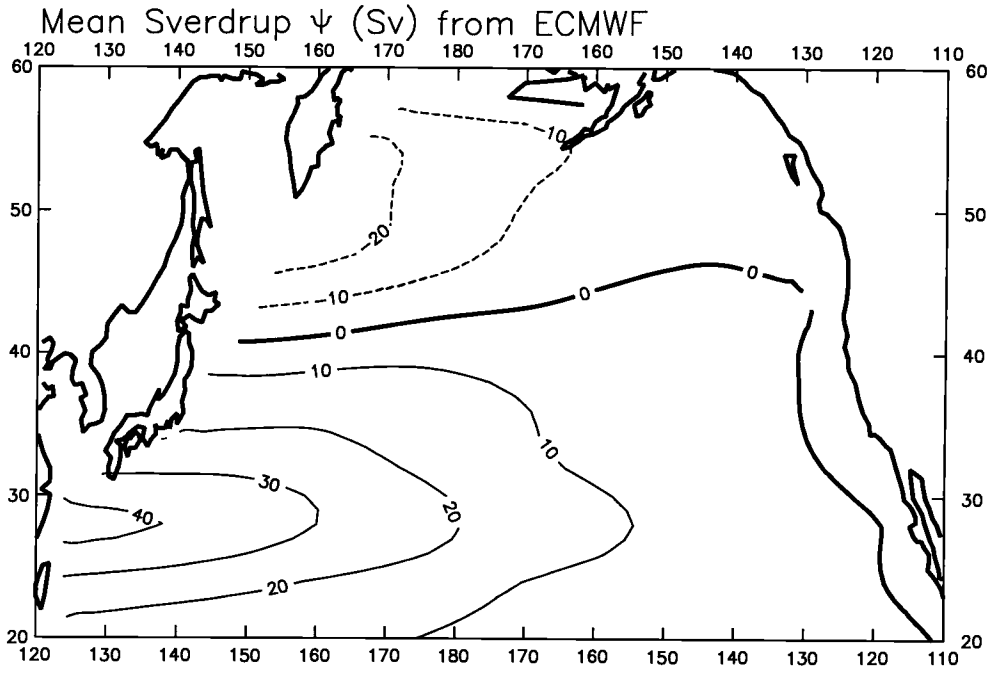

FIGURE 5.2. Mean Sverdrup volume transport streamfunction (Sv, 1 Sv$\equiv 10^6$ m^3 s^{-1}) in the North Pacific, calculated from the ECMWF wind stress curl field shown in Fig. 5.1.

Sverdrupian than the Atlantic. First, the Pacific is deeper and wider, with a large abyssal plain far away from the effects of the western boundary. Second, unlike the Atlantic where significant vertical shear can be found at all depths, in most of the Pacific there is a depth range (1000–3000 m) where the shear is very weak. This suggests that the wind-driven flow is isolated from the topography and reduces the uncertainty associated with selecting the reference level for the relative velocity calculation. Thirdly, the recirculation flow in the upper layers forced by the deep thermohaline component of the circulation is a larger fraction of the total flow in the Atlantic than in the Pacific.

The locations where the western boundary currents leave the coast are referred to as the separation points and the location where the two western boundary current extensions meet is referred to as the confluence point. This confluence point is located at a small distance eastward from the western boundary. If zonal variations of the wind stress were small and the ocean was purely linear, the confluence point and the boundary between the subtropical and subpolar gyres would lie along the latitude of the zero wind stress curl. However, zonal variations of the wind stress and nonlinear effects, given by the inertial terms in the vorticity equation, allow the boundary currents to overshoot the zero wind stress curl line, intensification of the zonal flow between the two gyres (the eastward jet), and secondary recirculations.

In the North Pacific, the interior southward flow of the subtropical gyre is compensated by the northward flow of the Kuroshio and the interior northward flow of the subpolar gyre is compensated by the southward flow of the Oyashio (Stommel and Yoshida 1972). The observed mean transport of the Kuroshio in the upper 1000 m, based on two years of hydrographic data referenced to current meter observations, is 56 Sv (1 Sv$\equiv 10^6$ m^3 s^{-1}) (Imawaki, personal communication, 1996) which compares well with the 40–60 Sv Sverdrup transports calculated from different

wind sources (e.g. Fig. 5.2, see also Table 1 of Hautala et al. 1994). The observed mean transport of the Oyashio is 22 Sv (as reported by Tomczak and Godfrey 1994) which can be compared to the $\sim$ 20 Sv from the Sverdrup calculation in Fig. 5.2.

The separation point of the Kuroshio and the eastward jet known as the Kuroshio Extension (Kawai 1972, see Fig. 5.3) are located along approximately 35°N, which is somewhat north of the zero mean curl in Fig. 5.1. The mean geostrophic transport from three deep hydrographic sections along 152°E across the Kuroshio Extension (29–41°N) is 57 Sv (Niiler et al. 1985). Because of flow instabilities of the eastward jet, the region of the Kuroshio Extension is dominated by eddies and meanders (see the insert in Fig. 5.3) and it stands out as a maximum in eddy variability in maps of the standard deviation of sea level observations from satellite altimetry (Zlotnicki 1991) (see also Fig. 5.9 below). The separation point of the southward flowing Oyashio current is located somewhat north of the Kuroshio Extension region at about 39–40°N (Sekine 1988).

The spin up of the mean wind-driven circulation described above is established by barotropic and baroclinic Rossby waves (e.g. Anderson and Killworth 1977). Topography causes interaction between the modes which results in a barotropic adjustment that occurs on two time scales. First, there is a fast adjustment (days) by barotropic Rossby waves to a topographic Sverdrup balance. Second, there is a slow adjustment (years) to a flat bottom Sverdrup balance in the wake of propagating baroclinic Rossby waves. For intermediate time scales, such as 1 year, the barotropic response dominates but the effects of the baroclinic adjustment and the role of topography are difficult to quantify.

In the North Atlantic, the validity of the flat-bottom, time-dependent Sverdrup balance on seasonal time scales has been questioned by several authors. Niiler and Richardson (1973) noted that the observed flow through the Florida Straits is

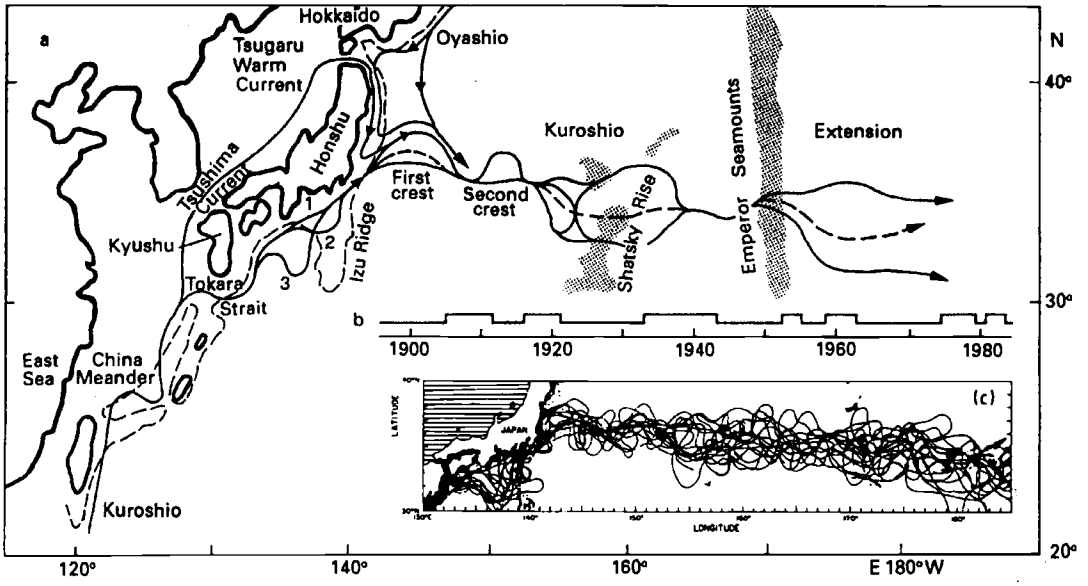

FIGURE 5.3. Schematic paths of the Kuroshio and Oyashio. The insert shows individual Kuroshio paths observed during summer 1976 to spring 1980. The dashed line is the 1000 m depth contour and illustrates the shelf break. (From Tomczak and Godfrey 1994).

out of phase with the variations predicted by flat-bottom Sverdrup theory. Anderson and Corry (1985a, b) pointed out the importance of bottom topography and showed that the time-varying flow through the Florida Straits is well represented by a 2-layer linear model driven by realistic wind forcing. They also showed that the variability is primarily barotropic since most of the model transport variations can be reproduced by a homogeneous version of the model.

In the North Pacific, the sea level difference across the Tokara Strait (Fig. 5.3) has been used to infer transport variations in the inflow region of the Kuroshio (Blaha and Reed 1982). The temporal variability of these sea level differences and of the geostrophic volume transport of the Kuroshio south of Japan (Taft 1972; Sekine and Kutsuwada 1994) show a large seasonal signal with a maximum in the summer and a minimum in the fall. This is about 6 months out of phase with the seasonal variations of the Sverdrup transport, which peak in winter at those latitudes. From barotropic simulations forced with Hellerman and Rosenstein (1983) seasonal anomalies from the annual mean winds, Greatbach and Goulding (1989, 1990) concluded that topography is crucial in determining the phase of the transport through the Tokara strait, analogous to the Anderson and Corry (1985 a,b) results for the North Atlantic. However, Greatbatch and Goulding estimates of the transport through the Tokara Strait are too small by a factor of at least two.

Sekine and Kutsuwada (1994) pointed out that the Greatbach and Goulding (1989, 1990) conclusion may change if the effects of mean flow and baroclinic adjustment are taken into account. Using a two-layer model of the North Pacific forced with seasonal observed winds compiled by Kutsuwada and Teramoto (1987), Sekine and Kutsuwada showed that simulations with flat or realistic bottom topography give Kuroshio transport variations nearly in phase with the Sverdrup flow. The main effect of including bottom topography in their model was to decrease the

amplitude of the transport variations by about 75%. Another finding was that the vertical difference of the horizontal velocities in each layer has the same phase as the observed geostrophic volume transport. That the model vertical shear agreed with the hydrographic observations but the model transport did not suggested that the reference velocity of the geostrophic velocities may not have been well estimated. To rationalize the phase difference between modeled and observed transport variations, Sekine and Kutsuwada proposed the existence of a barotropic flow during winter along the shelf break east of the Nansei Islands, located south of the Tokara Strait (see Fig. 5.3), which is blocked by topography and does not flow through the Tokara Strait.

Away from the western boundary of the North Pacific, the Greatbatch and Goulding (1989) topographic and flat-bottom simulations gave very similar transport variations, with the flat-bottom model (4000 m deep) giving amplitudes slightly larger. Greatbatch and Goulding considered this result to be related to the nearly-zonal structure of the f/H contours in the North Pacific (see Fig. 5.4, top panel). In the Sekine and Kutsuwada (1994) study the topographic and the flat-bottom simulations also gave similar transport variations in the interior. However, the amplitude in the Sekine and Kutsuwada topographic simulation was much smaller than in the flat-bottom (4500 m deep) case. In both the Greatbatch and Goulding and the Sekine and Kutsuwada studies the transport variations in the subtropical interior were in phase with the time-dependent Sverdrup theory, with larger transports in the winter and smaller subtropical transports in the fall.

In contrast to the flat-bottom, time-dependent Sverdrup balance discussed above, Koblinsky et al. (1989) tested a topographic Sverdrup balance (e.g. Pedlosky 1979) in the 10–100 day band, in an attempt to explain observed deep mesoscale current fluctuations in the North Pacific. This balance was found to apply only in

localized regions. However, the topographic Sverdrup balance has been questioned by Cummings (1991) who showed from numerical experiments that, even for periods longer than 100 days, the local balance is dominated by wavelike motions. In the Cummings (1991) experiments, the topographic Sverdrup balance emerges only after taking spatial averages of the vorticity equation. For 4° by 4° boxes, the balance holds for periods longer than 40 days and this cutoff period increases when smaller areas are considered. Recently, Fu and Davison (1995) used TOPEX/POSEIDON data to test the area-averaged vorticity equation globally in the 30–360 day band. Using 10° by 10° boxes, Fu and Davison conclude that a topographic Sverdrup balance is valid only in the northeast and southeast Pacific.

In an earlier South Pacific study, Mestas-Nuñez et al. (1992) integrated both the topographic and the flat-bottom Sverdrup equations. They showed that the flat-bottom Sverdrup balance was consistent with Seasat wind and sea level changes over a 3-month period but the topographic Sverdrup balance was not. Similar to the advantages of the North Pacific relative to the North Atlantic for testing Sverdrup balance of the mean flow as discussed previously, there are several reasons why the North Pacific is more suitable than the South Pacific for testing time-dependent Sverdrup dynamics. First, the North Pacific is deeper with more zonally oriented f/H contours than the South Pacific (Fig. 5.4). In particular, there is a large region of the South Pacific near the East Pacific Rise where the f/H contours are closed. There, the topographic Sverdrup balance becomes inappropriate and the flat-bottom approximation is difficult to justify. Second, the western boundary and associated return flows of the subtropical and subpolar North Pacific are better defined, allowing indirect tests of the interior Sverdrup flow. This is contrary to the South Pacific where, at high latitudes, two boundary currents are possible, one east of Australia and another east of New Zealand. Finally, in the North Pacific there

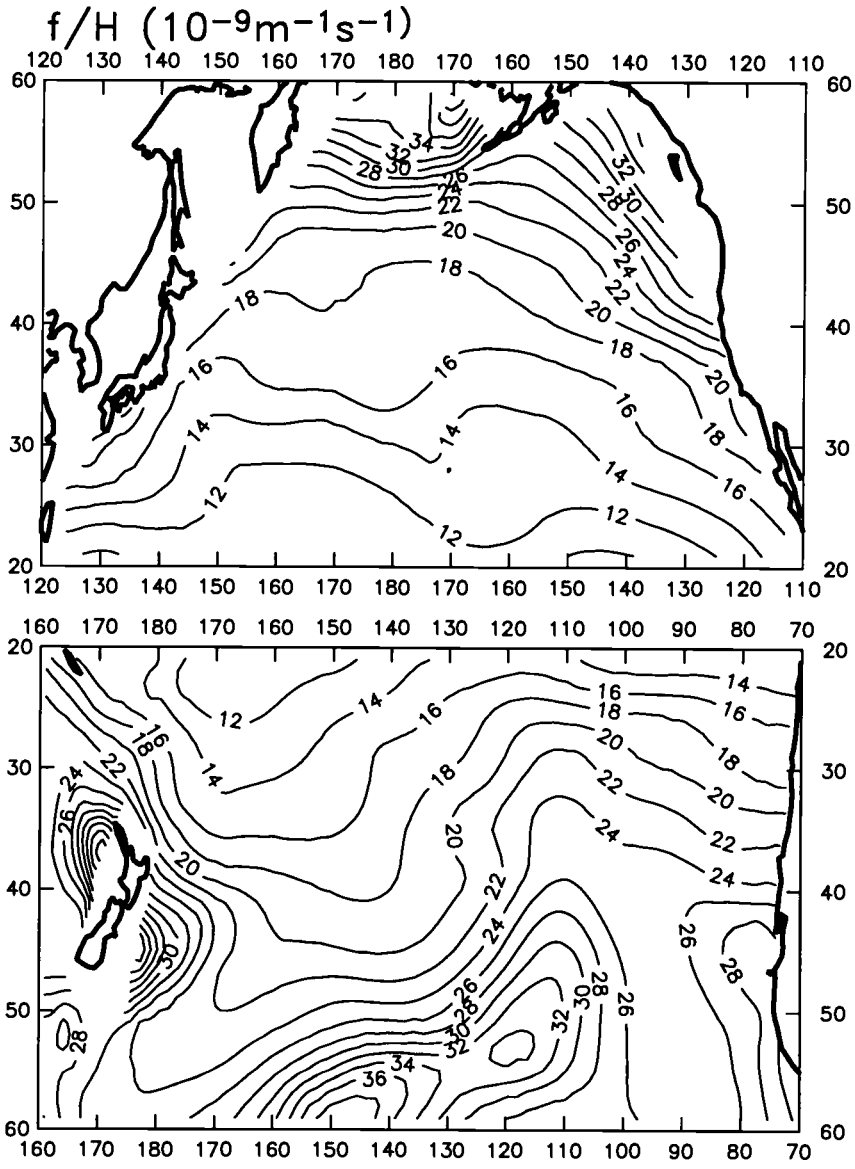

FIGURE 5.4. Contours of f/H in the North Pacific (top) and South Pacific (bottom). Contour interval is 2×10^{-9} m^{-1} s^{-1}. Only depth values greater than 1500 m were used and the topography was smoothed with a bell-shaped, low-pass filter analogous to 16° longitude by 5° latitude averages.

is a well defined subpolar gyre where Sverdrup dynamics are more likely to apply than at high latitudes in the South Pacific near the energetic, nearly-zonal flow of the Antarctic Circumpolar Current.

The goal of this study is to investigate flat-bottom, time-dependent Sverdrup dynamics in the western North Pacific on seasonal time scales and large spatial scales. The volume transport variability of the Oyashio/Kuroshio current system is estimated from simple Sverdrup theory and compared to the results of a state-of-the-art global ocean circulation model developed at Los Alamos National Laboratory by the Parallel Ocean Program (referred to hereafter as POP model; Dukowicz and Smith 1994). The sea level changes estimated from the Sverdrup theory are compared to high quality TOPEX/POSEIDON (hereafter TP) sea level observations. The comparison fields and procedures are described in section 5.3. The results of the Sverdrup theory are presented and described in section 5.4 and compared to the POP model in section 5.5. Sea level variability estimated from the Sverdrup theory is then compared to the variability observed by the TP altimeter in section 5.6. A summary of the results and a discussion are given in section 5.7

5.3. Comparison Fields

5.3.1. Sverdrup Streamfunction

The wind forcing used with the Sverdrup theory was based on 10-day vector-average wind stresses calculated from 10-m ECMWF winds using the drag coefficient of Large and Pond (1982). The record length used in this study is October 1992 to June 1994, which coincides with the first 20 months of the TP mission. The wind stress data were smoothed in time with a 1-d loess smoother (see Chelton et al. 1990b) with 60-day half span, analogous to 36 day averages, and in space with the

same bell-shaped low-pass filter used by Chelton et al. (1990a), which is analogous to 5° latitude by 16° longitude averages.

The 10-day wind stress maps were interpolated onto a 2° by 2° grid using cubic spline interpolation. The wind stress curl was computed using centered first differences in spherical coordinates. The Sverdrup streamfunction was derived by westward integration of the wind stress curl along lines of constant latitude from the coast of North America where the streamfunction was set to zero. The temporal mean Sverdrup streamfunction shown in Fig. 5.2 was removed from the time series at every grid point in order to investigate time-dependent Sverdrup transport variations.

5.3.2. POP Model Streamfunction

The POP model is a surface pressure formulation of the Bryan-Cox-Semtner global model that has been further improved by replacing the rigid-lid approximation with a free sea surface (Dukowicz and Smith 1994). The model equations are integrated on a Mercator grid with an average resolution of 1/5°. The actual resolution of the model is 31.25 km at the Equator and 6.5 km at ±78° latitude, with 1280 longitude points and 896 latitude points. Surface heat and salt fluxes were simulated by restoring to Levitus seasonal climatology with 1-month time scale in the upper level. Deep thermohaline forcing was allowed at high latitudes (70°N–78°N and 70°S–78°S) and in a 5° by 5° box around Gibraltar by restoring to Levitus climatology in the upper 2000 m with a 3-year time scale. Surface momentum fluxes were obtained from wind stress data calculated from ECMWF winds using the Large and Pond (1982) formulation. The wind stress record begins in 1985, with the period

1985–89 based on 1000 mb as in Trenberth et al. (1989) and after that on actual 10 m winds as suggested by Mestas-Nuñez et al. (1994).

The POP model was initialized using snapshots of temperature and salinity fields of the Semtner and Chervin 1/4° simulation interpolated to the 1/5°-average Mercator grid. From this initial state, the model was run for 8 years with wind forcing for the period January 1985–January 1993. The winds for 1985 were used twice to allow for some adjustment. From the final state of the first run (and because of an error in the implementation of the deep restoring boundary conditions around Gibraltar), a second run was performed with winds for the period January 1985–June of 1993. Finally, from the final state of the second run a third simulation was performed using 3-day (rather than monthly) averaged winds for the period January 1985–October 1994, with the winds for 1985 used twice. This is the model output analyzed in this study.

The barotropic streamfunction ψ_{bt} analyzed in this study was derived diagnostically from the POP model's barotropic (vertically averaged) velocity $\boldsymbol{u}_{bt}$ fields, which were archived every three days for the 20-month Topex period. The streamfunction was calculated by solving the Poisson equation

$$\nabla^2 \psi_{bt} = -\nabla \cdot (\boldsymbol{k} \times H\boldsymbol{u}_{bt})$$

with $\psi_{bt} = 0$ at the boundaries. Here, $\boldsymbol{k}$ is a unit vector in the vertical direction, H is the ocean depth and $H\boldsymbol{u}_{bt}$ is the vertically integrated velocity. A more detailed description of the streamfunction calculation is given in Appendix F of Dukowicz and Smith (1994).

For the purposes of this study, the high-resolution streamfunction field was interpolated onto a 1° by 1° by 10 day grid using trilinear interpolation. Smoothed estimates of the streamfunction at TP crossover points and repeat cycles were then

generated with the same low-pass filter used for the TP sea level (see section 5.3.3), analogous to 3.6° × 24 day averages. The average of the low-passed POP ψ_{bt} for the period October 1992–August 1994 is shown in Fig. 5.5. The mean circulation of the POP model compares well to the mean Sverdrup circulation presented in Fig. 5.2. This mean was removed from the time series of the low-passed POP barotropic streamfunction fields at every grid point for the analysis of time-dependent transport variability of interest here.

5.3.3. TP Sea Level

The launch of the TP satellite in August 1992 has provided the first high quality altimetric observations of sea level from which large-scale, low-frequency variability of ocean circulation can be investigated quantitatively. Unlike previous satellite altimeters (e.g. GEOSAT), TP observations have sufficient accuracy to study the small sea level changes (amplitudes of 1–10 cm) associated with the large-scale variability of the ocean surface currents. The satellite ground tracks of the TP altimeter have a repeat cycle of 9.9 days. Observations from the first 2.5 years of the mission are analyzed in this study. The data have been corrected for pressure loading effects and the other standard Geophysical Data Record corrections have been applied.

The sea level data used here have been low-pass filtered to remove temporal and spatial scales shorter than about 6° and 40 days, which are not adequately resolved by the irregular sampling pattern of the TP satellite (Greenslade and Chelton 1996). The smoothed estimates were generated globally at every crossover point and TP repeat cycle. The detailed procedure consisted of first applying a 1-d loess smoother in time with a half span of 40 days and then a 2-d loess smoother in space

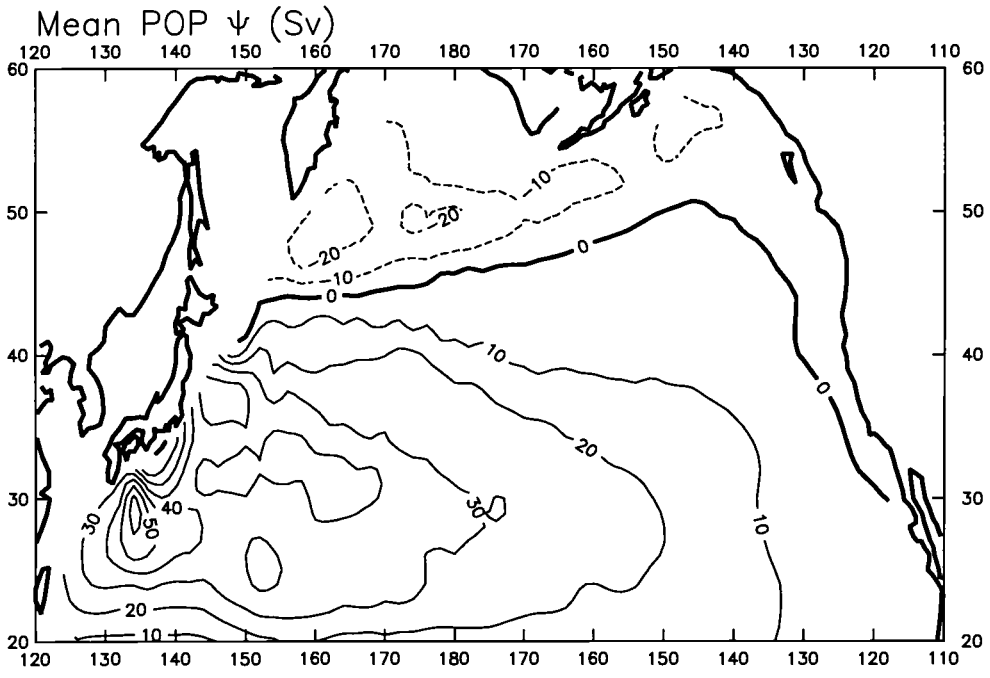

FIGURE 5.5. Mean POP model volume transport streamfunction (Sv) in the North Pacific for the period October 1992–August 1994, calculated from the smoothed fields generated as explained in the text.

with half spans of 6° in both latitude and longitude. This is analogous to 3.6°× 24 day averages. Estimates were constructed at every repeat cycle. The first two and last two cycles were not analyzed in this study to avoid edge problems in the smoothed time series. Finally, we removed any residual temporal mean from the time series.

5.4. Sverdrup Theory Transport Variations

A map of the standard deviation of the Sverdrup streamfunction in the North Pacific is shown Fig. 5.6. The temporal variability of the Sverdrup circulation is largest at high latitudes with localized maxima occurring at three locations in the western North Pacific. The primary maximum (∼ 24–28 Sv) near 45°N is about 5° south of the mean location of the center of the subpolar gyre (see Fig. 5.2). There is a secondary maximum (∼ 20 Sv) just north of the Kuroshio Extension region at 38°N. The third maximum (∼ 16–20 Sv) is near 28°N, which coincides with the mean location of the center of the subtropical gyre (see Fig. 5.2).

The Sverdrup streamfunction fields are used to estimate volume transport variations of the meridional flow near the North Pacific western boundary and in the Kuroshio Extension. From the linear barotropic (vertically averaged) continuity equation with the rigid-lid approximation, a volume transport streamfunction ψ can be defined as

$$H\boldsymbol{u}_{bt} = \boldsymbol{k} \times \nabla\psi. \tag{1}$$

The total volume transport through a surface extending from the sea surface to the ocean bottom between two arbitrary points is just the difference between the streamfunction values at the two points. For example, the total meridional transport

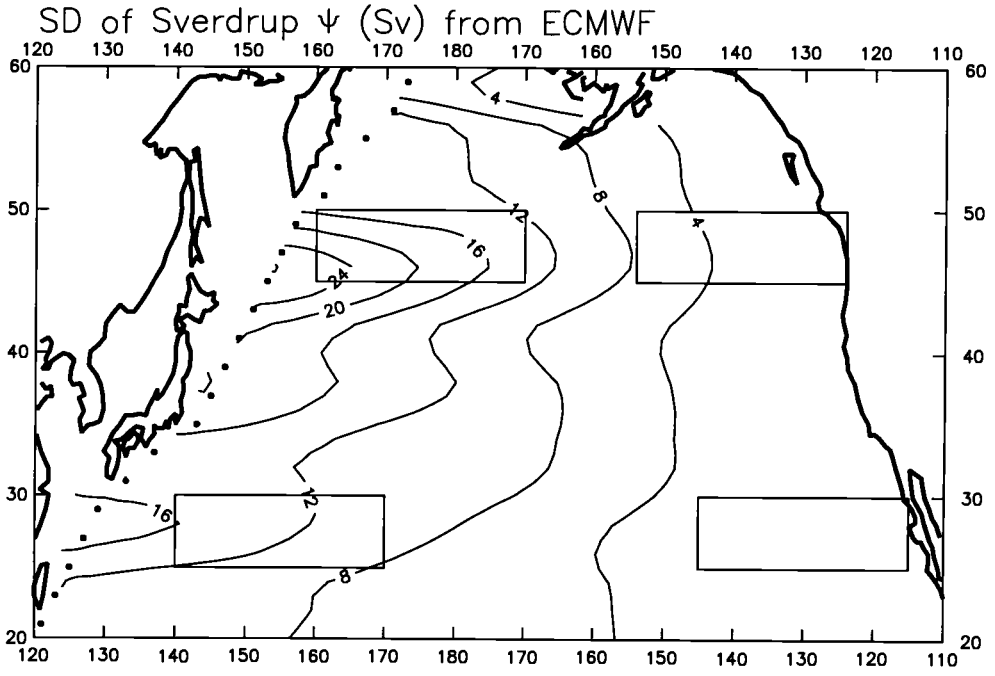

FIGURE 5.6. Standard deviation of the Sverdrup circulation for the North Pacific in Sv computed from ECMWF winds for the period October 1992–June 1994. Also shown are the box locations for estimating the transport variations of the western boundary currents and the grid points for the EOF analysis described in the text.

between points x_1 and x_2 is

$$\int_{x_1}^{x_2} H v_{bt} dx = \int_{x_1}^{x_2} \frac{\partial \psi}{\partial x} dx = \psi(x_2) - \psi(x_1).$$

The transport variations near the western boundary are estimated indirectly from basin-wide streamfunction differences based on continuity of volume. The meridional transport of the western boundary currents must be equal in magnitude and opposite in sign to the total meridional transport across the interior basin.

Examination of Fig. 5.6 suggests that the variability of the Sverdrup circulation has large spatial scales ($\sim 10^\circ$ in latitude and basin scale in longitude). The meridional scales of Sverdrup transport are defined by the scales of the wind stress curl. The zonal scales of the streamfunction variability are much larger than the curl. This is a consequence of the zonal-integral operation performed on the wind stress curl to calculate the streamfunction, which is an effective low-pass filter. In contrast, the large-scale variability of the POP streamfunction and TP sea level, which will be used to evaluate the Sverdrup theory in sections 5.5 and 5.6, has shorter spatial scales (see Fig. 5.10 and Fig. 5.13). These shorter spatial scales are related to processes not described by the simple Sverdrup theory (e.g. topography and transients such as planetary waves and mesoscale eddies and meanders of the mean flow). Thus, some additional spatial smoothing of the POP streamfunction and TP sea level is required. For simplicity, we use box averages and in order to be consistent we smooth the Sverdrup streamfunction in the same fashion. The streamfunction was therefore averaged in the 5° latitude by 30° longitude boxes shown in Fig. 5.6.

An important question is the sensitivity of the estimates of the western boundary current (WBC) transport variability to our particular choice of box locations. This was investigated from an Empirical Orthogonal Function (EOF) analysis

of the Sverdrup streamfunction along the western boundary at the grid points shown in Fig. 5.6. The first and second EOF of the WBC transport variability are shown in Fig. 5.7 and they account for 55% and 29% of the total WBC variance, respectively. The dominant mode is a seasonal cycle with maximum in winter and minimum in summer/fall. The amplitude of this mode is largest at approximately the latitudes of the primary ($\sim$ 45°N) and third ($\sim$ 28°N) maxima in Fig. 5.6 and near our WBC boxes. The latitudes of our boxes are thus representative of the latitudes of maximum WBC variability.

The time series of Sverdrup transport variations for the southward-flowing Oyashio is shown by the solid line in the top panel of Fig. 5.8. As expected from the EOF analysis, the transport variations of the Oyashio show a dominant seasonal cycle with an amplitude of about 20 Sv. For comparison, the time series of Sverdrup transport variations for the northward-flowing Kuroshio is also shown in the top panel of Fig. 5.8 (dashed line). The transport variations of the Kuroshio also show a dominant seasonal cycle with amplitude similar to, although slightly smaller than, the transport variations of the Oyashio. As inferred above from the structure of the dominant EOF of WBC transport, the seasonal Sverdrup transport variations of the two currents are in phase: both currents are strongest in winter and weakest in summer/fall.

Based on the coherent transport variations of the Kuroshio and Oyashio predicted by the Sverdrup theory, we expect large Sverdrup transport variations in the Kuroshio Extension. Using a simple conceptual model based on continuity of volume, the transport variations of the Kuroshio Extension can be inferred from the sum of the transport variations in the Oyashio and Kuroshio. This index is shown by the solid line in the bottom panel of Fig. 5.8.

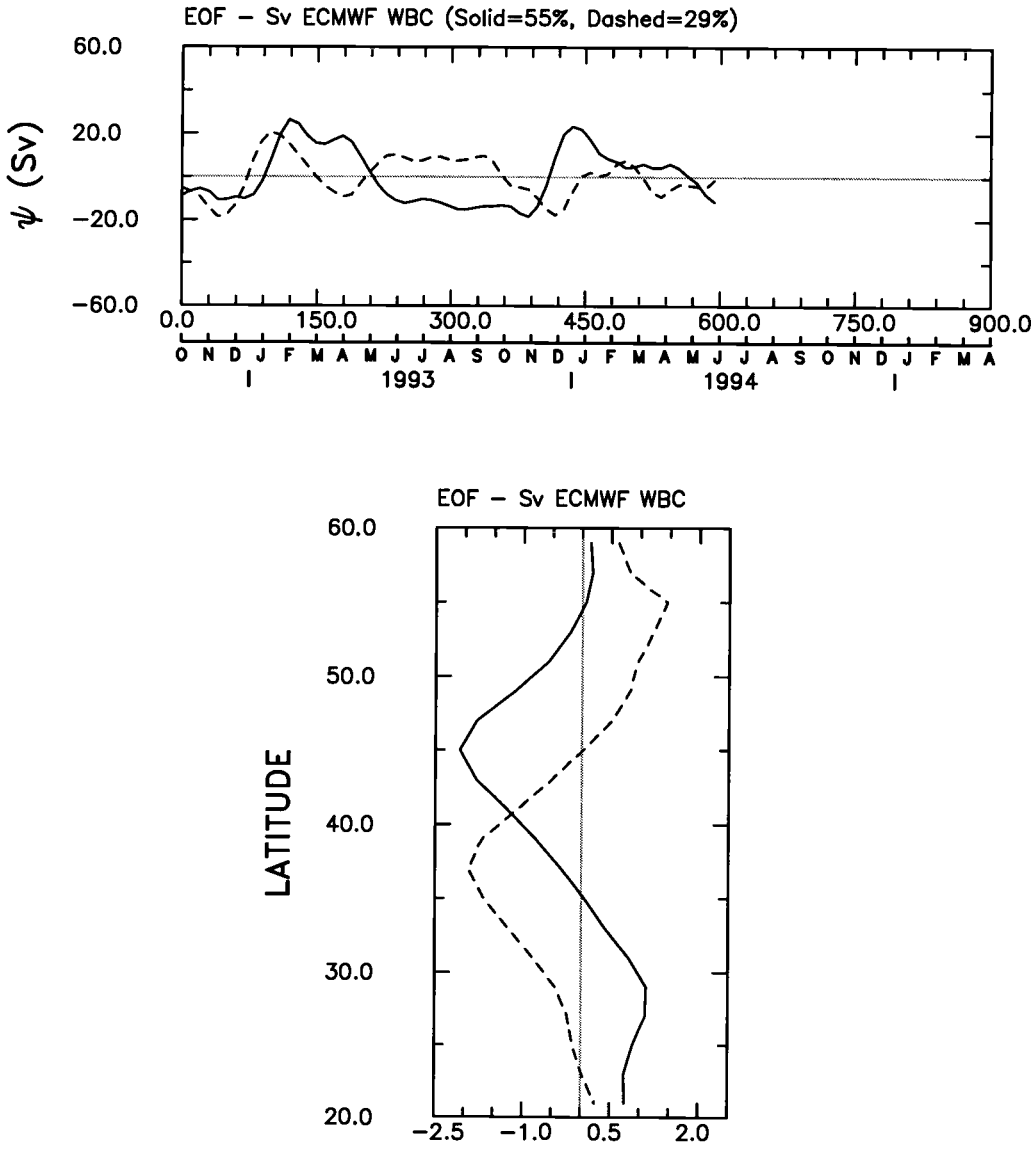

FIGURE 5.7. Amplitude time series (top) and EOFs (bottom) of Sverdrup stream-function variations at the grid points shown in Fig. 5.6. The first mode is indicated with a solid line and the second mode with dashed line.

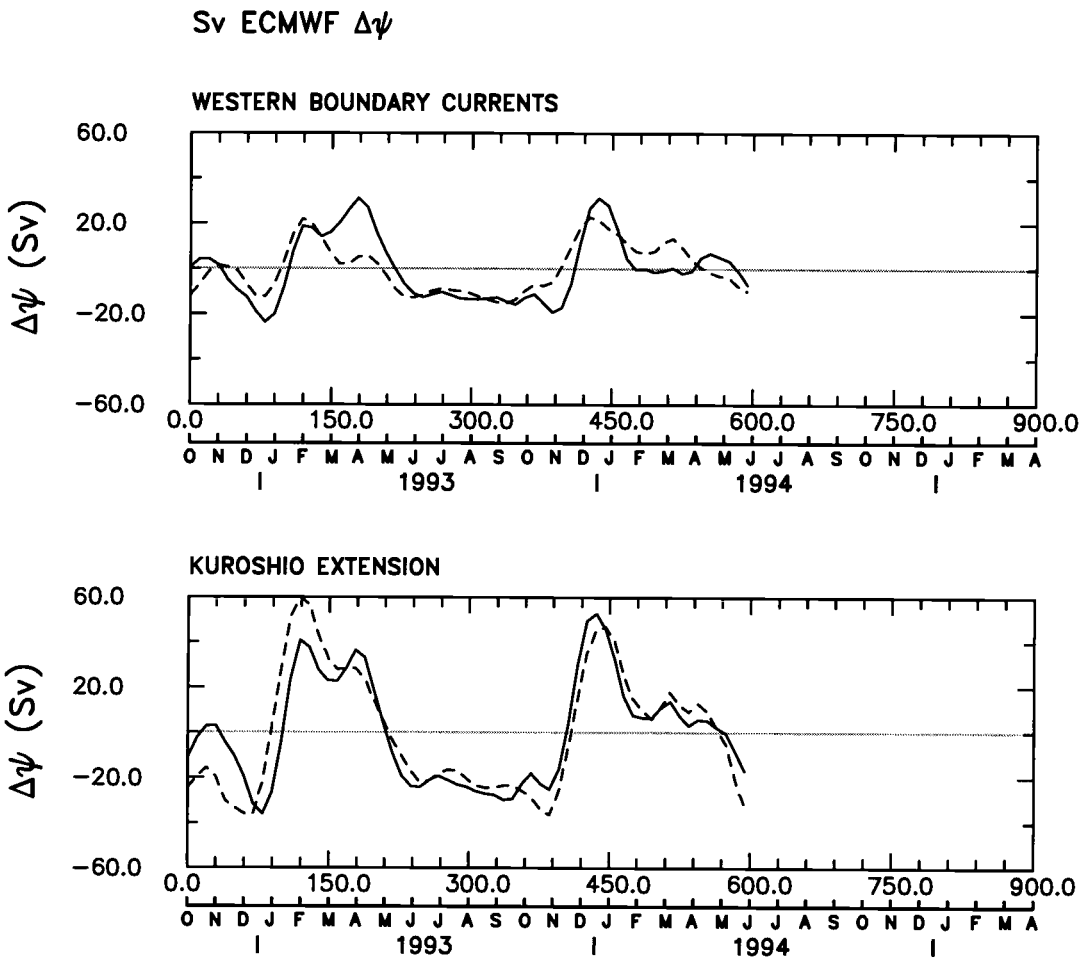

FIGURE 5.8. Transport variations (Sv) of the southward flow of the Oyashio (top, solid), northward flow of the Kuroshio (top, dashed) and the sum of the Oyashio plus Kuroshio variations (bottom, solid) estimated from the Sverdrup theory. The transport variations of the eastward flow of the Kuroshio Extension estimated from the Sverdrup theory is also shown (bottom, dashed).

These expected variations of the Kuroshio Extension transport can be tested from a direct estimate of the Kuroshio Extension transport variations calculated by averaging the streamfunction over 5° latitude by 25° longitude boxes across the Kuroshio Extension and then taking the difference (south minus north). The mean location of the Kuroshio Extension was inferred from the location of the high mesoscale variability in a map of sea level standard deviation from the TP altimeter shown in Fig. 5.9. The locations of the boxes used to obtain the direct estimates of Kuroshio Extension transport variations are also shown in Fig. 5.9. The resulting time series of Kuroshio Extension transport variability is shown with the dashed line in Fig. 5.8.

Both estimates of the Kuroshio Extension transport variations in the bottom panel of Fig. 5.8 agree well. The correlation coefficient is 0.89. The Sverdrup transports of both boundary currents add constructively to yield an increase of the Kuroshio Extension eastward transport of about 40 Sv in the winter and a decrease of the transport, of slightly smaller amplitude, in the summer/fall.

To check the sensitivity of our results to the winds, we have repeated this analysis with winds from the ERS-1 scatterometer. The results of the Sverdrup theory with ERS-1 and ECMWF winds are very similar because both wind products compare well in the North Pacific on the space and time scales of interest here.

5.5. POP Model Transport Variations

The time-dependent Sverdrup balance considered in the previous section is the simplest possible theory of basin-scale circulation. The extent to which it is valid on the seasonal to interannual time scales of interest here depends on many factors.

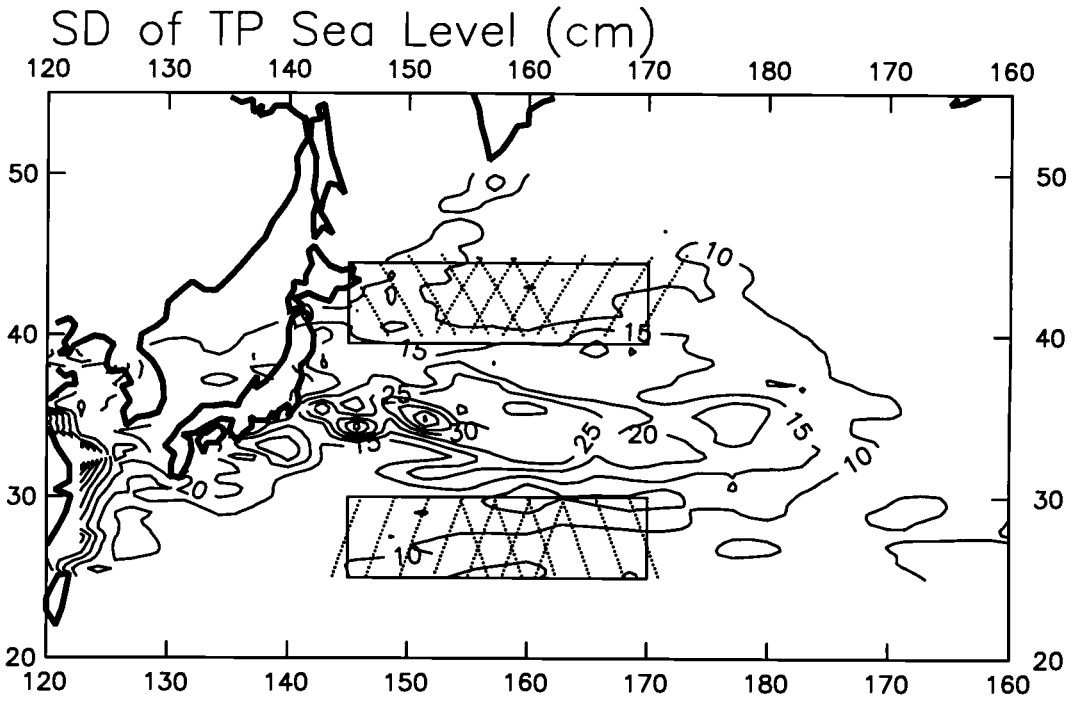

FIGURE 5.9. Location of boxes for estimating Kuroshio Extension transport variations superimposed on a map of sea level standard deviation (cm) from TP observations. Also shown are the location of some selected TP tracks used in section 5.6.

First, at middle and higher latitudes, the variability should be barotropic to zeroth order since the transient adjustment time for baroclinic Rossby waves is much longer than the time scales of the transport variations in Fig.5.8 (see e.g. Fig. 1 of Chelton and Schlax 1996). For the extreme case of a homogeneous ocean with very rapid barotropic adjustment, the quasi-steady balance is the topographic Sverdrup balance. In this balance, the circulation is calculated integrating the wind stress curl along lines of constant f/H — the f/H contours are mostly zonal in the North Pacific (see Fig.5.4) but with significant deviations in some regions — instead of constant f (latitude). However, attempts to simulate (Cummings 1991) or to validate (Fu and Davison 1995) this balance in the North Pacific have been mostly unsuccessful.

Second, at the other extreme of a stratified ocean with very rapid barotropic and relatively slow ($\gtrsim$ 5 years for the latitude range of interest here) baroclinic adjustment, the quasi-steady balance that should apply is the flat-bottom Sverdrup balance. The degree to which the flat-bottom Sverdrup theory can be applied to the North Pacific on seasonal time scales depends on the degree of baroclinic adjustment. Furthermore, the 5-year baroclinic adjustment time represents an upper limit because it is based on the assumption that the source for baroclinic Rossby waves is the eastern boundary. For all other possible sources of baroclinic waves (e.g. related to changes in the Ekman pumping in the ocean interior either at the surface from changes in the curl or at the bottom from topographic effects) the transit time would be smaller. The implications are that the baroclinic compensation of topographic effects on seasonal time scales may be more important than is generally believed.

Thirdly, both the topographic and the flat-bottom quasi-steady Sverdrup balances discussed above neglect transient motions (i.e. assume infinite Rossby

wave speeds) and higher order effects such as advection and diffusion of vorticity, buoyancy forcing, and bottom drag.

The importance of these issues can be investigated by comparing the flat-bottom Sverdrup transport variations with the transport variations simulated by the primitive equation POP model. As noted in section 5.3.2, the POP model is driven by the same ECMWF wind stress fields as the Sverdrup model, but includes additional forcing (e.g. buoyancy and inflow) and other dynamical processes beyond the simple time-dependent Sverdrup dynamics.

The standard deviation of the smoothed POP barotropic streamfunction is shown in Fig. 5.10. The variability of the POP circulation has some features qualitatively similar to the variability of the Sverdrup circulation in Fig. 5.6. The POP variability is largest in the subpolar region. There are also three local maxima in the western Pacific at about 30°N, 40°N and 45°N, which are close to the latitudes of the three maxima in the Sverdrup variability (Fig. 5.6). There are also some significant differences between POP and Sverdrup variability. POP has more spatial structure with a local maximum in the Bering Sea near 55°N that is not present in the Sverdrup theory. In addition, the effects of topography are evident in Fig. 5.10 from the region of low variability along the Emperor Seamount Chain near 170°E between 40° and 50 °N (see Fig. 5.3) and along the Izu Ridge near 140°E.

The POP transport variations for the Oyashio, Kuroshio and Kuroshio Extension are estimated by averaging the barotropic streamfunction over the same boxes used with the Sverdrup theory (see Figs. 5.6 and 5.8). The transport variations for the Oyashio, Kuroshio and the sum of Oyashio plus Kuroshio are shown in Fig. 5.11. It is worth noting that the streamfunction variations in the eastern WBC boxes are very small. Thus direct estimates of WBC transport variations calculated from the difference between the average streamfunction at the western boxes and

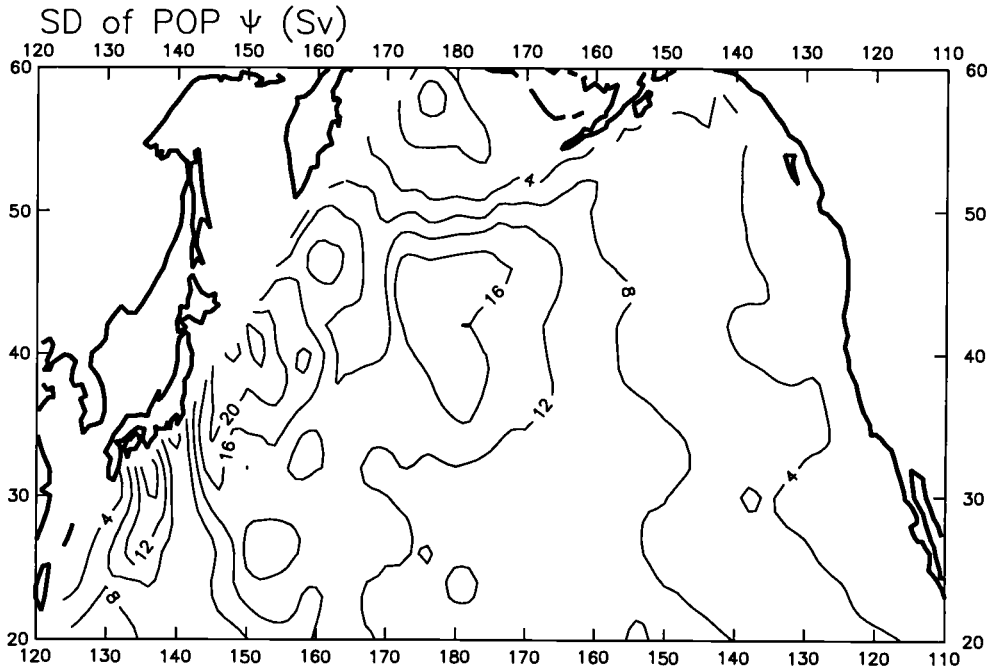

FIGURE 5.10. Standard deviation of the POP model barotropic streamfunction for the North Pacific in Sv for the period October 1992-August 1994.

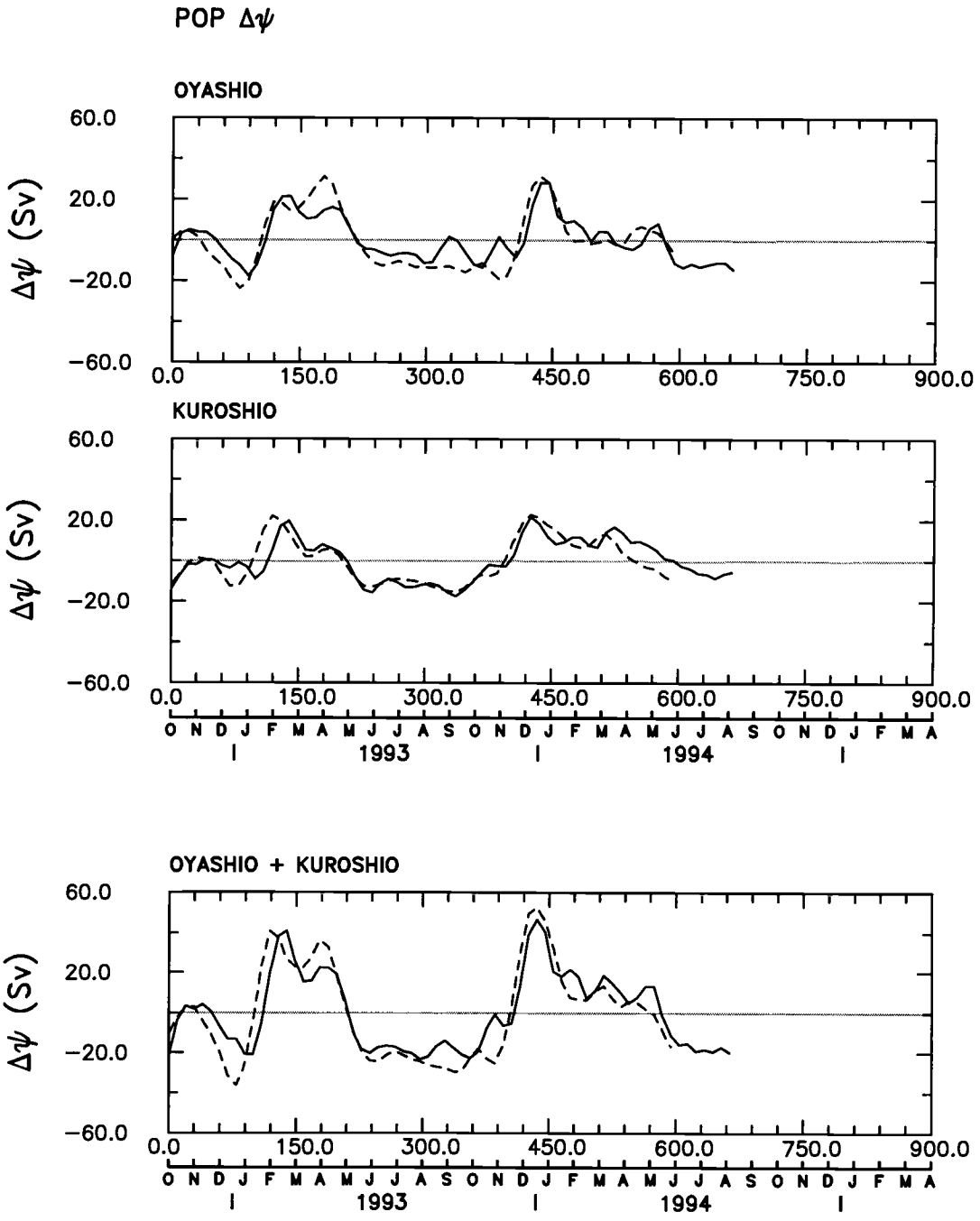

FIGURE 5.11. Transport variation (Sv) of the Oyashio (upper), Kuroshio (middle) and Oyashio plus Kuroshio (lower) estimated from the smoothed POP model streamfunction generated as described in the text. The results of the Sverdrup theory are also shown for comparison (dashed lines).

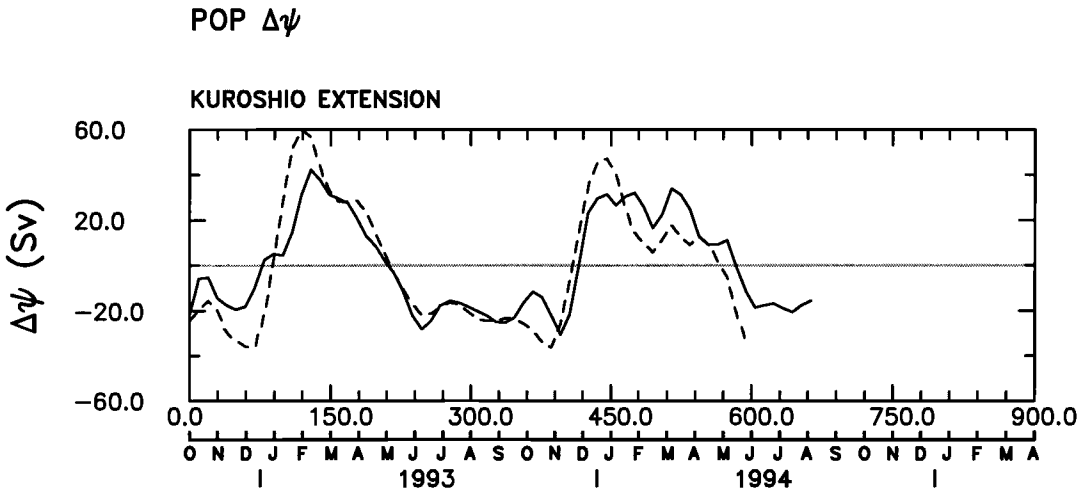

FIGURE 5.12. Transport variation for the Kuroshio Extension in Sv estimated from the POP barotropic streamfunction. The result of the Sverdrup theory is also shown for comparison (dashed line).

the value of the streamfunction at the western boundary (which is zero by definition) are therefore very similar to the time series shown in Fig. 5.11. The transport variations in the Kuroshio Extension are shown in Fig. 5.12. For comparison, the corresponding Sverdrup results presented in Fig. 5.8 are shown in both figures by dashed lines.

The agreement between the transport variations estimated from the theory and model is striking. The correlation coefficients between the POP and Sverdrup

transport time series range from 0.83 to 0.93 (Table 5.1). The significance level of the correlations was calculated based on an estimate of the effective sample size N^* instead of the total sample size N. From the time series of the Sverdrup and POP transport variations for the Oyashio shown in the upper panel in Fig.5.8 and using the long-lag correlation technique (Chelton 1983) with lags ranging from −400 to −300 days and 300 to 400 days N^* was estimated to be about 13. Using $N^* = 13$ the 99% significance level on the sample correlation is approximately 0.58. The sample correlations are thus statistically significant with much greater than 99% confidence. Note that N and N^* are related by the equation $N\Delta t = N^*\Delta t^*$ where Δt is the sample time interval and Δt^* is the effective sample time interval of the data (Preisendorfer 1988). Since $N = 61$ and $\Delta t = 10$ days, Δt^* is approximately 50 days.

TABLE 5.1. Correlation coefficient between Sverdrup and POP transport variations and the ratio of the standard deviation (SD) of the Sverdrup variations to the POP variations.

	Correlation	SD Ratio
Oyashio	0.86	1.37
Kuroshio	0.83	1.04
Oyashio + Kuroshio	0.93	1.23
Kuroshio Extension	0.88	1.28

The amplitudes of the Kuroshio transport variations predicted by the flat-bottom, time-dependent Sverdrup theory and the POP model are about the same (Table 5.1). The Sverdrup transport variations for the Oyashio and Kuroshio Extension are larger than the POP model by about 30%. This discrepancy may be related to the neglect of topographic effects in the Sverdrup theory. As noted in the introduction, one of the main effects of topography in a baroclinic ocean is to reduce

the amplitude of the seasonal response (Sekine and Kutsuwada, 1994). We note, however, that the decrease in amplitude of the seasonal transport variations of the Kuroshio by topography in Sekine and Kutsuwada's model was much larger (about 75%) than the differences between the Sverdrup and POP transport variations. This may be related to the simplified representation of stratification (2 layers) in their model. The large difference between the amplitudes of Sverdrup and POP transport variations in the Oyashio may be related to the faster baroclinic adjustment of the subtropical oceans relative to the subpolar oceans.

In summary, the comparison of Sverdrup and POP models indicate that time-dependent Sverdrup dynamics may account for a large fraction of the temporal characteristics of the POP simulation of large-scale, wind-forced transport variations in the western North Pacific on seasonal and longer time scales. However, this analysis suggests that the Sverdrup theory overestimates the amplitudes of transport variations in the Subpolar gyre. It should be emphasized that these conclusions apply to area-average, zonal integrals of the Sverdrup balance (i.e. streamfunction) rather than to the area-averaged local topographic Sverdrup balance (i.e. vorticity) tested by Cummings (1991) and Fu and Davison (1995).

5.6. TP Sea Level Variations

The agreement between the simple time-dependent Sverdrup balance and the complex POP model described in the previous section is very good. We emphasize again that our conclusions pertain to very large space scales (5° of latitude by 25°of longitude) and long time scales (longer than 40 days). These scales are well resolved by the TP altimeter (Greenslade and Chelton, 1996). The variability of

the circulation predicted by the models is compared with TP sea level observations in this section.

For a linear, barotropic (vertically averaged) flow in geostrophic balance, the momentum equation is

$$f\boldsymbol{k} \times \boldsymbol{u_b} = -g\nabla\eta_b. \tag{2}$$

Multiplying by H and using (1), this equation becomes

$$f\nabla\psi = gH\nabla n_b$$

For constant H and meridional scales of motion much shorter than $L_y = R\tan\theta$, where R is the radius of the earth and θ is latitude, we obtain $\nabla(f\psi_{bt}) = \nabla(gH\eta_b)$. At 40°N, this length scale is $L_y \sim 5000$ km, which is larger than the ~ 1000 km meridional scales of interest here. An effective barotropic sea level can thus be obtained from the barotropic streamfunction by

$$\eta_{bt} = \frac{f}{gH}\psi_{bt}, \tag{3}$$

where f is the Coriolis parameter, g is gravity and H is mean water depth. It is difficult to determine the precise value of H to use in the flat-bottom Sverdrup theory because the effective depth of the wind-forced barotropic motions is not known. We use a value of $H = 4$ km here. If a value of $H = 5$ is used, the sea level amplitudes computed from the streamfunction fields decrease by 20%.

A map of the standard deviation of the filtered TP sea level data is shown in Fig. 5.13. The most noticeable structure is the broad band of high variability associated with the Kuroshio Extension. By comparison with Fig. 5.9, it is evident that the variability in the raw data is diminished by the spatial smoothing and low-pass temporal filtering applied to the TP data as summarized in section 5.3. The maximum variability in the region of the Kuroshio extension has been reduced from

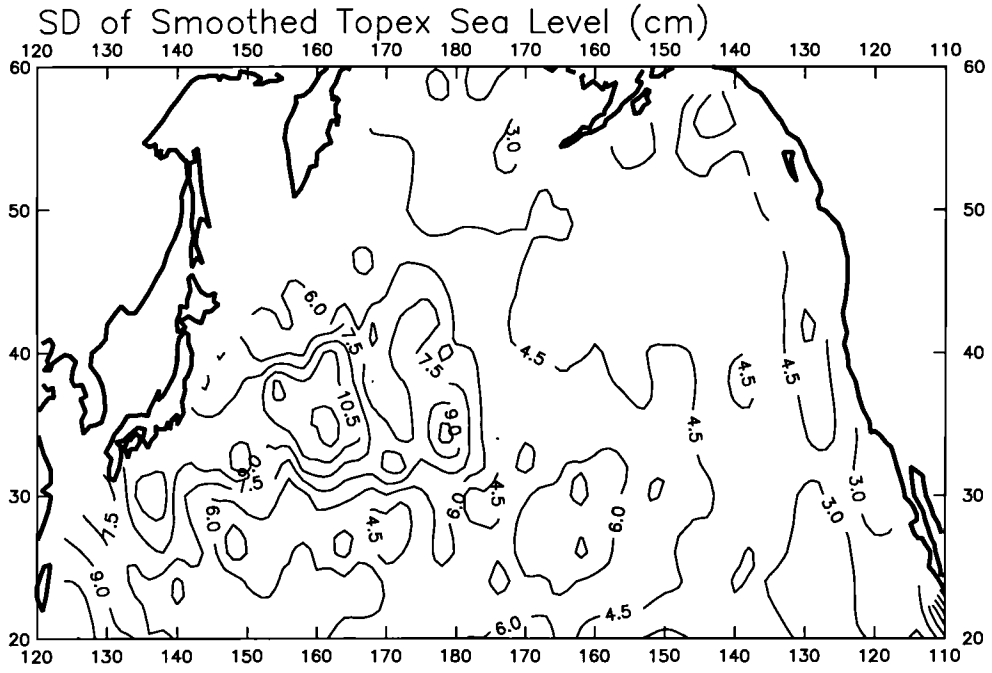

FIGURE 5.13. Contours of the standard deviation (cm) of sea level in the smoothed TP sea level fields generated as explained in the text.

30 cm to 10 cm. The background variability over the rest of the North Pacific is 3–5 cm.

On seasonal time scales there are two dominant signals in the smoothed TP sea level fields filtered as described in 5.3.3. On short spatial scales of $\lesssim$ 1000 km, there is the signature of quasi-annual first baroclinic Rossby waves (Chelton and Schlax 1996). These waves have wavelengths that decrease with increasing latitude. At a given location, it is believed that these waves are generally uncorrelated with the local wind stress curl. As a consequence, Rossby waves are effectively a source of noise in studies of the wind-forced sea level response from point correlations.

On very long spatial scales, there are seasonal steric-height changes due to the expansion and contraction of the water column associated with heating and cooling above the seasonal thermocline (e.g., Nerem et al. 1994; Stammer 1996). The steric height change is a baroclinic effect affecting only the near-surface flow and thus its contribution to the volume transport is small (Gill and Niiler 1973). However, its effects on sea level can be large. The steric signal must therefore be removed before sea level can be compared to the purely wind-forced sea level response estimated from the Sverdrup theory.

The contribution of baroclinic Rossby waves to TP sea level variability has been ameliorated by the box averaging over 5° of latitude and 25° of longitude as described previously. The maximum wavelength possible for quasi-annual Rossby waves at the latitudes of interest in this study is about 1600 km at 20°N. The Rossby wave signal is therefore diminished by our 25° averages. Our analysis was restricted to latitudes higher than 20°N because the Rossby waves at lower latitudes have very long zonal wavelengths and are therefore difficult to separate from the large-scale wind-driven variability of interest in this study.

The effect of steric-height sea level changes has been eliminated by removing the Stammer (1996) steric height estimates based on ECMWF heat fluxes. Stammer calculated the changes in the steric component of sea level in terms of the surface heat flux from

$$\frac{\partial \eta_s}{\partial t} = \frac{\alpha Q'}{\rho c_p}$$

where Q' is the anomaly relative to a time mean sea surface heat flux, α is the thermal expansion coefficient, ρ is the density of sea water, and c_p is the specific heat of sea water. The value of c_p was estimated as a function of the temperature of the mixed layer.

After removing the steric height contribution, the smoothed TP Sverdrup sea level fields are used to estimate sea level differences across the currents following the same procedures used to calculate streamfunction differences in sections 5.4 and 5.5. From (3), the sea level differences can be interpreted as indices of transport variability based on the assumptions of geostrophy and barotropic flow. Geostrophy allows sea level differences to be related to surface velocity. This is simply related to transport variations in the water column if the flow is also barotropic.

To determine the effects of filtering of the TP data, the sea level differences across the Kuroshio Extension calculated from the smoothed fields were compared with those calculated from the raw data along the ground tracks shown in Fig. 5.9. There are at least two possible ways to estimate the sea level differences across the Kuroshio Extension from the altimeter track data. One method is based on calculating the sea level difference along each track from the average sea level along each track segment. The other method is based on estimating the average sea level in the northern and southern regions and using them to calculate the difference. Both methods give identical results if there are no data dropouts since the averaging operation is linear. The two methods were, indeed, found to be almost identical,

indicating that data dropouts are not a significant problem. The time series of the track sea level differences calculated using the first method is shown with dashed lines in Fig. 5.14. For comparison, the sea level differences calculated from the loess smoothed fields are shown with a solid line in Fig. 5.14. It is evident that the sea level differences from the smoothed and track data agree very well. The correlation coefficient is 0.96. The track data in Fig. 5.9 is more energetic on short $\sim$ 50 day time scales because the short-period variability of the data is diminished by the loess smoothing. Both time series show evidence of intraseasonal variability (about 30–100 days) which is believed to be associated with barotropic motions (Fu and Smith 1995).

The Sverdrup and TP sea level differences for the Oyashio, Kuroshio and Oyashio plus Kuroshio are shown in Fig. 5.15 and the sea level differences across the Kuroshio Extension are shown in Fig. 5.16. Except in the Oyashio the TP and Sverdrup sea level differences compare well. The correlation coefficient between the TP and Sverdrup sea level differences and the ratio of the standard deviation of the Sverdrup to the TP differences are shown in Table 5.2. Assuming that $N^* = 13$ as in the comparisons in Table 5.1, the 99% significance level of the correlations is 0.58. All the correlations in Table 5.2 except for the Oyashio are thus significant with greater than 99% confidence. The the correlation in the Oyashio is significant only at $\sim$ 95% level (=0.48). The correlation of the Oyashio plus Kuroshio is significant at the 99% level because of the Oyashio contribution which is better correlated than the Oyashio. The amplitudes of the Sverdrup sea level differences are about 1.6 to 2 times too large except for the Kuroshio where the Sverdrup transport is about 20% too small.

The sea level variability estimated by the Sverdrup theory is compared pointwise with the TP sea level variability over the entire North Pacific in Fig. 5.17. The

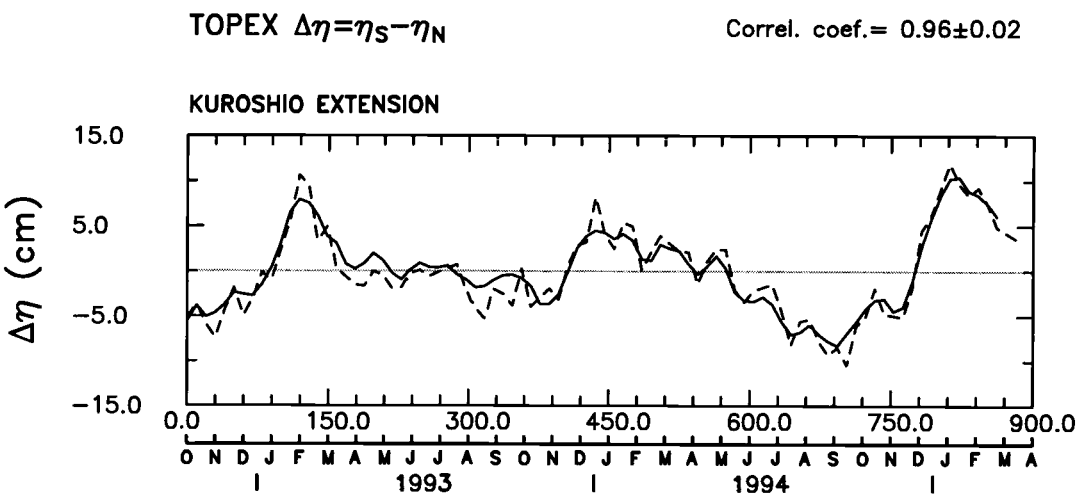

FIGURE 5.14. Time series of TP sea level differences (cm) across the Kuroshio Extension from the track data (dashed) and from the smoothed data generated as described in the text (thin).

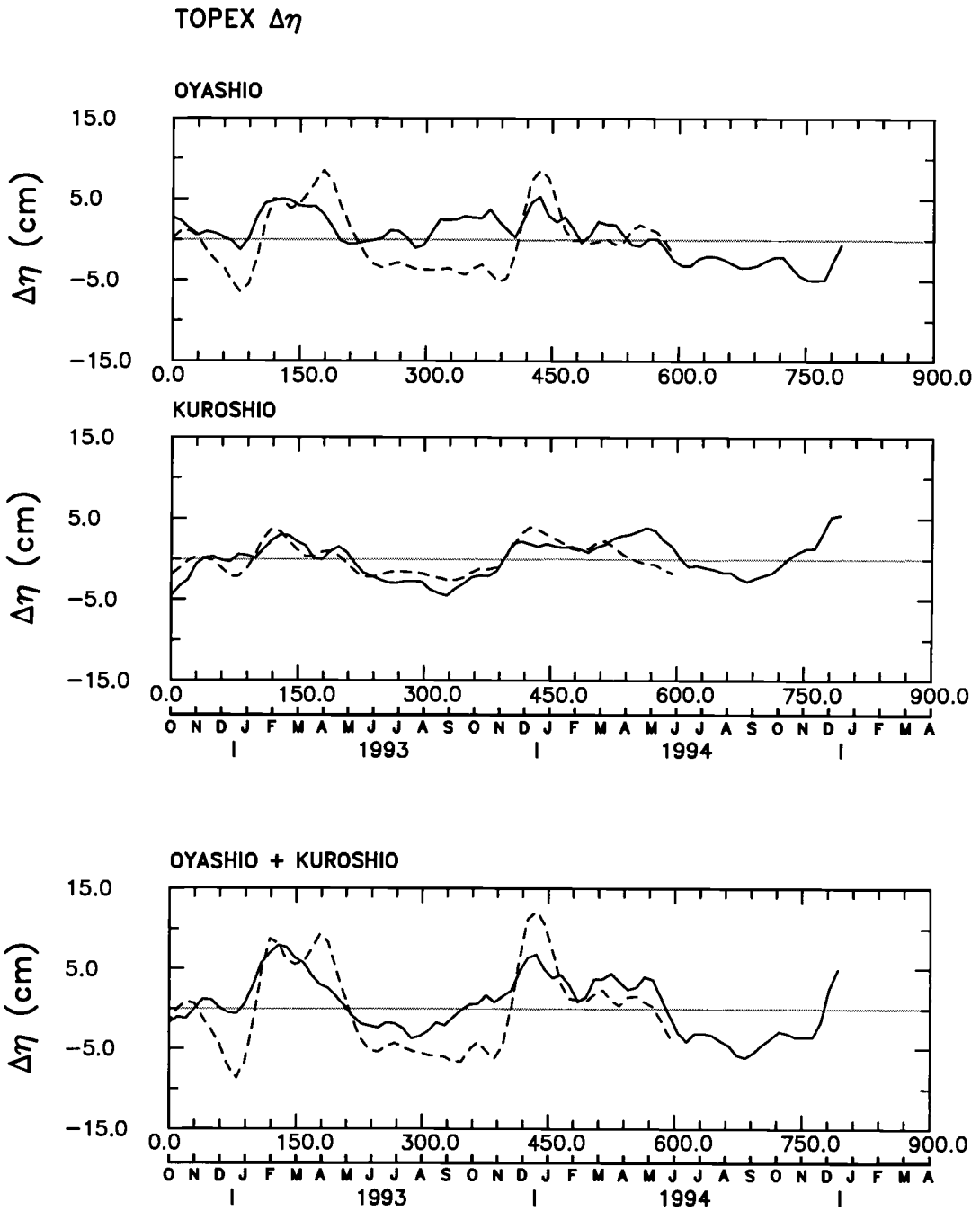

FIGURE 5.15. Variation of sea level differences for the Oyashio (upper), Kuroshio (middle) and Oyashio plus Kuroshio (lower) in cm estimated from the smoothed TP sea level. The results of the Sverdrup theory are also shown for comparison (dashed lines).

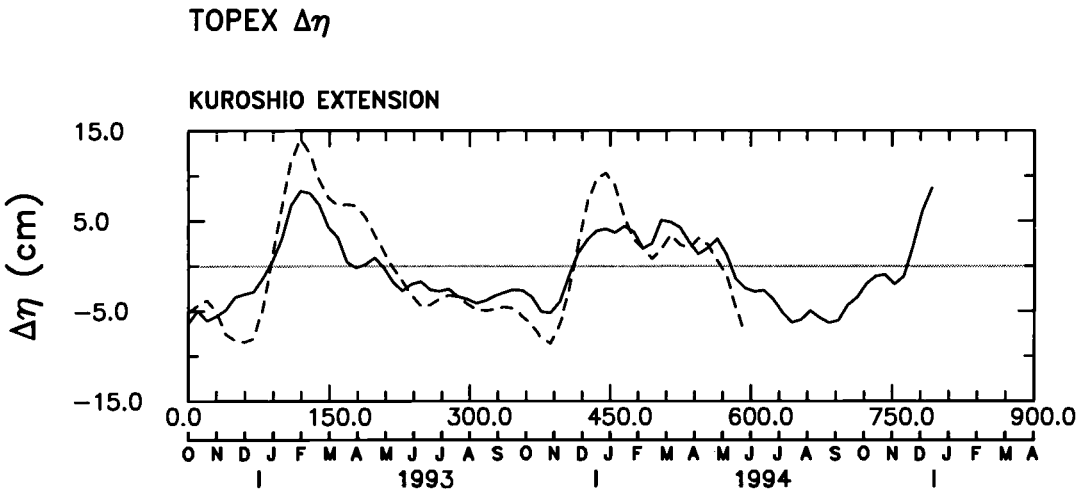

FIGURE 5.16. Variation of sea level differences (cm) across the Kuroshio Extension from the smoothed TP data. The result of the Sverdrup theory is also shown for comparison (dashed line).

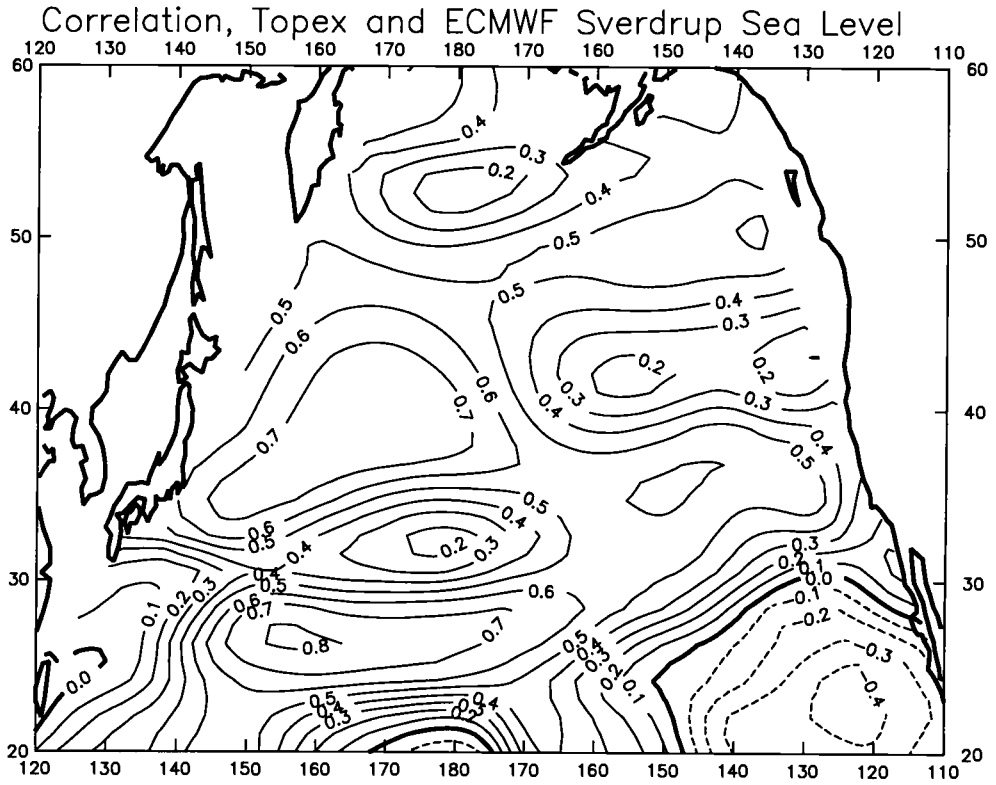

FIGURE 5.17. Correlation coefficient of Sverdrup sea level from ECMWF and TP sea level variations in the North Pacific.

TABLE 5.2. Correlation coefficient between Sverdrup and TP variations of sea level differences and the ratio of the standard deviation (SD) of the Sverdrup variations to the TP variations.

	Correlation	SD Ratio
Oyashio	0.50	2.13
Kuroshio	0.70	0.80
Oyashio + Kuroshio	0.81	1.79
Kuroshio Extension	0.89	1.60

large scales of the TP sea level were extracted using a bell-shaped low-pass filter (see Chelton et al., 1990a) with parameters $h_x = 25$ and $h_y = 4.5$, analogous to 5° latitude by 30° longitude averages. The correlation is largest over the western subpolar and subtropical North Pacific near the latitudes of maxima WBC variability in the Sverdrup theory (see Fig. 5.7). The correlation is lowest and even negative over the low latitude band south of about 25°N were long Rossby wave activity is expected to dominate the TP observations even in the spatially smoothed TP fields considered here. A tongue of low correlation is seen to extend from the western to the central North Pacific between 30-35°N along the paths of the Kuroshio and Kuroshio Extension. This low correlation is probably related to the eddies and meanders associated with these currents. There is also a region of low correlation in the eastern North Pacific west of 160°E between 40–45°N which coincides approximately with the line of zero wind stress curl (see Fig. 5.1) and therefore persistent nearly zero amplitudes in the Sverdrup sea level.

5.7. Summary and Discussion

We have calculated transport variations of the Oyashio/Kuroshio current system using flat-bottom, time-dependent Sverdrup theory. The Sverdrup theory was forced with temporally and spatially smoothed 10-day average wind stress derived from ECMWF 10-meter winds for the period October 1992 to June 1994. The results of the time-dependent Sverdrup theory were compared to similarly filtered and smoothed barotropic streamfunction fields from a primitive-equation model developed by the Parallel Ocean Program of Los Alamos National Laboratory (referred as the POP model), which was forced with 3-day average ECMWF winds (Dukowicz and Smith 1994). The POP model also includes surface heat and salt fluxes and deep thermohaline forcing at high latitudes.

The transport variations in both theory and model agree remarkably well and predict that the net meridional transports of the Oyashio, Kuroshio (including their recirculations) and the Kuroshio Extension fluctuate coherently with stronger transports in winter and weaker transports in summer/fall. This agreement indicates that $\sim$ 65–80% of the POP transport variability on seasonal and longer time scales in the western North Pacific is accounted for by simple flat-bottom, time-dependent Sverdrup dynamics. The amplitude of the Sverdrup and POP transport variations are about the same in the Kuroshio. However, the Sverdrup transport variations are somewhat larger than in the POP model in the in the Oyashio and Kuroshio Extension. This may reflect the importance of other dynamical processes (e.g. topographic blocking of the flow and dissipation) that are not included in the flat-bottom Sverdrup theory.

The results obtained here are similar to the results of Sekine and Kutsuwada (1994) in that the Sverdrup and modeled Kuroshio transport variations are in phase.

However, the amplitudes of the Kuroshio transport variations in their topographic model were smaller than in the flat-bottom Sverdrup theory by about 75%. This is in contrast with the good agreement found here between the amplitudes of the Sverdrup and POP Kuroshio transport variations perhaps because of the crude representation of stratification in their two-layer model. The amplitude of the Kuroshio transport variations in their topographic model agreed better with the Sverdrup theory when integrated westward from the Hawaii Ridge rather than from the eastern boundary. This was interpreted as evidence that the Sverdrup theory is valid only in the western-half of the Pacific. The agreement obtained here between the amplitudes of the transport variations in the Kuroshio from the basin-integrated Sverdrup theory and the POP model indicates that the transport variability over the western Pacific may be a basin-wide response to the winds.

An attempt to validate the Sverdrup theory results using temporally and spatially smoothed TP sea level data was presented. The sea level differences across the currents estimated from the Sverdrup theory assuming that the transport variations are geostrophic and barotropic were compared to the TP altimeter observations. The steric height changes known to dominate the TP sea level data on seasonal time-scales were removed using Stammer (1996) estimates from ECMWF heat fluxes. The effects of quasi-annual first-baroclinic Rossby waves in the TP data were ameliorated by the spatial averaging. Only in the Kuroshio do variations of Sverdrup and TP sea level differences agree well.

In conclusion, although the statistical significance of this analysis of large-scale variability on seasonal time scales is limited by the short (20-month) overlapping records of the POP model and TP observations, the analysis clearly indicates the importance of a Sverdrup-like response of the gyre-scale circulation of the North Pacific to wind forcing. The discrepancies between the amplitudes of the Sver-

drup and POP transport variations indicate that Sverdrup dynamics is not the only mechanism.

Although, the POP simulation is quite realistic in many respects, there are still large sources of error that are difficult to quantify. One of the major sources of error in model simulations is inaccuracies in the wind forcing. This may account for the closer agreement between the Sverdrup theory and the POP model (both of which were forced with ECMWF winds) than between the theory and the TP observations.

6. GENERAL CONCLUSIONS

The theory of wind-driven circulation for an homogeneous ocean is well established (e.g., Chapter 5 of Pedlosky, 1979). Briefly, when the primitive equations are scaled in terms of the Rossby and Ekman numbers, at the lowest order in both of these numbers the flow is geostrophic and non-divergent. To first order in the Rossby and Ekman numbers and for sufficiently small bottom slopes, the flow is governed by the non-linear quasigeostrophic potential vorticity equation. For the spatial scales of interest in this study ($L \gtrsim 1000$ km), the Rossby number is small ($U/fL \sim 10^{-3}$) and the vorticity equation can be linearized by neglecting the advection of relative vorticity. Furthermore, neglecting the bottom slopes (i.e. neglecting the vertical velocity at the bottom), we obtain the flat-bottom linearized quasigeostrophic vorticity equation (equation 4, Chapter 2). In this equation, the vorticity input by the wind is balanced by the time rate of change of relative vorticity and the advection of planetary vorticity (beta term).

The relative vorticity can be scaled by the spatial scale L of the wind and the x-derivative in the beta term by the width b of the ocean. The ratio of these two terms then defines a time scale $T = b/\beta L^2$, which is referred to as the barotropic adjustment time scale since this is the time required for a barotropic Rossby wave to cross the ocean. In the North Pacific at 40°N, the width of the ocean $b = 10000$ km. For a spatial scale of the wind forcing $L \sim 1000$ km, the adjustment time scale is $T \approx 10$ days. If the temporal scale of the wind forcing is T^*, the nature of the response depends on how T^* compares to the barotropic adjustment time scale T. For $T^* \ll T$ the response will be local; for $T^* \sim T$ the response will be Rossby waves; and for $T^* \gg T$ the response will be a quasi-steady Sverdrup balance (in this thesis,

we refer to this as either quasi-steady or time-dependent Sverdrup balance). For the temporal scales of interest in this study, $T^* \gtrsim 30$ days, the barotropic response will be in quasi-steady Sverdrup balance. Therefore the vorticity equation takes the familiar form where the input of vorticity by the wind stress curl is balanced only by the advection of planetary vorticity in the water column.

The theory summarized above describes the adjustment of a barotropic ocean. For an ocean with stratification there is also a baroclinic adjustment time scale determined by the time it takes the slower baroclinic Rossby waves to cross the ocean. The baroclinic adjustment time scale of the ocean at mid-latitudes is about 10 years, which is much larger than the barotropic adjustment time scale. Because in this thesis we focus on seasonal and shorter time scales, we can assume that the barotropic response will be dominant. On the seasonal scales of interest, the quasi-steady Sverdrup balance should pertain. This is the hypothesis tested in this thesis. In general, the approach followed is to estimate the Sverdrup streamfunction field (or Sverdrup sea level assuming geostrophic and barotropic flow) from wind stress curl fields, and then to compare the results with the streamfunction field simulated by a primitive equation model and with sea level fields observed by satellite altimeter.

In Chapter 2, the theoretical flat-bottom Sverdrup balance was tested in the South Pacific (40° to 60°S) using Seasat observations of winds stress curl and sea level over a three-month period. In the western South Pacific, the sea level changes from July to September 1978 predicted by the Sverdrup model forced by the Seasat-A Satellite Scatterometer (SASS) winds were consistent with the sea level changes observed by the Seasat altimeter and by three tide gauges in New Zealand. The flat-bottom Sverdrup model did not reproduce an observed decrease of sea level east of the East Pacific Rise. Sea level changes estimated using the topographic Sverdrup

balance were inconsistent with the observations in the western South Pacific. In the eastern South Pacific, the topographic Sverdrup balance is inadequate because of the presence of closed f/H contours. The main limitation of this analysis was the short record length of the Seasat observations.

When two years of sea level observations by the Geosat altimeter became available, the natural question was whether the Seasat South Pacific results could be reproduced in the longer data record. Since there were no simultaneous scatterometer wind observations during the Geosat mission, wind products from weather analyses by the European Centre for Medium-Range Weather Forecasts (ECMWF) provided a potentially viable alternative. However, the quality of the ECMWF winds in the South Pacific had not yet been established.

The accuracy of the ECMWF-based wind stress climatology derived by Trenberth et al. (1990) (referred to as the TLO climatology) was therefore evaluated in Chapter 3 by comparison with global 2-month averaged wind stress fields constructed from SASS winds. It was demonstrated indirectly that the effects of SASS scatterometer sampling errors on 2-month averaged wind stresses could be compensated by increasing the magnitude of the SASS wind stress by 7%. After applying this correction, the TLO climatology was found to be systematically stronger than SASS by almost 50% in extratropical latitudes north of 50°S. It was shown that these differences can be accounted for if the ECMWF 1000 mb wind analyses are interpreted as actually representative of the winds at 1000 mb rather than representative of the winds at 10 m, as assumed in the TLO climatology. This conclusion is supported by a comparison of the synoptic ECMWF wind speeds with coincident buoy observations along the U.S. coasts.

Apart from the systematic difference attributable to the reference level problem, the 1980–1986 TLO climatology and the 1978 SASS wind stresses generally

compared well. Except in the Southern Ocean, the differences were within the expected range of interannual variability. At high southern latitudes, the TLO climatology differed from the SASS wind stress field but was found to be consistent with a climatology derived from wind analyses by the Australian Bureau of Meteorology (ABM). However, knowledge of the accuracies of these climatologies over the Southern Ocean awaits future direct comparisons with simultaneous scatterometer observations.

In Chapter 4, the time-dependent Sverdrup balance was tested in the South Pacific (between 30–55°S and east of 180°E) using ECMWF wind forcing. The theoretical predictions were compared with nearly two years of Geosat sea level observations and with sea level simulations from the layered Naval Research Laboratory (NRL) and the z-level Semtner and Chervin (SC) primitive equations models. Both models were forced with momentum fluxes derived from ECMWF winds and the SC model also included thermal forcing given by surface restoring to Levitus climatology. In this chapter, Empirical Orthogonal Function analysis was used as a filter and attention was focused on the dominant mode of variability. The effect of topography associated with the East Pacific Rise was evident in the numerical model results and, similar to the Seasat study summarized in Chapter 2, in the altimetric observations. Significant spatial and temporal correlations between the theory and the observations as well as between the theory and the models were identified. These results were encouraging, although the dynamics behind the observed sea level variations were unclear. The questionable quality of the Geosat sea level observations, the unknown contribution of seasonal heating and cooling to the altimetric observations, and the unknown quality of the ECMWF winds at high southern latitudes were all major concerns in that analysis.

In Chapter 5, the Sverdrup theory was tested in the extratropical North Pacific because this basin more closely satisfies the fundamental assumptions inherent in the Sverdrup approximation than does the South Pacific. In particular, the North Pacific is deeper and has more zonally oriented f/H contours. The Sverdrup theoretical results were compared with streamfunction fields from a primitive equation numerical simulation by the Parallel Ocean Program (POP) of the Los Alamos National Laboratory forced with ECMWF winds. For consistency, the Sverdrup theoretical predictions were also calculated using ECMWF wind forcing. The time period analyzed here was October 1992–June 1994. On large space and time scales, the POP model was shown to be in quasi-steady Sverdrup balance. The net meridional transports near the western boundary of the subpolar (the Oyashio Current) and subtropical (the Kuroshio Current) gyres plus their recirculations and in the Kuroshio Extension are stronger in winter and weaker in summer/fall.

An attempt was made to validate these results using high quality sea level observations from the TOPEX/POSEIDON (TP) altimeter. On seasonal time scales, the TP sea level observations are dominated by steric height changes and by quasi-annual first baroclinic Rossby waves. Since this study of the Sverdrup theory deals only with the wind-driven response, an estimate of the steric height changes based on ECMWF heat fluxes (Stammer, 1996) was removed. The effect of the Rossby waves was ameliorated by box averaging over zonal scales much longer than the zonal wavelengths of baroclinic Rossby waves. The sea level differences across the meridional flow near the western subtropical boundary and across the Kuroshio Extension predicted from theory and observed by TP were highly correlated. The predicted and observed sea level differences across the Oyashio during October 1992–June 1994 compared less favorably. In particular, the inferred decrease in the transport of the Oyashio during summer/fall of 1993 was not observed by TP. It is interesting

to note, however, that the TP observations did show a decrease in the Oyashio flow during summer/fall of 1994. The source of this apparent interannual fluctuation of sea level has not yet been identified.

The possibility that the discrepancies between theory and observations in the subpolar North Pacific may be attributable to inaccuracies in the wind forcing was investigated. In the theory-model comparisons this was not a major issue because the forcings of both theoretical Sverdrup balance and the POP model simulation were based on ECMWF winds. From the ECMWF-SASS wind stress comparison in Chapter 3, significant differences were observed in the northeastern North Pacific, but they could be attributed to interannual variability. An analysis of the Sverdrup theory using contemporaneous ERS-1 scatterometer winds gave results very similar to the ones based on ECMWF products presented in this thesis. Therefore, the failure of the theory to show the decrease of the Oyashio flow during 1993 is not likely a result of problems in the ECMWF winds.

The sea level amplitudes predicted by the barotropic, flat-bottom, time-dependent Sverdrup theory generally did not compare well with the amplitude of the altimetric observations. In the Seasat South Pacific study, the Sverdrup sea level change from July to September 1978 was larger than observed by a factor of about three. In the Geosat South Pacific study, the standard deviation of the amplitude time series of the Sverdrup sea level first EOF was about 60% larger than the observed. In the Topex North Pacific Study, the standard deviation of the sea level differences across the Oyashio and Kuroshio Extension are about 1.6–2 times larger than observed. The amplitude of the theoretical and observed sea level compared better in the subtropical North Pacific. The standard deviation of the sea level differences across the Kuroshio and its recirculation was only 20% smaller than the observed.

The discrepancies between predicted and modeled sea level amplitudes may be related to the assumption of geostrophic flow invoked to convert from Sverdrup streamfunction to sea level (the Sverdrup flow is the sum of the geostrophic and the Ekman flow). To evaluate this hypothesis estimates of the Ekman component of the flow could be removed before converting streamfunction to sea level. Another source of error in the amplitude of the theoretical sea level estimates is the value of H which in a stratified ocean represents the effective depth of the wind forced motions. The value of H could be determined by comparing the barotropic streamfunction and sea level from the numerical simulations. This would require that the steric component of sea level in the model be previously estimated and removed.

In summary, we have tested the barotropic, flat-bottom, time-dependent Sverdrup balance in the Pacific on large space and time scales. In the western South Pacific, the Sverdrup balance is consistent with the 3-month, Seasat, wind and sea level observations. Analysis of the 2-year records of Geosat sea level and ECMWF winds gives similar results. However, the Seasat observational record is too short and the quality of the Geosat data is questionable. In the western North Pacific, barotropic transport variations simulated by the primitive equations POP model and estimated by the flat-bottom, time-dependent Sverdrup theory agree well. Using high quality TP sea level observations, we show that only in the Kuroshio the Sverdrup and observed sea level differences across the currents agree well.

BIBLIOGRAPHY

Aagaard, K., 1969: Relationship between geostrophic and surface winds at weather ship M. *J. Geophys. Res.*, **74**, 3440–3442.

Anderson, D. L., and R. A. Corry, 1985a: Ocean response to low frequency wind forcing with application to the seasonal variation in the Florida Straits–Gulf Stream transports, *Prog. Oceanogr.*, **14**, 7–40.

Anderson, D. L., and R. A. Corry, 1985b: Seasonal transport variations in the Florida Straits: A model study. *J. Phys. Oceanogr.*, **15**, 773–786.

Anderson, D. L., and P. D. Killworth, 1977: Spin-up of a stratified ocean, with topography. *Deep Sea Res.*, **24**, 709–732.

Anderson, D. L., K. Bryan, A. E. Gill, and R. C. Pacanowski, 1979: The transient response of the North Atlantic: Some model studies. *J. Geophys. Res.*, **84**, 4795–4815.

Anderson, D., A. Hollingsworth, S. Uppala, and P. Woiceshyn, 1991: A study of the use of scatterometer data in the European Centre for Medium Range Weather Forecasts operational analysis-forecast model, 1. Quality assurance and validation. *J. Geophys. Res.*, **96**, 2619–2634.

Atlas, R., A. J. Busalacchi, M. Ghil, S. Bloom, and E. Kalnay, 1987: Global surface wind and flux fields from model assimilation of Seasat data. *J. Geophys. Res.*, **92**, 6477–6487.

Baker, D. J., Jr., 1982: A note on Sverdrup Balance in the Southern Ocean. *J. Mar. Res.*, **40**, (Supplement), 21–26.

Barnier, B., 1986: Investigation of the seasonal variability of the wind stress curl over the North Atlantic Ocean by means of empirical orthogonal function analysis. *J. Geophys. Res.*, **91**, 863–868.

Beal, R. C., 1991: *Directional Ocean Wave Spectra.* Johns Hopkins University Press, Baltimore, 218 pp.

Blaha, J., and R. Reed, 1982: Fluctuations of sea level in the western North Pacific and inferred flow of the Kuroshio, *J. Phys. Oceanogr.*, **12**, 669–678.

Böttger, H., 1982: Local weather element guidance from the ECMWF forecasting system in the medium range. A verification study. Seminar/Workshop 1982 Interpretation of Numerical Weather Predictions Products. ECMWF, 417–441.

Chelton, D. B., 1983: Effects of sampling errors in statistical estimation. *Deep-Sea Res.*, **30**, 1083–1103.

Chelton, D. B., and F. J. Wentz, 1986: Further development of an improved altimeter wind speed algorithm. *J. Geophys. Res.*, **91**, 14250–14260.

Chelton, D. B., M. H. Freilich, and J. R. Johnson, 1989: Evaluation of unambiguous vector winds from the Seasat scatterometer. *J. Atmos. Oceanic Technol.*, **6**, 1024–1039.

Chelton, D. B., A. M. Mestas-Nuñez, and M. H. Freilich, 1990a: Global wind stress and Sverdrup circulation from the Seasat scatterometer. *J. Phys. Oceanogr.*, **20**, 1175–1205.

Chelton, D. B., M. G. Schlax, D. L. Witter, and J. G. Richman, 1990b: Geosat altimeter observations of the surface circulation of the Southern Ocean. *J. Geophys. Res.*, **95**, 17877–17903.

Chelton, D. B., and M. G. Schlax, 1996: Global observations of oceanic Rossby waves. *Science*, in press.

Clarke, A. J., 1982: The dynamics of large-scale, wind-driven variations in the Antarctic Circumpolar Current. *J. Phys. Oceanogr.*, **12**, 1092–1105.

Clarke, R. H., and G. D. Hess, 1975: On the relation between surface wind and pressure gradient, especially in lower latitudes. *Bound.-Layer Meteorl.*, **9**, 325–339.

Cummings, P. F., 1991: The barotropic response of the subpolar North Pacific to stochastic wind forcing. *J. Geophys. Res.*, **96**, 8869–8880.

Davison, J., and D. E. Harrison, 1990: Comparison of Seasat scatterometer winds with tropical Pacific observations. *J. Geophys. Res.*, **95**, 3403–3410.

Deacon, G. E. R., 1977: Comments on a counterclockwise circulation in the Pacific subantarctic sector of the Southern Ocean suggested by McGinnis. *Deep Sea Res.*, **24**, 927–930.

Deacon, G. E. R., 1982: Physical and biological zonation in the Southern Ocean. *Deep-Sea Res.*, **29**, 1–15.

deSzoeke, R. A., 1987: On the wind-driven circulation of the South Pacific Ocean. *J. Phys. Oceanogr.*, **17**, 613–630.

Dittmer, K., 1977: The hydrodynamic roughness of the sea surface at low wind speeds. *Meteor. Forsch.-Ergebnisse,* Reihe B., **12**, 10–15.

Dukowicz, J. K., and R. D. Smith, 1994: Implicit free-surface method for the Bryan-Cox-Semtner ocean model. *J. Geophys. Res.*, **99**, 7991–8014.

Effron, B., 1979: Computers and the theory of statistics: Thinking the unthinkable. *SIAM Rev.*, **21**, 460–480.

Ehret, L. L., and J. J. O'Brien, 1989: Scales of North Atlantic wind stress curl determined from the comprehensive ocean-atmosphere data set. *J. Geophys. Res.*, **94**, 831–841.

Findlater, J., T. N. S. Harrower, G. A. Howkins, and H. L. Wright, 1966: Surface and 900 mb wind relationships. *Scientific Paper* No. 23, Meteorological office, London, England, 41 pp.

Freilich, M. H., and R. S. Dunbar, 1993: Derivation of satellite wind model functions using operational surface wind analyses: An altimeter example. *J. Geophys. Res.*, **98**, 14633–14649.

Fu, L.-L., and D. B. Chelton, 1985: Observing large-scale temporal variability of ocean currents by satellite altimetry: with application to the Antarctic Circumpolar Current. *J. Geophys. Res.*, **90**, 4721–4739.

Fu, L.-L., and R. A. Davison, 1995: A note on the barotropic response of sea level to time-dependent wind forcing. *J. Geophys. Res.*, **100**, 24995–24963.

Fu, L.-L., and R. D. Smith, 1996: Global ocean circulation from satellite altimetry and high-resolution computer simulation, in preparation.

Garner, D. M., 1959: The Subtropical Convergence in New Zealand surface waters. *New Zealand Journal of Geology and Geophysics*, **2**, 315–337.

Garzoli, S. L., and S. G. H. Philander, 1985: Validation of an Equatorial Atlantic simulation model using inverted echo sounder data. *J. Geophys. Res.*, **90**, 9199-9205.

Garzoli, S. L., Z. Garraffo, G. Podesta, and O. Brown, 1992: Analysis of a general circulation model product, 1, Frontal systems in the Brazil/Malvinas and Kuroshio/Oyashio regions. *J. Geophys. Res.*, **97**, 20117–20138.

Gill, A. E., 1968: A linear model of the Antarctic circumpolar current. *J. Fluid Mech.*, **32**, 465–488.

Gill, A. E., 1971: Ocean models. *Phil. Trans. Roy. Soc. London*, **A 270**, 391–414.

Gill, A. E., and P. P. Niiler, 1973: The theory of seasonal variability in the ocean. *Deep Sea Res.*, **20**, 141–177.

Godfrey, J. S., 1989: A Sverdrup model of the depth-integrated flow for the world ocean allowing for island circulations. *Geophys. Astrophys. Fluid Dyn.*, **45**, 89–112.

Gordon, A. L., E. Molinelli, and T. Baker, 1978: Large-scale relative dynamic topography of the Southern Ocean. *J. Geophys. Res.*, **83**, 3023-3032.

Gordon, A. L. and E. Molinelli, 1982: *Southern Ocean Atlas.* Columbia University Press, 34 pp. plus 248 plates.

Greatbatch, R. J., and A. Goulding, 1989: Seasonal variations in a linear barotropic model of the North Pacific driven by the Hellerman Rosenstein wind stress field. *J. Geophys. Res.*, **94**, 12645–12665.

Greatbatch, R. J., and A. Goulding, 1990: On the seasonal variation of transport through the Tokara Strait. *J. Oceanogr. Soc. Japan*, **46**, 9–20.

Greenslade, D. J. M., and D. B. Chelton, 1996: The resolution capability of single and tandem satellite altimeter missions. *J. Atmos. Oceanic Technol.*, submitted.

Haney, R. L., 1971: Surface thermal boundary condition for ocean circulation models. *J. Phys. Oceanogr.*, **1**, 241–248.

Harrison, D. E., 1989: On climatological monthly mean wind stress and wind stress curl fields over the world ocean. *J. Clim.*, **2**, 57–70.

Hasse, L., and V. Wagner, 1971: On the relationship between geostrophic and surface wind at sea. *Mon. Wea. Rev.*, **99**, 255–260.

Hautala, S. L., D. H. Roemmich, and W. J. Schmitz, Jr., 1994: Is the North Pacific in Sverdrup balance along 24°N? *J. Geophys. Res.*, **99**, 16041–16052.

Hellerman, S., and M. Rosenstein, 1983: Normal monthly wind stress over the world ocean with error estimates. *J. Phys. Oceanogr.*, **13**, 1093–1104.

Hurlburt, H. E., and J. D. Thompson, 1980: A numerical study of Loop Current intrusions and eddy sheddings. *J. Phys. Oceanogr.*, **10**, 1611–1651.

Hurlburt, H. E., A. J. Wallcraft, Z. Sirkes, and E. J. Metzger, 1992: Modeling of the Global and Pacific Oceans: On the path to eddy-resolving ocean prediction. *Oceanography*, **5**, 9–18.

Hurlburt, H. E., A. J. Wallcraft, W. J. Schmitz, Jr., P. J. Hogan, and E. J. Metzger, 1996: Dynamics of the Kuroshio/Oyashio current system using eddy-resolving models of the North Pacific Ocean. *J. Geophys. Res.*, **101**, 941-976.

Inoue, M., 1985: Modal Decomposition of the low-frequency currents and baroclinic instability at Drake Passage. *J. Phys. Oceanogr.*, **15**, 1158–1181.

Janssen, P. A. E. M., P. Lionello, M. Reistad, and A. Hollingsworth, 1989: Hindcasts and data assimilation studies with the WAM model during the Seasat period. *J. Geophys. Res.*, **94**, 973–993.

Johnson, G. C., and H. L. Bryden, 1989: On the size of the Antarctic Circumpolar Current. *Deep-Sea Res.*, **36**, 39–53.

Kawai, H., 1972: Hydrography of the Kuroshio Extension, in *Kuroshio, Physical Aspects of the Japan Current*, H. Stommel and K. Yoshida, Eds., University of Washington Press, 235–352.

Kelly, K., 1988: Comment on "Empirical orthogonal function analysis of advanced very high resolution radiometer surface temperature patterns in Santa Barbara Channel" by G.S.E. Lagerloef and R.L. Bernstein. *J. Geophys. Res.*, **93**, 15753–15754.

Kelly, K. A., and M. J. Caruso, 1990: A modified objective mapping technique for scatterometer wind data. *J. Geophys. Res.*, **95**, 13483–13496.

Killworth, P. D., D. Stainforth, D. J. Webb, and S. M. Paterson, 1991: The development of a free-surface Bryan-Cox-Semtner ocean model. *J. Phys. Oceanogr.*, **21**, 1333–1348.

Koblinsky, C. J., 1990: The global distribution of f/H and the barotropic response of the ocean. *J. Geophys. Res.*, **95**, 3213–3218.

Koblinsky, C. J., P. P. Niiler, and W. J. Schmitz, Jr., 1989: Observations of wind-forced deep ocean currents in the North Pacific. *J. Geophys. Res.*, **94**, 10773–10790.

Kutsuwada, K., and T. Teramoto, 1987: Monthly maps of surface wind stress fields over the North Pacific during 1961-1984. *Bulletin of the Ocean Research Institute, University of Tokio*, 100 pp.

Lalbeharry, R., M. L. Khandekar, and S. Peteherych, 1990: Wind specification based on Seasat A satellite scatterometer and conventional winds for driving an ocean wave model. *J. Geophys. Res.*, **95**, 761–773.

Lambert, S. J., 1988: A comparison of operational global analyses from the European Centre for Medium Range Weather Forecasts (ECMWF) and the National Meteorological Center (NMC). *Tellus*, **40 A**, 272–284.

Large, W. G., and S. Pond, 1982: Sensible and latent heat flux measurements over the ocean. *J. Phys. Oceanogr.*, **12**, 464–482.

Large, W. G., and H. van Loon, 1989: Large scale, low frequency variability of the 1979 FGGE surface buoy drifts and winds over the southern hemisphere. *J. Phys. Oceanogr.*, **19**, 216–232.

Leetmaa, A., P. Niiler, and H. Stommel, 1977: Does the Sverdrup relation account for the Mid-Atlantic circulation? *J. Mar. Res.*, **35**, 1–10.

Legler, D. M., and J. J. O'Brien, 1985: Development and testing of a simple assimilation technique to derive average wind fields from simulated scatterometer data. *Mon. Wea. Rev.*, **113**, 1791–1800.

Levitus, S., 1982: *Climatological atlas of the world oceans.* NOAA Professional Paper 13, U.S. Department of Commerce, 173 pp.

Lionello, P., H. Günther, and P. A. E. M. Janssen, 1992: Assimilation of altimeter data in a global third-generation wave model. *J. Geophys. Res.*, **97**, 14453–14474.

Liu, W. T., K. B. Katsaros and J. A. Businger, 1979: Bulk parameterization of air-sea exchange in heat and water vapor including the molecular constraints at the interface. *J. Atmos. Sci.*, **36**, 1722–1735.

Matano, R. P., M. G. Schlax, and D. B. Chelton, 1993: Seasonal variability in the Southwestern Atlantic. *J. Geophys. Res.*, **98**, 18027–18035.

Meindl, E. A., and G. D. Hamilton, 1992: Programs of the National Data Buoy Center. *Bull. Amer. Meteor. Soc.*, **73**, 985–993.

Mestas-Nuñez, A. M., D. B. Chelton, and R. A. deSzoeke, 1992: Evidence of time-dependent Sverdrup circulation in the South Pacific from the Seasat scatterometer and altimeter. *J. Phys. Oceanogr.*, **22**, 934–943.

Mestas-Nuñez, A. M., D. B. Chelton, M. H. Freilich, and J. G. Richman, 1993: An evaluation of ECMWF-based climatological wind stress fields. *J. Phys. Oceanogr.*, **24**, 1532–1549.

Mulhearn, P. J., 1987: The Tasman Front: A study using satellite infrared imagery. *J. Phys. Oceanogr.*, **17**, 1148–1155.

Munk, W. H., 1950: On the wind-driven ocean circulation. *J. Meteorol*, **7**, 79–93.

Nerem, R. S., E. J. Schrama, C. J. Koblinski, and B. D. Beckley, A preliminary evaluation of ocean topography from the TOPEX/POSEIDON mission. *J. Geophys. Res.*, **99**, 24565–24583.

Neumann, G., 1955: On the dynamics of wind-driven ocean currents. *Meteorological Papers*, **2**, 33 pp.

Niiler, P. P., and W. S. Richardson, 1973: Seasonal variability of the Florida Current, *J. Mar. Res.*, **31**, 144–167.

Niiler, P. P., W. J. Schmitz, and D.-K. Lee, 1985: Geostrophic volume transport in high eddy-energy areas of the Kuroshio Extension and Gulf Stream, *J. Phys. Oceanogr.*, **15**, 825–843.

NOAA, 1986: ETOP05 digital relief of the surface of the earth, Data Announcement 86-MGG-07, National Geophysical Data Center.

Patterson, S. L., and T. Whitworth, 1990: Physical Oceanography, in *Antarctic Sector of the Pacific*. Elsevier, 396 pp.

Pedlosky, J., 1987: *Geophysical Fluid Dynamics*. Springer-Verlag, 710 pp.

Peterson, R. G., 1988: On the transport of the Antarctic Circumpolar Current through Drake Passage and its relation to wind. *J. Geophys. Res.*, **93**, 13993–14004.

Preisendorfer, R. W., 1988: *Principal component analysis in meteorology and oceanography. Developments in atmospheric sciences 17.* Elsevier, 425 pp.

Press W. H., B. P. Flannery, S. A. Teukolsky, and W. T. Vetterling, 1989: *Numerical Recipes, The art of Scientific Computing (FORTRAN version).* Cambridge University Press, 702 pp.

Reid, J. L., 1986: On the total geostrophic circulation of the South Pacific Ocean: Flow patterns, tracers and transports. *Prog. Oceanog.*, **16**, 1–61.

Reynolds, R. W., K. Arpe, C. Gordon, S. P. Hayes, A. Leetmaa, and M. J. McPhaden, 1989: A comparison of tropical Pacific surface winds analyses. *J. Clim.*, **2**, 105–111.

Schacher, G. E., K. L. Davidson, T. E. Houlihan and C. W. Fairall, 1981: Measurements of the rate of dissipation of turbulent kinetic energy, ϵ, over the ocean. *Bound.-Layer Meteorl.*, **20**, 321–330.

Schaefer, J. T., and C. A. Doswell III, 1979: On the interpolation of a vector field. *Mon. Wea. Rev.*, **107**, 458–476.

Schmitz, W. J., Jr., J. D. Thompson, and J. R. Luyten, 1992: The Sverdrup circulation for the Atlantic along 24°N. *J. Geophys. Res.*, **97**, 7251–7256.

Sekine, Y., 1988: Anomalous southward intrusion of the Oyashio east of Japan. 1. Influence of the seasonal and interannual variations in the winds stress over the North Pacific. *J. Geophys. Res.*, **93**, 2247–2255.

Sekine, Y., and K. Kutsuwada, 1994: Seasonal variation in volume transport of the Kuroshio south of Japan. *J. Phys. Oceanogr.*, **24**, 261–272.

Semtner, A. J., and R. M. Chervin, 1992: Ocean general circulation from a global eddy resolving model. *J. Geophys. Res.*, **97**, 5493–5550.

Shea, D. J., K. E. Trenberth, and R. W. Reynolds, 1990: A global monthly sea surface temperature climatology. National Center for Atmos. Res. Tech. Note NCAR/TN-345 +STR, 167 pp.

Stammer, D., 1996: Steric and wind-induced changes in TOPEX/POSEIDON large-scale sea surface topography observations, in preparation.

Stanton, B. R., 1981: An oceanographic survey of the Tasman Front, *N.Z. J. Mar. Freshwater Res.*, **15**, 289–297.

Stommel, H., 1948: The westward intensification of wind-driven ocean currents. *Trans. Amer. Geophys. Un.*, **29**, 202–206.

Stommel, H., 1957: A survey of ocean current theory. *Deep Sea Res.*, **4**, 149–184.

Stommel, H., and K. Yoshida, 1972: *Kuroshio, Physical Aspects of the Japan Current.* University of Washington Press, 517 pp.

Sverdrup, H. U., 1947: Wind-driven currents in a baroclinic ocean: with application to the equatorial currents in the eastern Pacific. *Proc. Natl. Acad. Sci. U.S.A.*, **33**, 318–326.

Taft, B., 1972: Characteristics of the flow of the Kuroshio south of Japan, in *Kuroshio, Physical Aspects of the Japan Current*, H. Stommel and K. Yoshida, Eds., University of Washington Press, 165–216.

Tomczak, M., and J. S. Godfrey, 1994: *Regional Oceanography: An Introduction.* Pergamon, 422 pp.

Trenberth, K. E., J. G. Olson, and W. G. Large, 1989: A global ocean wind stress climatology based on ECMWF analyses. National Center for Atmos. Res. Tech. Note NCAR/TN-338 +STR, 93 pp.

Trenberth, K. E., W. G. Large, and J. G. Olson, 1990: The mean annual cycle in global ocean wind stress. *J. Phys. Oceanogr.*, **20**, 1742–1760.

van Loon, H., and J. C. Rogers, 1984: The yearly wave in pressure and zonal geostrophic wind at sea level on the southern hemisphere and its interannual variability. *Tellus*, **36A**, 348–354.

Wallcraft, A. J., 1991: The Navy layered ocean model users guide. *Naval Oceanographic and Atmospheric Research Laboratory Report 35*, 21 pp.

Wentz, F. J., L. A. Mattox, and S. Peteherych, 1986: New algorithms for microwave measurements of ocean winds with application to Seasat and SSM/I. *J. Geophys. Res.*, **21**, 2289–2307.

Whitworth, T., and R. G. Peterson, 1985: The volume transport of the Antarctic Circumpolar Current from bottom pressure measurements. *J. Phys. Oceanogr.*, **15**, 810–816.

Wilkin, J. L., R. A. Morrow, 1994: Eddy kinetic energy and momentum flux in the Southern Ocean: Comparison of a global eddy-resolving model with altimeter, drifter, and current-meter data.

Willebrand, J., 1978: Temporal and spatial scales of the wind field over the North Pacific and North Atlantic. *J. Phys. Oceanogr.*, **8**, 1080–1094.

Willebrand, J., S. G. Philander, and R. C. Pacanowski, 1980: The oceanic response to large-scale atmospheric disturbances. *J. Phys. Oceanogr.*, **10**, 411–429.

Wunsch, C., and D. Roemmich, 1985: Is the North Atlantic in Sverdrup balance? *J. Phys. Oceanogr.*, **15**, 1876–1880.

Wyrtki, K., 1971: *Oceanographic Atlas of the Indian Ocean Expedition.* National Science Foundation NSF-10E-1, 531 pp.

Zlotnicki, V., 1991: Sea level differences across the Gulf Stream and Kuroshio Extension. *J. Phys. Oceanogr.*, **21**, 599–609.